University of Alberta

Effect of crystallinity on crack propagation and mineralization of bioactive glass 45S5

by

Satadru Kashyap

A thesis submitted to the Faculty of Graduate Studies and Research
in partial fulfillment of the requirements for the degree of

Master of Science

in

Materials Engineering

Department of Chemical and Materials Engineering

Examining Committee

Dr. John A. Nychka, Advisor, Chemical and Materials Engineering, University of Alberta

Dr. Adrian Gerlich, Chemical and Materials Engineering, University of Alberta

Dr. Robert Luth, Earth and Atmospheric Sciences, University of Alberta

Dedicated

to

Maa, Deta, Jethu, Jethai and Maina

ABSTRACT

Bioactive glasses are a type of ceramic material designed to be used as bioresorbable therapeutic bone implants. Thermal treatment of bioactive glass ceramics dictates many important features such as microstructure, degree of crystallinity, mechanical properties, and mineralization. This study investigates the effects of temperature, time, and heating rates on the crystallization kinetics of melt cast bioactive glass 45S5. Bulk crystallization (three dimensional crystallite formation) was found to always occur in bulk bioactive glass 45S5 irrespective of the processing conditions. A comparative study of crack paths in amorphous and crystalline phases of bioactive glass 45S5 revealed crack deflections and higher fracture resistance in partially crystallized bioactive glass. Such toughening is likely attributed to different crystallographic orientations of crystals or residual thermal mismatch strains. Furthermore, *in vitro* immersion testing of partially crystalline glass ceramic revealed higher adhesion capabilities of the mineralized layer formed on amorphous regions as compared to its crystalline counterpart.

ACKNOWLEDGEMENTS

TABLE OF CONTENTS

LIST OF TABLES

LIST OF FIGURES

LIST OF SYMBOLS

f	Fraction transformed or crystalline volume fraction transformed
t	Time (minutes)
k	Avrami rate constant
n	Avrami exponent
E_a	Activation energy (kJ/mol)
α	Heating rate (K/min)
T_p	Peak crystallization temperature (K)
R	Gas constant ($8.314\ \mathrm{JK}^{-1}\ \mathrm{mol}^{-1}$)
W	Full width of the crystallization peak at the half maximum (FWHM)
GS	Average grain size
L	Length of line drawn on micrographs for grain size measurement
N	Number of intercept made by each line of length L at the grain boundaries
V_S	Volume of immersion medium required (ml)
S_A	Apparent surface area of the specimen (mm^2)
$\bar{d}$	Average diameter of samples (mm)
$\bar{r}$	Average radius of samples (mm)
$\bar{h}$	Average height of samples (mm)
K_{IC}	Fracture toughness ($\mathrm{MPam}^{-1/2}$)
P	Indentation load (N)
E	Young's modulus of the material (MPa)
H	Hardness of the material(GPa),
δ	Empirical constant of 0.016 ± 0.004 for the Vickers indentation technique
c	Half length of Palmqvist crack (m)
h_m	thickness of mineralized layer
h_S	thickness of bioactive glass sample (substrate)
ε_m	Drying strain in mineralized layer
ε_S	Drying strain in bioactive glass 45S5 (substrate)

ε_c	Cracking strain generated in the mineralized layer atop amorphous regions
ε^e_m	Biaxial elastic strain generated in the mineralized layer
ε^e_S	Biaxial elastic strain generated in bioactive glass 45S5 (substrate)
E_m	Young's modulus of the mineralized layer
E_S	Young's modulus of bioactive glass 45S5 (substrate)
σ_m	Biaxial stress on mineralized layer
σ_S	Biaxial stress on bioactive glass 45S5 (substrate)
v_m	Poisson's ratio of the mineralized layer
v_S	Poisson's ratio of bioactive glass 45S5 (substrate)
ε_{bc}	Strain that caused bifurcating cracks in mineralized laye atop crystalline region
ε_κ	Strain due to curvature that caused mineralized layer atop crystalline region to peel off from substrate
G	Energy release rate

LIST OF ABBREVIATIONS

HCA	Hydroxy carbonate apatite
SBF	Simulated body fluid
PBS	Phosphate buffer solution
DTA	Differential thermal analysis
DSC	Differential scanning calorimetry
FWHM	Full width at half maximum
TTT	Time temperature transformation
XRD	X-ray diffraction
FTIR	Fourier transform infrared spectroscopy
SEM	Scanning electron microscopy
DPT	Dye penetrant test
SENB	Single-edge notched beam
CCT	Continuous cooling transformation
TEM	Transmission electron microscopy

CHAPTER 1

Introduction

Synopsis of the thesis

Bioactive glass 45S5 is an amorphous material that has been successfully used for local bone repair therapy. However, its usage as monolithic implant material in load bearing applications is unwarranted due to its poor mechanical performance. A possibility in increasing the fracture resistance of bioactive glass 45S5 would be to produce it as a glass ceramic with dispersion of a crystalline phase in the glassy matrix to effect crack deflection at and around crystals thereby increasing crack length, and in turn the fracture resistance. Production of a glass ceramic with optimum dispersion of crystals requires complete knowledge of its crystallization kinetics. Moreover, this glass ceramic with a crystalline phase must maintain the inherent bioactivity for bioactive glass 45S5. Hence, this study explores the possibility of producing this glass ceramic by studying the crystallization kinetics of bioactive glass 45S5 while comparing the crack propagation and mineralization phenomenon of the glass ceramic with its amorphous counterpart.

1.1 Biomaterials

The term 'biomaterial' was first coined to describe a material which could be used to replace diseased or damaged bones and tissues in a living organism. Application of engineering and biological principles over the last four decades to continuously develop structure, processing conditions, biocompatibility and efforts to apply budding ideas has led to evolution and diversification of these biomaterials. Interdisciplinary studies on material-tissue interfacial behaviour as well as tissue engineering have provided a huge impetus in the progression of bio-inert metals to bioresorbable materials being used as implants in the living body.

The first generation of biomaterials were 'biological inert or almost inert' materials which were used for the sole purpose of replacing a tissue by a metal that would release minimal amount of toxins and minimize scar tissue formation in the host body. Second generation biomaterials involved implant materials with the ability to bond with the tissue through different stages of interfacial reactions. However, the advent of tissue-regenerating and gene activating bioactive implant materials 40 years ago, ushered a new dawn in the field of biomaterials. Bioceramics form an integral part of this third generation of biomaterials and have been developed over the years into diverse forms, structures, types and compositions depending on the physiological and biological compatibility as well as the ease of manufacturing and application [1, 2].

1.2 Bioceramics

Bioceramics are essentially ceramic materials with the ability to become bioimplants by reconstructing or replacing damaged tissues. They are bioactive materials whose structure can be of diverse forms like polycrystalline (alumina or hydroxyapatite), glass (Bioglass$^{®}$), glass-ceramic (apatite/wollastonite) or composites (polyethylene hydroxyapatite) [3]. Moreover, these bioceramics can also be categorized based of their attachment with the host tissue/bone such as almost inert (Al_2O_3, ZrO_2 - dense, non porous), porous implants facilitating bone ingrowth (porous hydroxyapatite, hydroxyapatite coated porous metals), surface reactive ceramic, glasses or glass ceramics (bioactive glasses, bioactive glass ceramics, dense hydroxyapatite) and resorbable ceramics and glasses (bioactive glasses, tricalcium phosphate) [3]. Apart from being used as implant materials these bioceramics find a huge demand in the health care industry catering to the needs of eyeglasses, diagnostic instruments, fibre optics etc [4]. Bioactive glasses are relatively new class of bioceramics (consisting of both surface reactive and resorbable bioceramics) which have tremendous potential to revolutionize the health care industry by providing effective synthetic materials for replacement and restoration of damaged or diseased tissue or bones.

1.3 What are *bioactive glasses*?

First reported in the early 1970s by L.L. Hench and developed over a time span of four decades, bioactive glasses are bioceramic materials which can repair and rebuild damaged tissues, particularly hard tissues[5]. They stand out from other bioceramics or glass ceramic in the prospect that they can be tailor-made through a huge range of chemical composition, mechanical property and bonding speed with the host tissue. Therefore these bioactive glasses can be specifically made to cater requirements of many clinical applications [2, 3, 6].

Bioactive glasses can be produced with the conventional technologies of the glass industry by melt casting[7], but new procedures like sol-gel processing [8] can also be used to manufacture a variety of these bioactive glasses. Moreover, they can be produced in bulk, powder or sintered powder modes depending on the end usage.

The base components of these glasses are usually silica (SiO_2), sodium oxide (Na_2O), calcium oxide (CaO), and phosphorus pentoxide (P_2O_5). However, compounds like calcium fluoride (CaF_2) are also added in some bioactive glasses. Bioactive glasses differ from traditional soda lime glasses in the sense that [7] :

- They have less than 60 mol% SiO_2.
- Higher content of Na_2O and CaO.
- High CaO/ P_2O_5 ratio.

These properties make bioactive glass more surface reactive when in contact with an aqueous medium, such as body fluid, thereby increasing the chance of interfacial reactions with the tissue or bone. Bioactive glasses show different kinds of interfacial behaviour when used as bioimplants: some bond with both soft tissues and bone (e.g. bioactive glass 45S5), some only with bone (e.g. bioactive glass 5S4.3 or Ceravital), some get encapsulated with a non adhering fibrous tissue and others are completely resorbed within 30 days. L.L. Hench used the Na_2O-CaO-SiO_2 diagram (at 6 wt% of P_2O_5) shown in Figure 1.1 to explain

the biocompatibility behaviour of different bioactive glass compositions [2]. Based on their chemical composition and biocompatibility criteria bioactive glasses can be divided into 4 broad classes as shown in Table 1.1 [7, 9].

Biocompatibility	Approximate composition range (with constant 6 wt% P_2O_5)	Region in Fig 1.1
bioactive, bonds to bone, some formulations bond to soft tissues	35-60 mol.% SiO_2, 10-50 mol.% CaO, 5-40 mol.% Na_2O	A and S
non-bioactive, nearly inert, gets encapsulated with fibrous tissue	<35 mol.% SiO_2	B
bioactive, resorbed within 10–30 days	>50 mol.% SiO_2, <10 mol.% CaO, <35 mol.% Na_2O	C
technically impractical	>65 mol.% SiO_2	D

Table 1.1: Four classes of bioactive glasses and their compatibility with the bonding tissue (after [7, 9]).

Based on the Na_2O-CaO-SiO_2 phase diagram (at 6 wt% of P_2O_5) L.L. Hench also defined the two classes of bioactivity which show the highest amount of bone bonding and optimum dissolution in the body fluid to cause gene activation and catalyze the proliferation of osteoblasts. These two classes of bioactivity are [1, 2, 5]:

- **Class A: osteoconduction** and **osteoproduction** (corresponds to region S in Figure 1.1).[10, 11]
  - ✓ rapid bonding with bone
  - ✓ improved bone proliferation
  - ✓ bonds with soft tissues too

- **Class B**: **osteoproduction** only (corresponds to region A in Figure 1.1). [12, 13]

4

- ✓ slower bonding with bone

- ✓ no bone proliferation

- ✓ no bonding with soft tissues
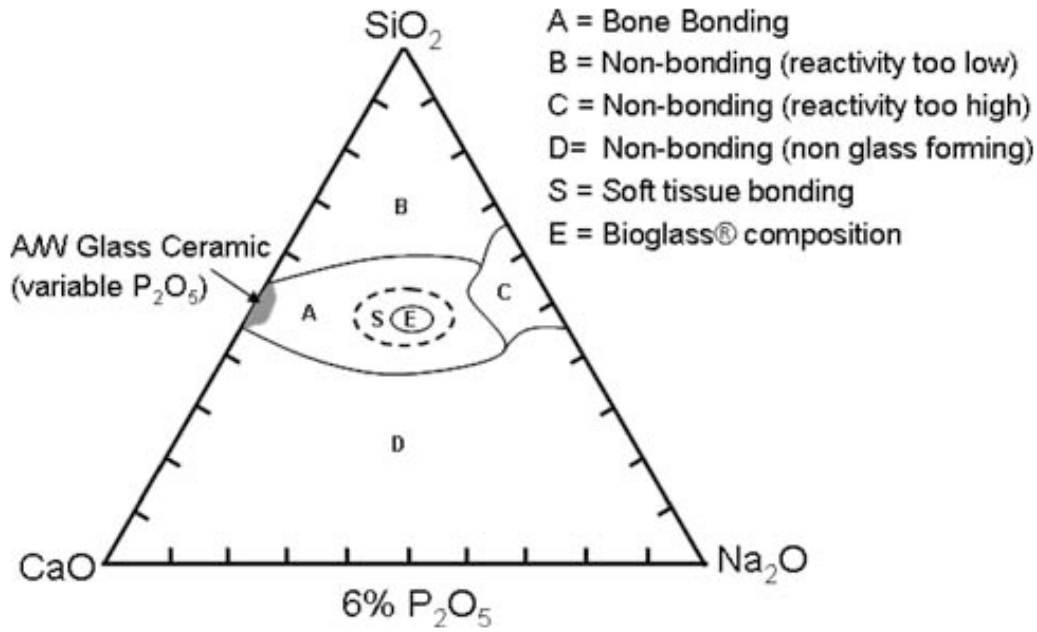
Fig.1.1: Na_2O-CaO-SiO_2 Compositional diagram for bone bonding with a constant 6 wt% of P_2O_5. Reproduced and adapted with permission and copyright © of the Journal of Materials Science: Materials in Medicine (Springer) [2].

However, in order to prove its efficiency, a bioactive glass must be biologically compatible with both bone and soft tissue in regards to its attachment with the bone/tissue, its dissolution rate in body fluids and its ability to catalyze regeneration of new cells on the interface. L.L. Hench [2, 5]formulated the first bioactive glass "**Bioglass**® **45S5**" using the Na_2O-CaO-SiO_2 phase diagram as he chose a composition in the region E inside region S of Figure 1.1 which enables this bioactive glass to bond with both bone and soft tissue making it both osteoconductive and osteoproductive [14-16] (i.e. it has Class A conductivity). Thereafter, various other categories of bioactive glasses were tried and tested based on need and applications. Since then, research has been carried out to seek better biocompatibility, characterization of these bio glasses and their reaction with the living tissue. Since their incipient stages, bioactive glasses have posed a

constant challenge to researchers all over the world in fields relating to their *in vitro* and *in vivo* bioactivity, interfacial reactions with tissue and enhancement of their mechanical properties.

1.4 Bioactive glass 45S5

Evolution and varieties of bioactive glasses were discussed in the previous section and bioactive glass 45S5 was the first of its kind reported by L.L. Hench in the early 1970s and copyrighted by the University of Florida under the name "**45S5 Bioglass$^{®}$**". Hench found that the Na_2O-CaO-SiO_2 phase diagram with constant 6wt % P_2O_5 shows a ternary eutectic in the region E (Figure 1.1). Therefore, the composition of bioactive glass 45S5 was chosen as 45wt% SiO_2, 24.5wt% CaO, 24.5wt% Na_2O and 6wt% P_2O_5 corresponding to the region E in Figure 1.1 [2, 3, 5]. They are commercially found by the name of Novabone$^{®}$, Perioglas$^{®}$, Biogran$^{®}$ depending on their applications.

The name 45S5 denotes 45wt% SiO_2 with 'S' of silicon as the network former and 5 resembles the amount of CaO to P_2O_5 (24.5/5 ~ 5). The composition chosen also fell in the region S, which actually denoted materials capable of bonding with both bone and tissue.

Bioglass$^{®}$ 45S5 is one of the most commonly used bioactive glasses renowned for its bioactivity and commercial viability in its usage as a structural material for biomedical implants. The bonding mechanism of the silica based bioactive glass like 45S5 can be attributed to a series of surface reactions which lead to the formation of a hydroxy carbonate apatite (HCA) layer at the bioglass surface. This phenomenon can be explained by the following two examples.
The important element which catalyses its formation is a layer of porous silica gel with a high surface area. The function of the silica layer towards bonding can be seen in Figure 1.2 where an *in vivo* study of the bonding nature of bioactive glass 45S5 was carried out on a rabbit [17]. Moreover, Figure 1.3 shows another

laboratory *in vivo* study on a rat bone showing the formation of hydroxy carbonate apatite (HCA) layer on a silica layer and finally osteocytes on new bone [3].

However, the reactions, bonding and generation of osteoblasts or bone cells at the implant-bone interface is a complex phenomenon, which is not easy to decipher. The more intensive look at these reactions will be discussed in the section 1.4.

In order to bridge the gap between fundamental knowledge and product development, various work on quantitative methods of bioactive glass characterization including assays for adhesion, viability of biomaterials, proliferation and differentiation of bone cells in response to surface reactions involving synthetic materials. The expected outcome of all these include desired response in the form of cellular growth for different substrates.
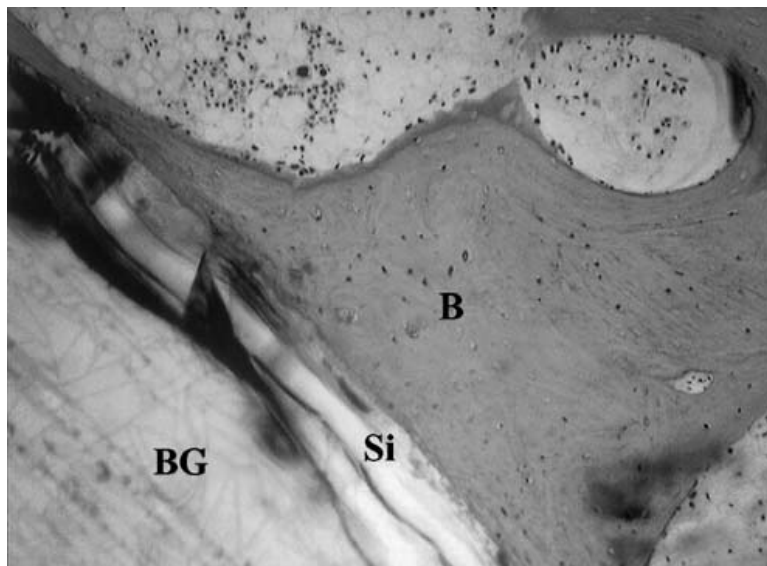
Fig 1.2: Bulk Bioactive Glass 45S5 (BG) implanted in rabbit model. After 12 weeks of implantation, the interface is composed of newly formed bone (B) through a silica (SiO_2) layer denoted in figure by 'Si'. No scale bar was provided in the original figure. Reproduced and adapted with permission and copyright © of the British Editorial Society of Bone and Joint Surgery [17].
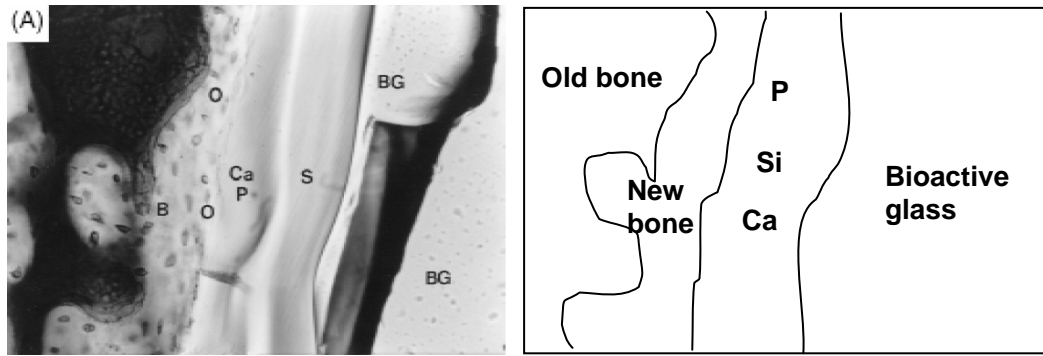
Fig 1.3: (A) Optical micrograph of 45S5 bioactive glass implant (BG) bonded to rat bone (B) after 1 year showing osteocytes or bone cells (O) along with HCA layer (Ca, P) formed on a silica layer. No scale bar was provided in the original figure. Schematic is provided at right. Reproduced and adapted with permission and copyright © of the Journal of American Ceramic Society (John Wiley and Sons) [3].

In this age of interdisciplinary research, it is imperative that a mechanical approach as to how cells behave and remodel on interaction with synthetic materials together with mechanical properties and its improvement has been a consistently a subject of research and innovation. Nevertheless, large scale commercialization of these glass ceramics as monolithic bioimplants has not still been possible because of uncertainty relating to their chemomechanical (alterations in the mechanical properties due to reactions with a biological environment) and mechanochemical (effect of mechanical strain on the dissolution rate of materials) behaviour. Thus, there exists a lack of understanding of the relationship between the mechanical properties of bioactive glasses and their bioactivity. Adjusting the mechanical properties of a bioactive glass without compromising its bioactivity is of prime concern for ongoing research.

1.4.1 Applications of bioactive glass 45S5

Bioactive glass 45S5 is used in implant materials such as cochlear implants, replacement of middle ear bones (DouekMED®), replacement of periodontal defects (Perioglas®, Biogran®), reconstruction of maxillo-facial defects (Novabone®), spinal surgery (Novabone®), repair of orthopaedic cavitary (hip) defects (Novabone®) [18]. Example of bioactive glass 45S5 cochlear implant prostheses is shown in Figure 1.4 (left). Figure 1.4(A) shows X-ray

picture of third molar tooth before extraction. The extracted area was filled with 45S5 glass particulate implant and after three months it was observed that new bone had filled the space so that the X-ray density was equivalent to the normal bone (Figure 1.4 B) [3].

1.5 Bioactivity

The term "bioactivity" means effect of an agent (in this case the implant material) upon a living organism or tissue. However, bioactivity of a bioactive material essentially refers to the positive effect of the implant material with regard to its bonding with the tissue/bone causing surface reactions to catalyze specific influence/interaction with tissue which would promote cell conduction and proliferation on the surface [3], or cause gene activation [19]. But the bioactivity of a bioinert material refers to its ability to interact with the host tissue without releasing any toxins (inflammation or necrosis) or forming scar tissue (fibrous tissue encapsulation) [3]. L.L. Hench has stated many times in his work the diverse kinds of bioactivity exhibited by different bioceramics [3, 20-22] (recall Table 1.1).
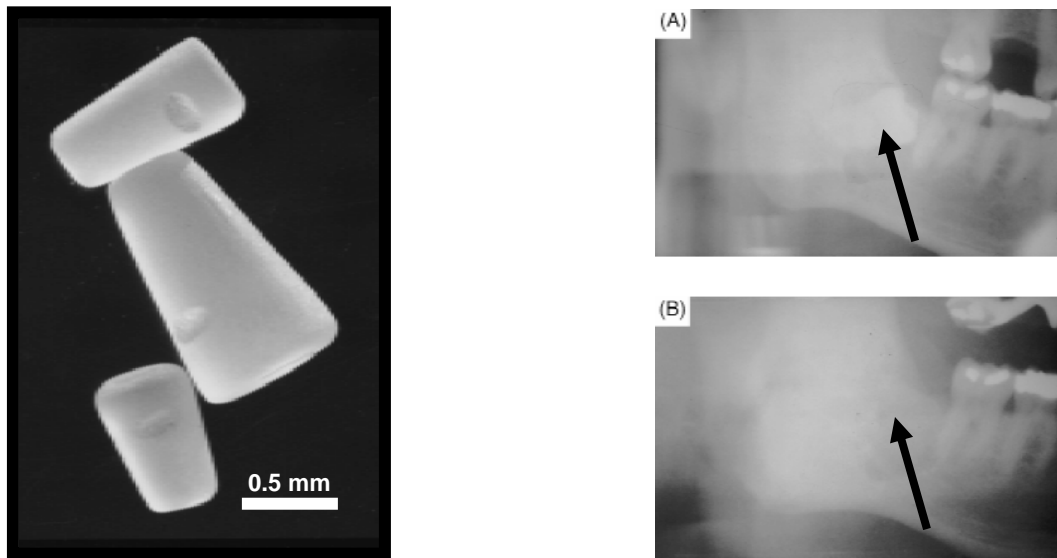
Fig 1.4: (on the left) Bioactive glass 45S5 cochlear implant prostheses; (on the right) X-ray of third molar (impacted wisdom tooth) prior to extraction and implantation with 45S5 particulate (A); 3 months later new bone formed with x-ray density equivalent to normal bone (B). Reproduced and adapted with permission and copyright © of the Journal of American Ceramic Society (John Wiley and Sons) [3].

The different surface reactions that the implant materials create determine the extent of bioactivity of a bioactive glass. However, different stages of reaction that occur in the tissue/bone – implant interface are complex. Adhesion of bioglass on a tissue undergoes various surface reactions resulting in formation of hydroxyl carbonate apatite layer. There are 12 stages involved and the stages 1-11 are shown in Table 1.2 [23, 24] while stage 12 is the proliferation of bone.

Reactions 6-12 occur on the tissue side of the interface, stages 6-7 usually overlap with stages 3-5 while the rest occur on the material side of the interface. Various *in vitro* analyses has been carried out in order to confirm the first 5 reactions that occur on the implant surface by immersion in various immersion mediums such as simulated body fluid (SBF), phosphate buffer solution (PBS), tris buffer solution. The formation of hydroxy carbonate apatite occurred in stage 5, which has been the benchmark for most of the *in vitro* research being carried out in the field of bioactivity of bioceramics.

In the early years, it was assumed that the formation of hydroxyl carbonate apatite (HCA) by resorbable bioceramics was the most critical stage towards new bone/tissue formation (i.e. towards bioactivity) [3, 11, 20, 25]. However, recent research has shown that HCA formation is undoubtedly important but not the paramount stage in tissue regeneration [2]. The prime phenomenon is controlled release rates of ionic products on dissolution of the implant material when it comes in contact with the body fluid. Figure 1.5 shows schematic diagram unfolding the path towards formation of new bone after implantation as described by Hench [2]. If the implant material was able to release ions at a controlled rate on dissolution, only then can these ions can trigger cell response in osteoblast progenitor cells. These osteoblast progenitor cells in turn undergo duplication of chromosomes in the nucleus followed by mitosis to form osteoblasts which again undergo similar cycles before finally leading to bone growth. However, bone growth is preceded by protein cell attachment on the interface and finally proliferation of osteoblasts. The cells unable to undergo mitotic cycles (osteocytes) become involved in the production and mineralization of the extra

cellular matrix (ECM) after collagen and HCA (formed on implant material) bonding as the final step towards bone formation. The formation of ECM is very important as it provides the mechanical strength and toughness to the newly formed bone.

SEQUENCE OF INTERFACIAL REACTIONS INVOLVED IN FORMING A BOND BETWEEN TISSUE AND BIOACTIVE CERAMICS

SURFACE REACTION STAGES	
11	CRYSTALLIZATION OF MATRIX
10	GENERATION OF MATRIX
9	DIFFERENTIATION OF STEM CELLS
8	ATTACHMENT OF STEM CELLS
7	ACTION OF MACROPHAGES
6	ADSORPTION OF BIOLOGICAL MOIETIES IN HCA LAYER
5	CRYSTALLIZATION OF HYDROXYL CARBONATE APATITE (HCA)
4	ADSORPTION OF AMORPHOUS Ca + PO$_4$ + CO$_3$
3	POLYCONDENSATION OF SiOH + SiOH → Si-O-Si
1 & 2	FORMATION OF SiOH BONDS
	BIOACTIVE GLASS

LOG TIME (HOURS) — 1, 2, 10, 20, 100

Table 1.2: Sequence of interfacial reactions leading to tissue-bioceramic implant bonding. Reproduced and adapted with permission and copyright © of the Journal of Sol-Gel Science and Technology (Springer) [24].

1.5.1 Bioactivity of bioactive glass 45S5

Numerous comparative studies on the bioactivity of bioactive glass 45S5 versus other bioactive glasses have included varied compositions, properties, biomineralization rates, crystallinity and processing modes, in order to assess their suitability in their usage as bioimplants [8, 15, 26-30].
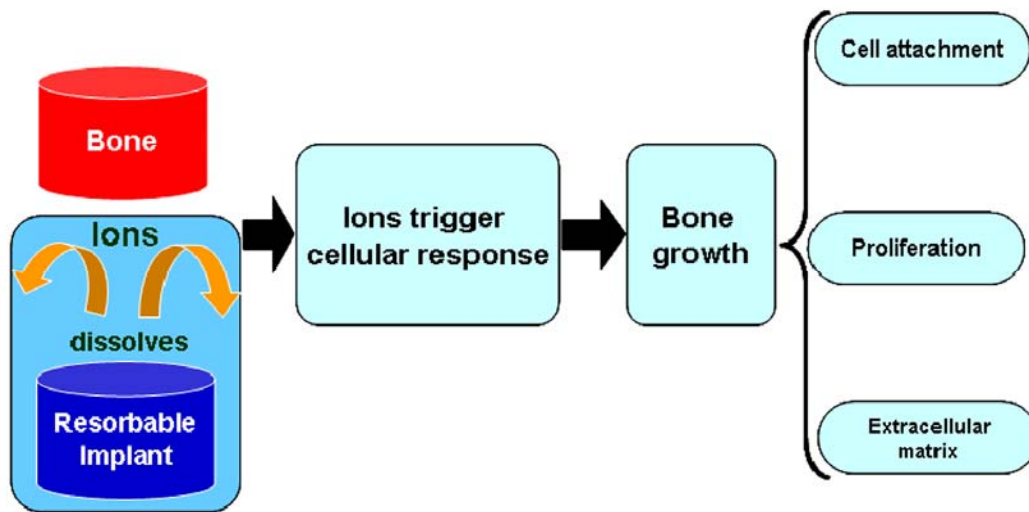
Fig. 1.5: Schematic showing the path from dissolution of the implant to final bone formation.

One such comparative *in vitro* example is shown in Figure 1.6, which reveals the morphology of apatite structures formed on bioglass 45S5, 58S and 77S after being soaked for three different durations of time [30]. As seen in the images, formation of apatite layer does not take place in melt derived bioglass 45S5 until 4 hrs unlike 58S and 77S. The structure of sol gel produced bioglass 58S and 77S were porous and hence ions dissolve more easily than melt casted 45S5. For 45S5, Na^+ ions dissolved first followed by Ca^{2+} ions. Hence, biomineralization of 45S5 was slow first and then it picked up rapidly. Moreover, the layer of apatite formed on the 45S5 and 58S was hydroxyl carbonate apatite while that in 77S was hydroxyl apatite due to its high SiO_2 content.

Since most of the earlier researches had already revealed the properties and behaviour of bioactive glass 45S5, recent studies have taken a trend towards optimising its mechanical properties and deciphering the effects of different stresses, thermal treatments and crystallinity on bioactivity and mechanical properties so that it can ultimately be inducted into the health care industry as a full fledged implant material whose properties can be varied to provide varied effects depending on the needs and applications [23, 26, 31-35].
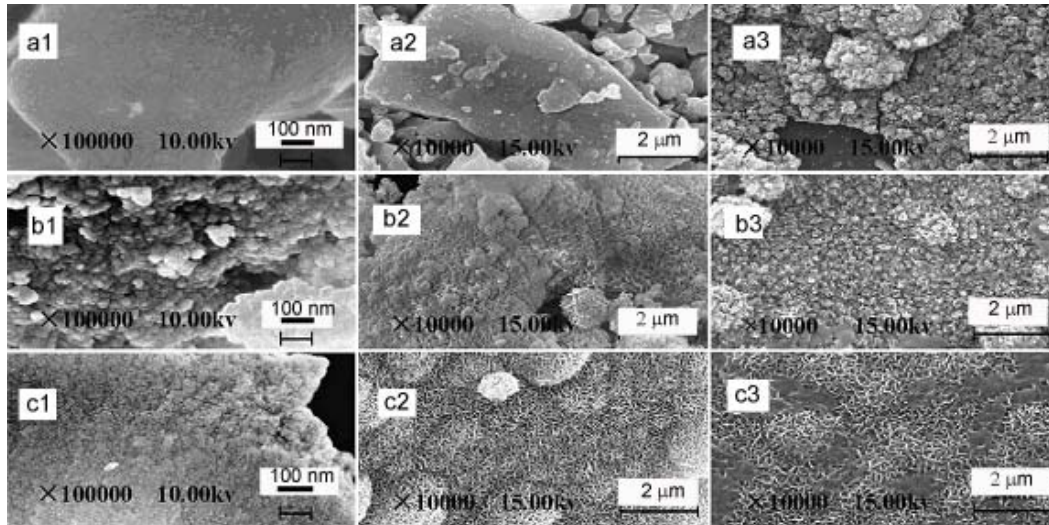
Fig 1.6: SEM images showing morphology of bioactive glass (a) 45S5 (b) 58S (c) 77S immersed in SBF for (1) 0 hr (2) 4hrs (3) 96hrs. Reproduced and adapted with permission and copyright © of Applied Surface Science (Elsevier) [30].

An example of this new trend in optimising properties of bioactive glass 45S5 was the *in vitro* studies recently by Nychka *et. al* [28, 36] revealing the dissolution phenomenon of bioactive glass 45S5 explained by the mechanochemical and chemomechanical behaviour of these materials under the influence of stresses and strains. Dissolution behaviour of amorphous bioactive glass 45S5 subjected to residual stress induced by indentation load were studied by Nychka *et al.* [28]. These studies were conducted by inducing compressive residual stress through microindentation and immersing the samples in phosphate buffer solution (PBS) for different durations of time. Figure 1.7 reveals a minimum load above which there is appreciable residual stress induced in the bioglass sample to affect dissolution. Moreover, higher indentation loads suppress the dissolution of bioglass surrounding the indents. Tensile stresses at the crack tips have higher dissolution rate than the bulk surface and also the main indent area which is under compressive stresses.

In vitro analyses also involved testing the bioactivity of bioactive glass 45S5 in various immersion mediums and thereby standardize a medium which was the closest in composition and behaviour with the body fluid [35, 37].
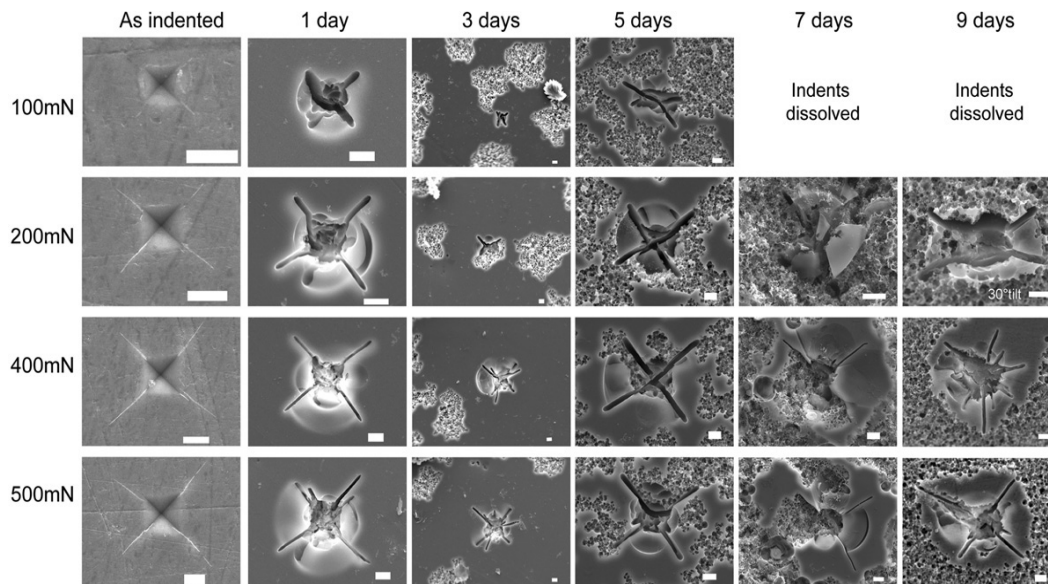
Fig 1.7: Secondary electron micrographs of indented samples under different loads *vs.* the immersion time in PBS. Reproduced and adapted with permission and copyright © of the Journal of Mechanical Behaviour of Biomedical Materials (Elsevier) [28].

Moreover, *in vivo* analysis of bioactive glass 45S5 has also been carried out to show great potential in tissue-regeneration [15, 38-40]. The effects on implantation in pictorial form were shown in the sections explaining the applications of bioactive glass 45S5.

1.6 Mechanical properties: a review

Bridging the gap between fundamental knowledge and product improvement requires quantitative methods of biomaterials characterization to be formulated including assays for bone adhesion and better mechanical properties. Resorbable implant materials endure some form of mechanical loading during manufacture or whilst in service. It has been mentioned before that a huge hindrance in inducting bioactive glasses in to the health care industry as implant materials is their poor mechanical properties in terms of fracture toughness, strength, impact resistance which are insufficient for life long service (>20 years) [20]. Comparative mechanical properties of bioactive glass 45S5 and soda lime glass are provided below [3, 36, 41, 42]:

Mechanical Properties	Bioactive glass 45S5	Soda lime glass
Density (g/cm^3)	2.65 [3]	2.5 [42]
Vickers Hardness (HV)	458 ± 9.4 [3]	581 [41]
Young Modulus (GPa)	35 [3]	69 [42]
Fracture Toughness (MPam$^{1/2}$)	0.11 [36]	0.7 - 0.8 [42]

Table 1.3: Mechanical properties of bioactive glass 45S5 and soda lime glass [3, 36, 41, 42]. Source is indicated within brackets beside the property data.

Thus, load bearing applications with these monolithic bioimplants have been limited. In the past, metallic alloys and ceramic composites have been used but they have issues like toxicity and stress shielding (elastic modulus mismatch) [29]. Efforts have been made to toughen bioactive glass ceramics by introducing composites in the form of particles [33, 40, 43-46], particle composites [47], glass ceramic composites [48, 49] and coatings [50-53]. "Glass ceramics" were developed by special heat treatment of particular glass compositions to present a uniform fine dispersion of crystals in glassy phase matrix, which gave them a cutting edge over the conventional "glass" in terms of properties like higher strength and impact resistance, low coefficient of thermal expansion, low dielectric loss and a range of optical properties from clear to opaque or white [54, 55]. Thereby, another thought to improve the stress carrying capability in bioactive glass ceramics would be phase transformation into partially crystalline bioactive glass. Moreover, bioactivity or rate of hydroxyl carbonate apatite (HCA) formation for fully and partially crystallized bioactive glass ceramics yielded assorted results [15, 23, 56, 57]. Chen *et al*. also revealed the ability of mechanically competent crystalline sintered bioactive glass 45S5 powder to form biodegradable and bioactive calcium phosphate upon immersion in simulated body fluid [26]. Our knowledge of mechanical properties as they relate to crystallization and toughness are rather well established in the field of glass

ceramics, but our understanding is lacking with regard to the impact of such variables on bioactivity.

1.7 Crystallization

Numerous crystallization kinetics studies have been conducted for bioactive glass 45S5 [27, 31, 34, 56, 58, 59], however a correlation between the effects of crystallization, mechanical properties and bioactivity has rarely been made. As mentioned above, an idea to increase toughness in bioactive glass 45S5 was to crystallize it into partially crystalline structure so that it would have an optimum amount of crystals dispersed in an amorphous matrix. This idea can be clearly explained by Figure 1.8 which shows the crack propagation in two different glass compositions containing 10% volume fraction of thoria [60]. In Figure 1.8A the crystal size and dispersion is not optimum and hence cracks propagate in a straight path even through the crystalline particles. However, Figure 1.8B shows that for the same volume fraction of crystals if properly sited and dispersed the crack path winds around the crystals, thereby lengthening the crack path which essentially increases the fracture toughness of the material. If bioactive glass 45S5 were to be crystallized in such a way so as to form a partially crystallized glass ceramic with the optimum amount of crystal fraction, crystal size and dispersion then it might exhibit improved fracture toughness.

Hence, controlled crystallization seemed to be a novel idea in improving the mechanical properties of bioactive glass 45S5. 'Controlled crystallization' means appropriate knowledge of the processing conditions, thermal treatment cycles, controlled heating and cooling rates, crystallization kinetics and the optimum amount and size of crystals needed to produce the partially crystallized sample with enhanced mechanical properties. Nonetheless, it is important to understand that introduction of better mechanical properties in this partially crystallized bioactive glass 45S5 sample should not compromise with the bioactivity of this material.
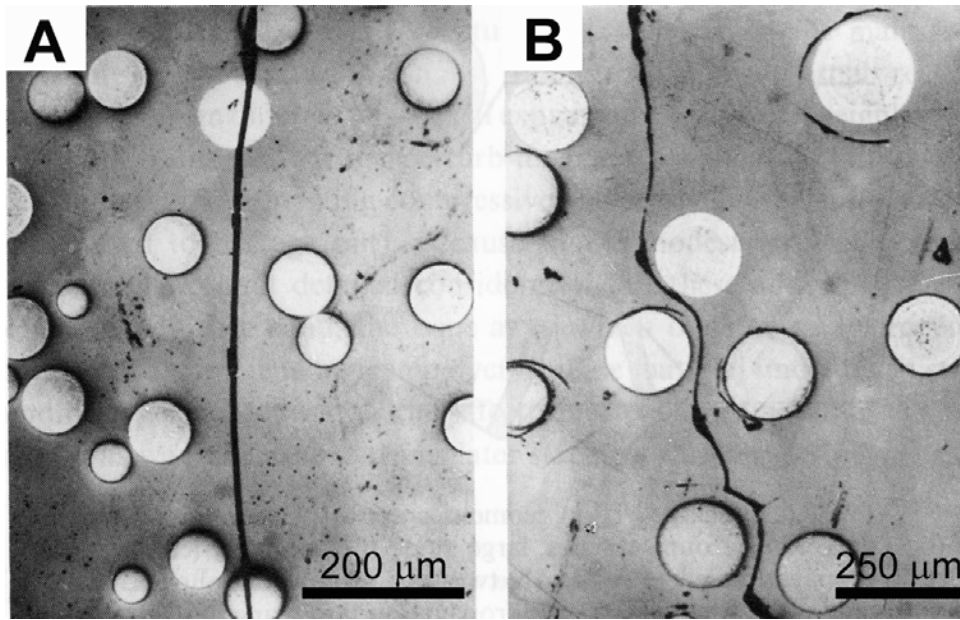
Fig. 1.8: Crack paths in two different glass compositions containing 10% volume fraction of thoria spheres. Reproduced and adapted with permission and copyright © of the Journal of Materials Science (Springer) [60, 61].

1.7.1 Crystallization kinetics

Recent work by Clupper and Hench [23, 34, 58, 62], who had done quantitative evaluations on the effect of crystallinity on the apatite formation on bioactive glass 45S5, revealed that the crystalline phase combeite ($Na_2Ca_2Si_3O_9$) slightly decreased the HCA forming kinetics on the bioactive glass sample but did not totally suppress it [23]. The rate of HCA formation as a function of volume fraction of crystallinity determined by Peitl *et al.* [23] is shown in Figure 1.9.

Different techniques have been used to determine the crystallization kinetics of various bioactive glasses powders such as using differential thermal analysis / differential scanning calorimetry (DTA/DSC) [27, 31, 34, 59, 63] or calculation of crystalline volume fraction from optical micrographs [23, 58].

In the early 1940s Michael Avrami developed a theory of diffusional phase change kinetics [64-66] known as the Avrami Equation, which describes changes in the volume of crystals as a function of time during crystallization at a

particular temperature. Phase transformations, including glass crystallization kinetics are most often studied using the Avrami equation given as:

$$f = 1 - \exp\left(-kt^n\right) \qquad (1.1)$$

where f is the crystalline volume fraction transformed isothermally after time t, k is the rate constant and n is the Avrami exponent.

The more common expression to linearize the Avrami equation (1.1) is as follows:

$$1 - f = \exp\left(-kt^n\right)$$
$$-\ln\ln(1-f) = \ln k + \ln t \qquad (1.2)$$
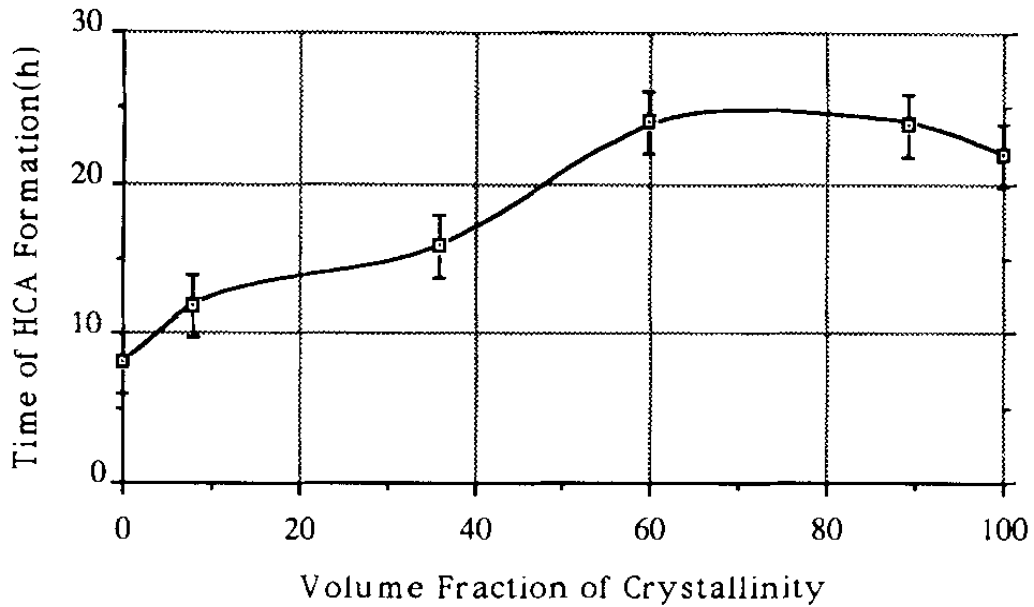
Fig. 1.9: Variation in rate of HCA formation with increasing volume fraction of crystallinity. Reproduced and adapted with permission and copyright © of the Journal of Biomedical Materials Research (John Wiley and Sons) [23].

18
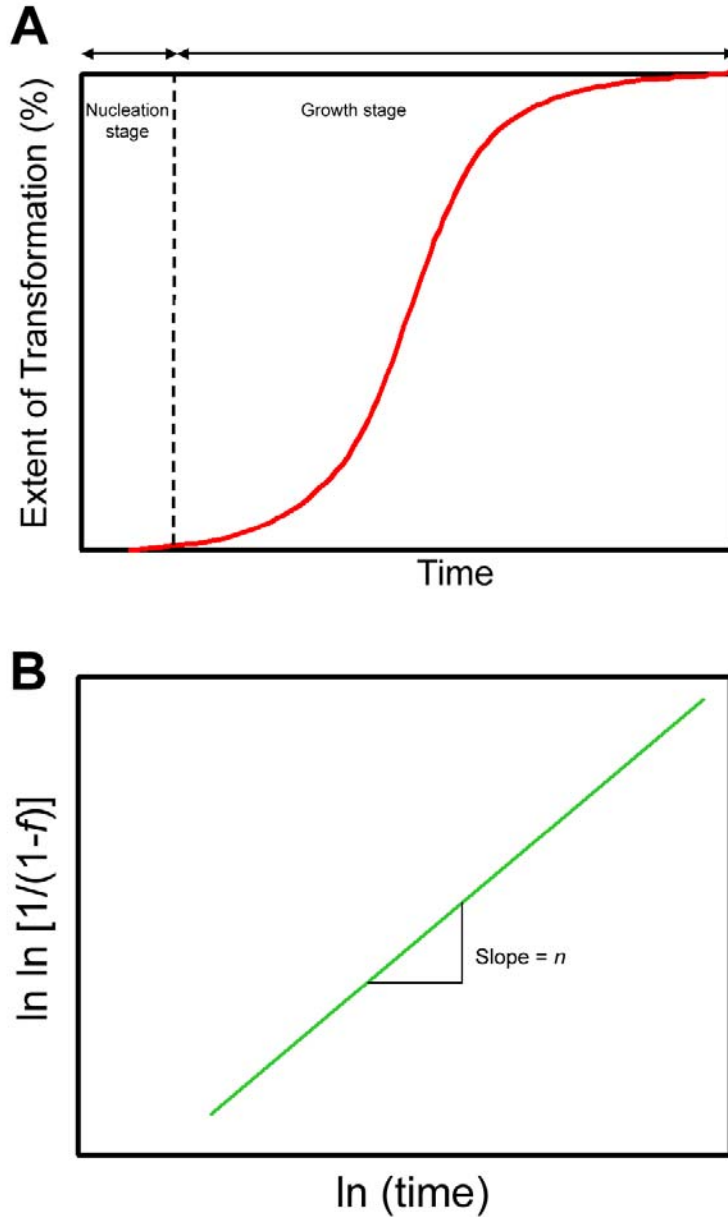
Fig. 1.10 (A) Amount of transformation *vs.* time corresponding to the Avrami equation (Equation 1.1) (B) Linear representation of the Avrami equation (Equation 1.2)

A pictorial representation of Equation 1.1 and 1.2 are shown in Figure 1.10. Figure 1.10A shows that the phase transformation follows a characteristic S-shaped or sigmoidal profile where the transformation rates are low at short and long times but exponentially high in between. The initial slow rate can be attributed to the time required for a significant number of nuclei of the new phase

to form and begin growing. During the intermediate period the transformation is rapid as the nuclei grow into grains consuming the parent phase while more nuclei continue to form in the remaining parent phase. Once the transformation begins to near completion there is little untransformed material for nuclei to form in and the production of new phase begins to slow. Further, the grains already formed begin to touch one another, forming a grain boundary where growth stops. The linear form of the Avrami equation is pictorially shown in Figure 1.9B where the slope of the straight line gives the value of 'n' and the intercept on the Y axis gives the value of 'ln k' from which the rate constant 'k' values can be determined.

The interpretation of Avrami exponent 'n' relates to the mode of transformation. The value of 'n' varies from 1 to 4. The value 1 indicates 1 dimensional needle-like linear second phase particles forming from the parent phase, 2 indicates two dimensional transformation, 3 indicates three dimensional bulk transformation and 4 signifies three dimensional growth supported by sporadic nucleation. Thus each dimension of growth increases the value of 'n' by 1 [67, 68]. The interpretation of 'n' values in terms of crystallization types is given in Table 1.3.

n	Crystal morphology	Type of crystallization
1	needle like crystals (1-dimensional)	surface
2	plate like crystals (2-dimensional)	surface
3	3-dimensional growth of crystals	bulk
4	3-dimensional growth of crystals	Bulk (with sporadic nucleation)

Table 1.4: The interpretation of Avrami exponent 'n' values with respect to crystal morphology and type of crystallization.

The Avrami parameters have been determined with DTA/DSC techniques by obtaining the glass transition temperature, crystallization temperature and melting temperature from the TGA-DTA plots. The crystallization kinetics was then studied using a non isothermal method by DTA. The activation energy for crystallization (E_a) was calculated from the Kissinger equation [69]:

$$\ln\left(\frac{\alpha}{T_p^{\ 2}}\right) = -\left(\frac{E_a}{RT_p}\right) + \ constant \qquad (1.3)$$

where E_a = activation energy (kJ/mol); α = heating rate (K/min); T_p = peak crystallization temperature (K); R = gas constant (8.314 JK^{-1} mol^{-1}).
By plotting [$-\ln (\alpha/ T_p^2)$] *versus* $1/T_p$ the activation energy of crystallization can be calculated from the slope of the line.

The mechanism of nucleation and growth of crystals defined by the Avrami exponent 'n', was determined by the Augis–Bennet equation [69].

$$n = \left(\frac{2.5}{W}\right)\left(\frac{RT_p^{\ 2}}{E_a}\right) \qquad (1.4)$$

where W (K) is the full width of the crystallization peak at the half maximum (FWHM).

However, these experiments were performed for powdered or tape cast bioglass 45S5 samples and application of the above equations yielded the value of 'n' $\sim$ 0.95-1 indicating surface crystallization [31, 34]. Whether the same was true for bulk samples of 45S5 bioactive glass, still needs to be confirmed because Koga *et al.* found that transition from surface to bulk crystallization occurs with increasing particle size in Na_2O-CaO-2SiO$_2$ glasses [70]. Though transmission electron microscopy was performed to confirm the crystalline combeite phase [63] but the confirmation of the mode of crystallization was not established by imaging techniques.

Moreover, research have been conducted to obtain optical micrographs of partially crystallized bioactive glass samples (crystallization at a particular temperature for varied durations of time) from which the area fraction of crystalline phases were formulated by point counting stereology techniques. These area fractions were assumed to be equivalent to the volume fraction of crystalline phase formed [23, 58] to obtain samples with various amounts of crystallinity. Although different volume fractions of crystalline samples were obtained, these studies have only compared the rate of HCA formation with increasing crystallinity (recall Figure 1.9). No attempts have been made to study the crystallization kinetics of bioactive glass 45S5 by obtaining crystalline volume fraction from micrographs. Hence, crystallization kinetics (mode of crystallization and morphology) in bulk bioactive glass 45S5 is still ambiguous and needs to be studied. Information on crystallization kinetics is important while trying to improve the mechanical property of monolithic bioactive glass 45S5 by making it a glass-ceramic or when a monolithic sample is crushed into powder and then sintered (which will induce crystallization) for clinical applications.

The knowledge of crystallization kinetics can only be said to be fulfilled if the time-temperature transformation (TTT) curves of bioactive glass 45S5 are available for precise understanding of the thermal treatments required to obtain a particular volume fraction of crystalline phase in bioactive glass 45S5. A schematic of a TTT curve is shown in Figure 1.11 which shows the means of obtaining a TTT curve from an isothermal transformation-time plot similar to that obtained from an Avrami equation (recall Figure 1.10A).

Earlier studies attempted to construct the TTT curves of other glasses [71, 72]. As a matter of fact, the construction of TTT curves indicative of crystallization kinetics in bulk bioactive glass 45S5 has not been established. Lefebvre et al. studied the structural transformations occurring in powder Bioglass® 45S5 as a function of temperature [27]. They found that above 550°C phase separation into two immiscible phases (silica rich and phosphate rich) take place and crystallization starts at 610°C when combeite starts forming and above

22
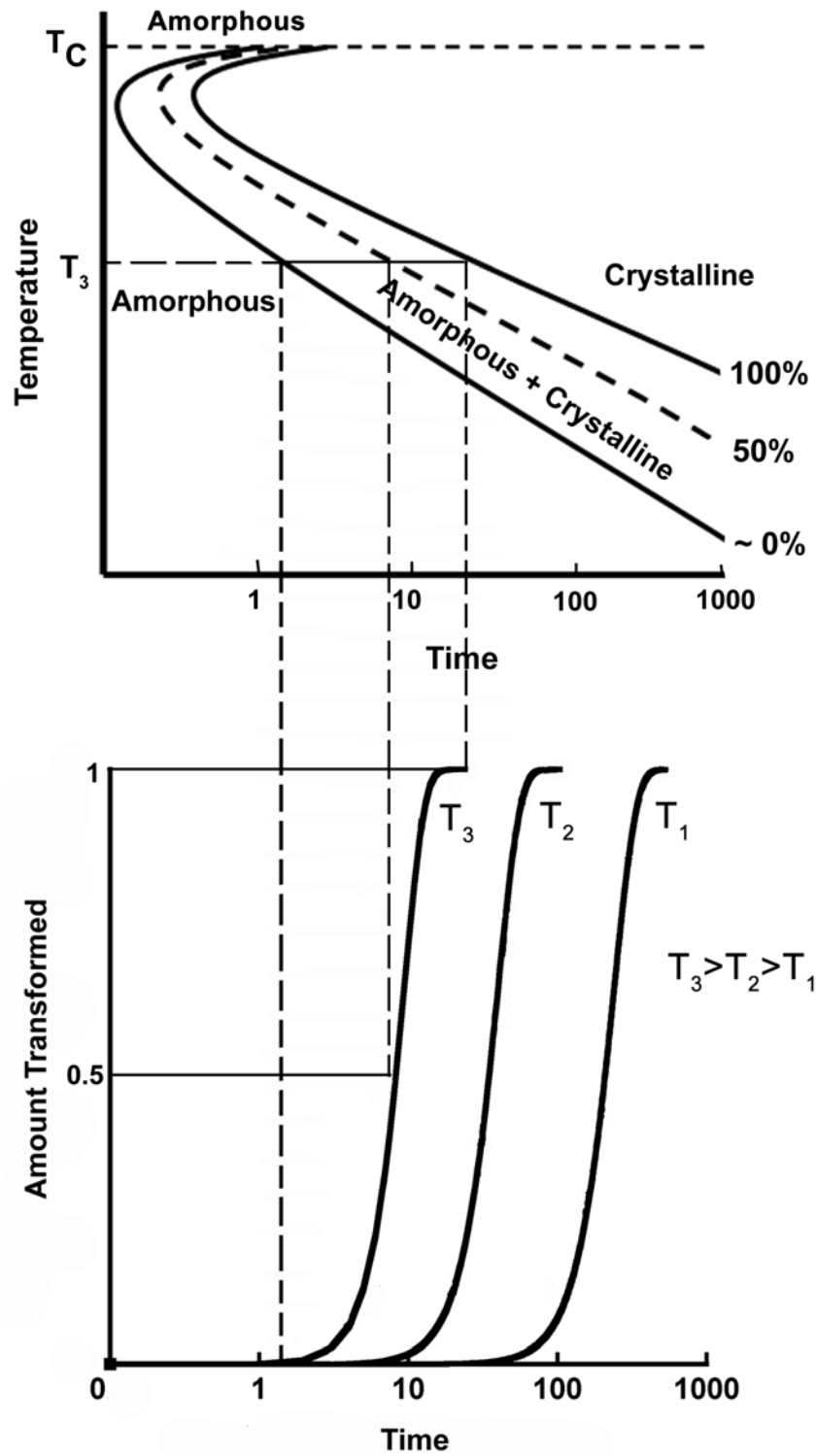
Fig. 1.11: Schematic diagram of TTT curve obtained from isothermal transformation-time curve.

800°C a new phosphate containing phase forms called silicorhenanite ($Na_2Ca_4(PO_4)_2SiO_4$). In addition to that, they determined the volume fraction of crystalline phase by isothermal measurements between 620 to 680°C using DSC technique. The powder samples were held at the desired temperatures between 620°C-680°C for 90 minutes to obtain the DSC data. The exothermic crystallization peaks at each temperature were measured. The area of each peak at a particular temperature normalized by the total area was calculated. This provided the required data of the degree of transformation at a given time and temperature which was used to construct the TTT curve. This is shown in Figure 1.12 [27]. The TTT curves formulated provided transformation curves from 10%-90% in the crystallization temperature range of 620 to 680°C. It was evident from these plots that the nose of the TTT curve did not appear as the experimental range of 620 to 680°C was below the temperature at which the fastest crystallization takes place. Therefore, this TTT curve does not provide a comprehensive detail of all the phase transformation kinetics.
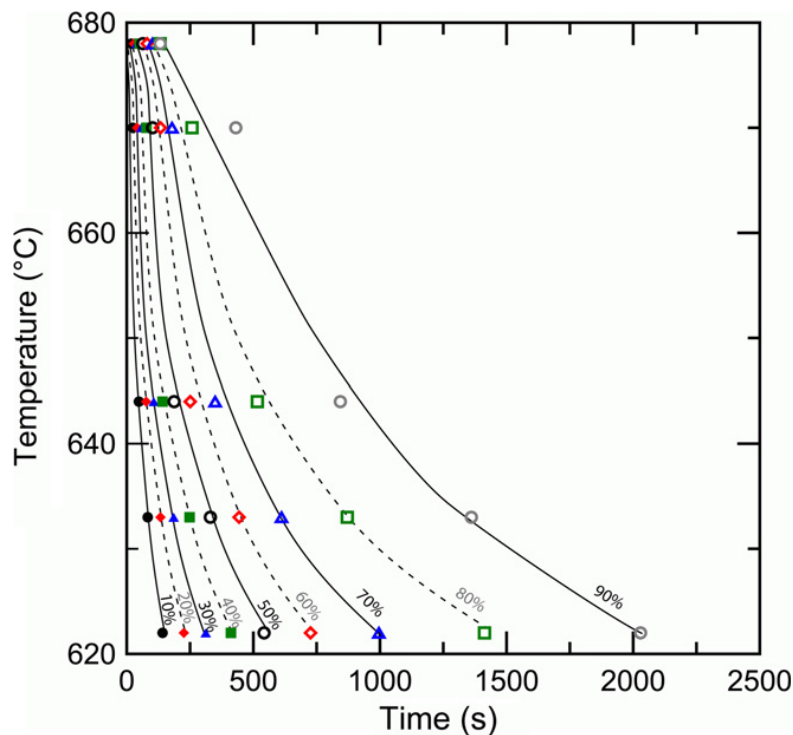
Fig. 1.12: TTT curves constructed for bioactive glass 45S5 by Lefebvre *et al.* Reproduced and adapted with permission and copyright © of Acta Materialia (Elsevier)[27].

1.8 Summary of literature survey

The above discussion in previous sections about earlier research on the crystallization, bioactivity and mechanical properties have revealed that

- Use of bioactive glass 45S5 as implant materials would be problematic due to its poor mechanical properties (recall Table 1.3). No attempts at improving its mechanical properties and without compromising the bioactivity have been made to date.

- Though bulk bioactive glass 45S5 samples with various amounts of crystallinity were used to determine the rate of HCA formation, crystallization kinetics of bulk bioactive glass 45S5 are still ambiguous.

- Construction of TTT curve for bulk bioactive glass formulating the entire crystallization kinetics has not been established.

1.9 Motivation

From the previous section it has been mentioned that one of the main hindrances of using bioactive glass as implants is its poor mechanical properties (recall Table 1.3). One way to counter that problem would be to produce 45S5 glass ceramics with optimum crystal size, crystal dispersion, and volume fraction which would hinder crack propagation by deflecting crack paths around crystals which would increase the fracture toughness (as seen in case of thoria crystals, recall Figure 1.8). However, production of the best bioactive glass ceramic with enhanced mechanical properties needs appropriate knowledge of the crystallization kinetics and TTT curves. The new glass ceramic with improved mechanical properties which contain a crystalline phase must maintain the bioactivity or dissolution response of the material. Peitl *et al.* previously proved that though bioactivity decreased but was not totally suppressed by the crystalline phase in bioactive glass 45S5 (recall Figure 1.9).

Therefore, an effort has been made to understand the effect of crystallinity on the mechanical and mineralization behaviour of bioactive glass 45S5 ceramics, which investigates Avrami crystallization kinetics of bioactive glass at different crystallization temperatures by studying the crystallization behaviour as a function of time. Attempts have been made to conduct comparative studies on crack propagation path in amorphous and partially crystallized bioactive glass using micro-indentation technique; aspiring to support the hypothesis "partially crystalline bioactive glass with optimum amount of crystalline phase in an amorphous matrix might hinder crack propagation, thereby improving fracture toughness". With the object of comprehending the mineralization behaviour of crystalline phase as compared to its amorphous counterpart within the same sample, *in vitro* tests of partially crystallized bioactive glass in a buffer solution were performed.

The motivation generated for this research was three fold:
1. Amorphous bioactive glass 45S5 has poor mechanical properties.
2. Crystallization kinetics of bulk bioactive glass 45S5 is ambiguous.
3. Mechanical properties (crack propagation, modes of fracture) and mineralization behaviour (under immersion) for partially crystalline bioactive glass 45S5 is still not fully known.

The long term goal of this research is "*to produce a partially crystalline bioactive glass with optimum crystalline phase, crystal size and crystal dispersion which possesses better mechanical properties and does not compromise the inherent bioactivity of the material.*"

1.10 Hypothesis and objectives

In order to test the **hypothesis:**
"***Partially crystalline bioactive glass 45S5 with a dispersed crystalline phase in an amorphous matrix should hinder crack propagation, thereby improving fracture resistance***"

this research was conducted with the following objectives:

1. Characterize Avrami Kinetics of crystallization: determine the crystalline volume fraction as a function of time at different crystallization temperatures. Study the effect of crystallization temperature and heating rates. Determine the mode and rate of crystallization and construct a TTT curve from the data.

2. Crack Propagation: Comparative crack propagation and fracture surface study in amorphous and partially crystalline bioactive glass to compare mechanical properties.

3. Mineralization: Comparative mineralization behaviour study of the amorphous and crystalline regions in a partially crystalline bioactive glass immersed in a simulated buffer solution.

CHAPTER 2

Materials and methods

Different sets of experiments were designed in order to execute the objectives mentioned in section 1.10. A brief summary of experiments conducted with their expected outcome is provided below in Table 2.1.

Objectives	Experiments*	Expected outcome
Study of crystallization kinetics	Heat treatment	Obtain samples with a variation in %crystallinity
		Formulate Avrami kinetics
	Dye penetrant test	Characterize void formation during crystallization
Crack Propagation study	Heat treatment	Crack path as a function of crystallinity
	Microindentation	
	Thermal shock resistance test	Mode of fracture in amorphous and partially crystalline glass ceramic
	In vitro immersion	Crack propagation upon drying in mineralized layer formed atop amorphous and crystalline phases
Mineralization study	Heat treatment *In vitro* immersion	Mineralized layer formed atop crystalline and amorphous phases

* Sample preparation was carried out for all experiments, as was characterization.

Table 2.1: Different sets of experiments designed along with their expected outcomes in order to fulfill the objectives of this study.

2.1 Material

Mo-Sci Health Care, L.L.C (Rolla, MO, USA) provided melt cast, annealed and amorphous 12 mm diameter cylindrical rods of bioactive glass 45S5 as shown in Figure 2.1(A). The chemical composition of these rods as provided by Mo-Sci Health Care L.L.C (Rolla, MO, USA) was 45 wt% SiO_2, 24.5 wt% Na_2O, 24.5 wt% CaO and 6 wt% P_2O_5.

2.2 Sample preparation

2.2.1 Sectioning

The cylindrical rods of bioactive glass 45S5 were sectioned into 3mm thick discs (Figure 2.1B) using a Slow Speed Saw (Techcut 4[TM], Allied High Tech Products Inc.) with a diamond wafering blade (Allied Hightech, Diamond metal bonded) using isopropyl alcohol as the lubricant/coolant.
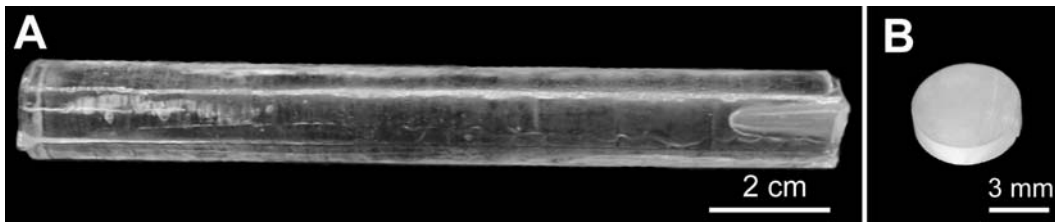
Fig. 2.1: (A) 12 mm diameter cylindrical rod of bioactive glass 45S5 as received from Mo-Sci Health Care, L.L.C, Rolla, MO, USA. (B) 3mm thick disc of bioactive glass 45S5 after sectioning.

2.2.2 Mounting

In order to make grinding and polishing of these discs convenient, they were mounted on piston and ring mounting jigs. The piston was inserted inside the ring and held in place with a screw. The bioactive glass discs were mounted on the piston by using thermoplastic mounting wax (Crystalbond[TM] 509). The mounting wax was placed on the piston and heated to ~ 170°C on a hot plate (Cimarec[TM] HP130915) which melted the wax. The bioactive glass disc was placed on the melted wax which upon cooling fixed the disc in place on the piston. Care was taken to place the smoothest surface face down on the wax and swirl the disc around the melted wax to remove any air bubbles underneath. The mounting jig was assembled by holding the piston with the disc inside the ring using a screw such that the top surface of the bioactive glass disc aligned with the peripheral surface of the ring. In order to do this, the mounting jig was placed upside down on a Kimwipe and the piston was pushed slightly harder on the inside of the jig while tightening the screw at the same time. The mounting jig was checked for proper alignment by running the edge of a clean glass slide

across the surface. If the glass slide hits the bioactive glass disc, the alignment procedure must be repeated again. All the steps required in the sample mounting process have been shown in Figure 2.2.

2.2.3 Grinding and polishing

The mounted bioactive glass discs were ground on silicon carbide papers (Allied High Tech Products Inc.) fixed to a grinding wheel (Twinprep 3^{TM}, Allied High Tech Products Inc.) in the order: 320, 400, 600, 800 and 1200 grit. Isopropyl alcohol was used as the lubricant/coolant while grinding. Care was taken to swipe the surface of samples with a cotton swap dipped in acetone, in between grinding stages so as to avoid any contamination by particles of other grits.

Subsequent polishing was carried out on polishing cloths mounted on stainless steel support plates, using polycrystalline diamond paste in the order 6, 3, 1 and 0.5μm size with Blue Lube™ as the oil based lubricant/coolant (Allied High Tech Products Inc.). Three different types of polishing cloths (Allied High Tech Products Inc.) were used depending on the particle size of the diamond paste used – Gold Label™ for 6μm size, Imperial™ for 3μm and 1μm size and Final P™ for 0.5μm size. Compressed air was blown on the polishing cloth from time to time to get rid of any contaminant particles that could scratch or contaminate the sample surface.

2.2.4 Dismounting and cleaning

Once the first side was polished, it was dismounted by dissolving the mounting wax in acetone. It was then flipped upside down and remounted for grinding and polishing the other side. After grinding and polishing both the side the sample was finally dismounted again and thoroughly swiped on all the sample surfaces with a cotton swab dipped in acetone. Then the samples were ultrasonically cleaned in a Branson (Model 3510) Ultrasonic Cleaner (Figure 2.3A). Ultrasonic cleaning involved cleaning of the samples first, in an acetone bath for 30 minutes followed by an isopropyl alcohol bath for another 30 minutes. The acetone and isopropyl alcohol bath consisted of a tightly capped 200ml glass

bottles filled either with acetone or isopropyl alcohol to the top. The samples were first immersed in the acetone bottle while this bottle was placed in water stored in the ultrasonic cleaner. A similar procedure was performed for ultrasonic cleaning in the isopropyl alcohol bath. Finally the samples were dried with compressed air and stored in a desiccator.
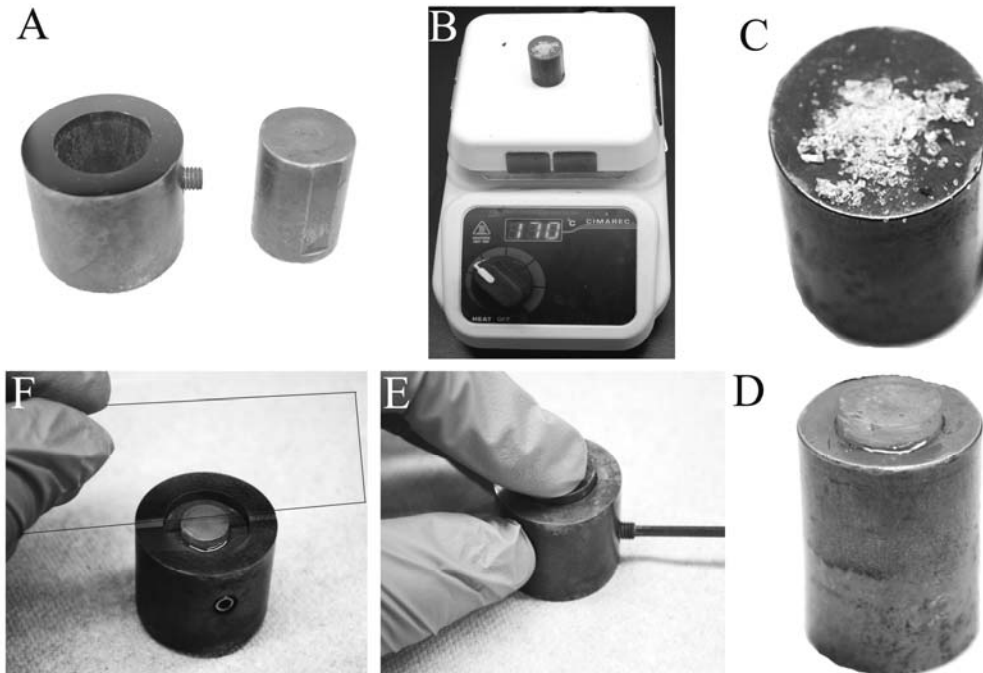
Fig. 2.2: Clockwise (A) Mounting jig parts - ring and piston cylinders, (B) mounting wax on piston being heated on a hot plate, (C) closer view at the wax on the piston, (D) Sample mounted on the solid cylinder after the wax melted, (E) Aligning the sample surface with the peripheral surface of the ring, (F) Alignment check by running the edge of a clean glass slide.
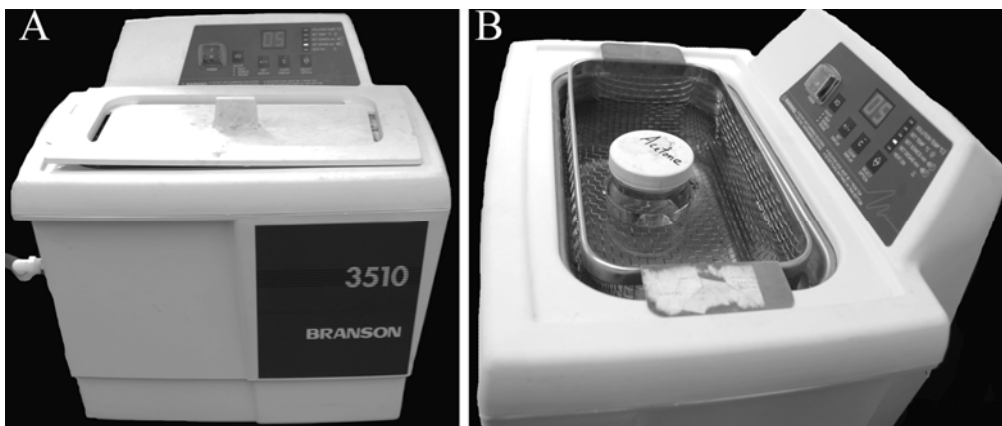
Fig. 2.3: (A) Ultrasonic Cleaner, (B) Sample in an acetone bath placed in the ultrasonic cleaner.

2.3 Heat treatment

2.3.1 Annealing

Bretcanu *et al*. found that the bioglass 45S5 crystallizes between 600°C and 750°C [31] while an earlier study by Lefebvre *et al*. showed structural changes and alterations occurring in bioactive glass 45S5 just after its glass transition temperature of 550°C [27]. So an annealing temperature of 460°C was chosen in order to relieve any induced and residual stresses present in the bioactive glass after sample preparation, as this temperature was much lower than the temperature when phase transformation and phase separation begins. Hence after sample preparation, the amorphous bioactive glass samples were placed inside a muffle furnace (Thermo Scientific, Model: F48055) and the temperature was ramped up at 20°C/min to an annealing temperature of 460ºC. The samples were annealed for 8 hrs at that temperature and then furnace cooled (approximate cooling rate of ~ 2°C/min.).

2.3.2 Crystallization

It has been previously shown that crystallization range in bioactive glass 45S5 exists from ~ 600°C to 750°C [23, 27, 31]. The crystallization heat treatment process for bioactive glass 45S5 samples was carried out for three different temperatures: 640°C, 680°C and 720°C respectively. All the crystallization heat treatment cycles were carried in the same muffle furnace (Thermo Scientific, Model: F48055). Two different heating rates were employed at each crystallization temperature to obtain a series of bioactive glass ceramics with different amounts of crystallinity demonstrating a transition from amorphous to fully crystalline. In the first case, samples were inserted in the muffle furnace at room temperature and the temperature was ramped up at 20°C/min (heating rate) to each temperature: 640°C, 680°C and 720°C respectively. Samples were kept at that temperature for varied durations of time at each of these temperatures in order to manufacture glass ceramics with different degrees of crystallinity and

derive a transition from amorphous to full crystalline structure as a function crystallization time at a particular crystallization temperature. Similar treatments were given in the second case with the change that the bioactive glass samples were inserted when the muffle furnace was already at the required temperatures (i.e. 640°C, 680°C and 720°C respectively). Table 2.2 provides different durations of time that the samples were kept to obtain varied degrees of crystallinity as the bioactive glass samples underwent a transition from amorphous to fully crystalline at three different temperatures (640°C, 680°C and 720°C) each with two different heating rates (ramped up at 20°C/min to that temperature and inserted at that temperature).

Crystallization Temperature (°C)	Heating rate	Crystallization Time (min)						
640	Inserted	0	90	150	210	300	390	480
	Ramped up 20°C/min	0	60	150	210	300	390	450
680	Inserted	0	20	30	45	60	90	105
	Ramped up 20°C/min	0	15	22.5	30	37.5	45	60
720	Inserted	0	4	6	7.5	12	20	25
	Ramped up 20°C/min	0	4	5	7.5	12	20	-

Table 2.2: Bioactive glass 45S5 samples held at various times at the temperature of interest for two different heating rates.

2.3.3 Etching

Bioactive glass 45S5 samples undergo deformations with increased degree of crystallinity, owing to structural changes occurring in them during crystallization. Deformation occurring during crystallization is evident from the macrographs of polished as received and fully crystallized bioactive glass 45S5

samples as shown in Figure 2.4 (A) and 2.4 (B). Hence, these samples were ground and polished again as per the sample preparation procedures mentioned above (recall sections 2.1.2, 2.1.3 and 2.1.4). A macrograph of polished crystallized sample is shown in Figure. 2.4(C). Subsequently these polished crystallized samples were etched with 0.05% HF solution for 4 seconds in Nanofab Laboratory (University of Alberta) so as to make the crystalline areas in the samples more prominent and facilitate better characterization. Moreover, a partially crystallized bioactive glass disc (crystallized at 680ºC for 30 min) was sectioned along its thickness. The cross sectioned surface was ground, polished and annealed by the procedure mentioned above (recall sections 2.1.2, 2.1.3 and 2.1.4), before being etched with 0.05% HF solution for 4s.
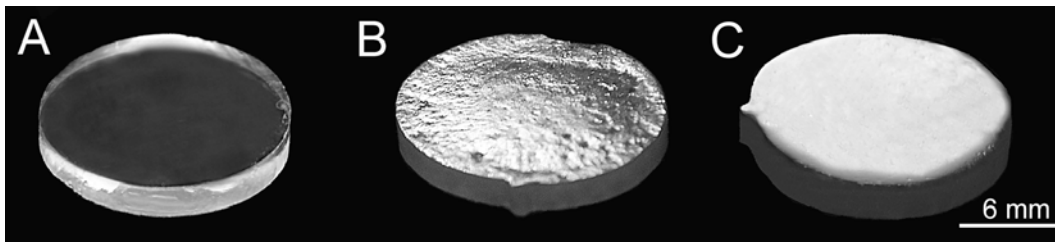
Fig. 2.4: Macrographs of (A) Polished as received, (B) Fully Crystallized, (C) Polished fully crystallized bioactive sample 45S5.

2.4 Characterization

Different methods were utilized to characterize various properties and parameters of amorphous and crystalline bioactive glass 45S5 samples. The methods and equipment used are described in the succeeding sub sections below. All samples were stored in a desiccator in between their characterization study.

2.4.1 Imaging

Macrographs of amorphous and all the partially/fully crystallized bioactive glass 45S5 samples mentioned in Table 2.2 were taken with a Nikon Coolpix L100 digital camera. Moreover, macrographs of partially crystallized sample

cross section after the dye penetrant test and fractured surfaces of amorphous and crystallized sample after thermal shock resistance test were also taken with the aforementioned digital camera. All the optical micrographs were taken in reflected bright field with 20X (N.A. = 0.4) objective on a Nikon Epiphot 300 optical microscope fitted with a Nikon D300 DSLR camera.

2.4.2 X-ray diffraction

X-ray diffraction (XRD) was performed on the as received amorphous bulk sample, bulk samples crystallized at 680°C for 15, 22.5, 30, 37.5, 45 and 60 minutes, and powder samples obtained from crushed bulk samples crystallized at 640°C for 510 minutes and at 720°C for 20 minutes. XRD was performed using a Rigaku Rotating Anode system with CuKα radiation (λ = 1.5406^{o}A) at 40kV and 110 mA. 1° diffraction slit and 0.3° receiving slit scanning between 10º and 110º for 2θ values at the rate of 2º/min.

2.4.3 Image analysis

Optical micrographs obtained for the partially crystallized bioactive glass 45S5 ceramic showed regions of crystalline and amorphous phases. Quantification of the degree of crystallinity was done by crystalline area fraction calculation in these partially crystallized bioactive glass samples using ImageJ software (a public domain Java image processing program). The ImageJ software converts coloured optical micrographs into 8-bit binary images and subsequently calculates the area fraction of crystalline phases. Three optical images obtained from an etched sample surface were chosen to tabulate values of crystalline area fraction (at various crystallization times). Similar exercises were performed for each crystallization time considered (mentioned in Table 2.1) at the three different temperatures (640°C, 680°C and 720°C) and their corresponding heating rates (ramped up at 20°C/min to that temperature and inserted at that temperature).

Grain size measurements were conducted by using the linear intercept method by Fullman compensation formula [73] which provides the average grain size.

$$GS = \frac{3\sum L_i}{2\sum N_i} \qquad (2.1)$$

where *GS* is the average grain size, *L* is the length of the lines drawn on optical micrographs and *N* is the number of intercepts each line makes at the grain boundaries. Number of lines chosen were such that $N_i \geq 100$. This method was conducted for six micrographs of fully crystallized samples each obtained at three crystallization temperatures and both heating rates.

2.4.4 Scanning electron microscopy

For scanning electron microscopy (SEM) the bioactive glass ceramic samples were at first gold sputter coated (Xenosput XE200) for 5 minutes to prevent any charging during imaging. All the back scattered electron and secondary electron micrographs of amorphous and crystallized bioactive glass 45S5 samples were taken using a Zeiss EVO Scanning electron microscope with a LaB_6 filament.

2.4.5 Fourier transform infrared spectroscopy

Fourier Transform Infrared Spectroscopy (FTIR) was performed by diffused reflectance technique using a Nicolet Magna 760 FTIR main bench with a Spectra-Tech diffuse reflectance attachment. The sample and background spectra were obtained in absorbance mode using 64 scans at 4 wavenumber resolution. The background was obtained using a clean silver mirror. An absorbance spectra was obtained using this technique. In case of FTIR, an infrared beam is projected on the sample. The amount transmitted (T) through, amount reflected (R) from and the amount absorbed (A) in the sample gives the total intensity (I) of the infrared beam. Hence,

$$I = T + R + A \qquad (2.2)$$

In this case, the sample was a bulk sample, hence the amount transmitted through the sample was 0 (i.e. T=0). If the total infrared beam intensity is considered to be 1 (i.e. I =1), then

$$1\text{-}A = R \qquad\qquad (2.3)$$

Hence a reflectance pattern was obtained by subtracting the absorbance spectra from 1 in the Y axis for further analysis and comparison with literature.

2.4.6 Microindentation

Microindentations were made on polished amorphous, etched partially crystallized (crystallized at 680ºC for 22.5 min and 30 min), and unetched fully crystalline sample (crystallized at 680ºC for 60 min) bioactive glass samples using a diamond Vickers indenter (Mitutoyo MVK-H1). An array of 5 indents spaced at least 3 indent diagonal lengths away from each other, were made at a load of 300gf corresponding to a force of 2.943N on each sample surface and optical micrographs of the indents with their crack paths were recorded.

2.4.7 Dye penetrant test

A partially crystallized bioactive glass 45S5 sample was sectioned along the cross section and subsequently polished. A macrograph of the cross sectional surface was recorded for future comparison with end results using the equipment mentioned above (recall Section 2.4.1). The dye/ink obtained from a Sharpie® permanent marker was spread over the polished cross sectional surface of the sample. Following that, the sample was placed on a vacuum plate (Nalgene^{TM}) and covered by an inverted vacuum jar (Nalgene^{TM}). A gasket sealed the gap between the lip of the jar and the vacuum plate. The whole system inside the jar was brought to a vacuum by using a mechanical pump (Fisher Technical Company, LAV-3). Vacuum was maintained for about 10 minutes following which the sample was taken out and the dye/ink on the cross sectional surface was wiped clean with a Kimwipe. Macrographs and optical micrographs were taken by the same equipment mentioned above (recall Section 2.4.1) for recording the Dye Penetrant Test (DPT) results.

2.4.8 Thermal shock resistance test

An amorphous sample of bioactive glass 45S5 was taken in an alumina crucible and was inserted in the muffle furnace (Thermo Scientific, Model: F48055) and the temperature was ramped up at 20°C/min until it reached 680°C. As soon as the desired temperature was reached, the crucible with the sample was taken out from the furnace with tongs and the sample was quenched in water. A similar exercise was conducted for another amorphous sample and in this case, the sample instead of being taken out exactly when 680°C was reached, it was allowed to sit in the furnace for 30 min at 680°C. Subsequently after 30 minutes, the crucible containing the partially crystallized sample was taken out of the furnace and was quenched in water. Macrographs of both the samples were taken using the same camera as mentioned in section 2.4.1 and secondary electron images of the fractured surfaces were taken using the same SEM as mentioned in section 2.4.4.

2.5 *In vitro* immersion in phosphate buffer solution

2.5.1 Phosphate buffer solution (PBS): recipe

In vitro immersion testing of partially crystallized bioglass 45S samples was carried out in PBS according to [28]. The main ingredients for preparation of 1 litre of PBS are:

1. Stock Solution
2. Magnesium Chloride ($MgCl_2$) Solution
3. 1N Sodium Hydroxide (NaOH) Solution
4. De-ionized ultra filtered water (DIUF)

Preparation of 100ml of stock solution:

The stock solution was prepared in an iso-temperature water bath (Fisher Scientific Isotemp 210, Model No. 15-462-10) at 36.5°C. 3.4g of Potassium dihydrogen phosphate (KH_2PO_4) weighed in a balance (Denver Instrument, Model No. P-214) and was added to 50ml of DIUF. Thereby, the pH of the

solution was adjusted to 7.2 by adding 1N NaOH drop by drop. The pH of the solution was determined by dipping the electrode of an Accumet Basic AB15 Plus pH meter (Fisher Scientific) in the stock solution. The Automatic Temperature compensation (ATC) probe connected to the pH meter was dipped in the water bath to confirm that the pH reading was taken by the equipment at a temperature of 36.5°C instead at room temperature. After adjusting the pH of the solution, the volume was brought to 100ml by adding DIUF. The pH meter was calibrated before using it and its accuracy was checked by dipping its electrode in standard buffer solutions with known pH (pH=2, 4, 6, 8). Variation in pH was on the order of $\pm$ 0.05.

Preparation of 100ml of magnesium chloride ($MgCl_2$) solution:

3.8g of $MgCl_2$ powder (reagent grade) was weighed in the same balance mentioned above and added to 100ml of DIUF. The solution was stirred till the $MgCl_2$ powder was totally dissolved in the solution.

Preparation of 100ml of 1N sodium hydroxide (NaOH) solution:

4g of NaOH powder (reagent grade) was weigh in the same balance mentioned above and added to 100ml of DIUF to obtain 1N NaOH solution.

Preparation of final working solution of PBS (1 Litre):
1. 1.25ml of stock solution was poured into a 1 litre beaker.
2. 5ml of magnesium chloride solution was added to the solution.
3. The volume of the solution was brought to 1 litre by adding DIUF to obtain to a working solution of PBS. The target pH of the solution was 7.2 $\pm$ 0.2.

All the solutions including PBS were stored under refrigeration between 4-7°C.

2.5.2 *In vitro* immersion test

Kokubo *et al.* formulated the procedure of the apatite test in the case of simulated body fluid (SBF) [37]. For calculation of the volume of immersion medium needed for *in vitro* testing the following formula was used

$$V_S = S_A/10 \qquad\qquad (2.4)$$

where V_S is the volume of immersion medium required in mL and S_A is the apparent surface area of the specimen in mm^2.

This procedure was also used for *in vitro* immersion in PBS. The diameters and thicknesses of 3 etched bioactive glass 45S5 samples partially crystallized at 680ºC for 30 minutes were measured using a digital calliper. The diameters were 10.61, 10.63 and 10.66 mm respectively and the corresponding thicknesses (or heights, considering them as cylinders) of the samples were 2.66, 2.65, and 2.64 mm respectively.

Average diameter of samples $\overline{d}$ = 10.63mm

Average radius of samples $\overline{r}$ = 5.315mm

Average height of samples $\overline{h}$ = 2.65mm

Apparent Surface Area (S_A) = $2\pi\overline{r}\overline{h} + 2\pi\overline{r}^2$ = 265.86 mm^2

Therefore, $V_S = S_A/10 = 265.86/10 = 26.5$ mL

Hence, the volume of PBS required for immersion testing was found to be 26.5mL. Subsequently, the same 3 etched bioactive glass 45S5 samples partially crystallized at 680ºC for 30 minutes whose dimensions were determined, were placed in three separate petri dishes. Each of the three samples was immersed in 26.5 mL of PBS poured on to the respective petri dishes. The petri dishes were covered with a polymer cover and sealed with cello tape to prevent contamination and evaporation. Each of the 3 separate petri dishes containing the samples immersed in PBS were placed inside an iso-temperature water bath (Fisher Scientific Isotemp 210, Model No. 15-462-10) maintained at 36.5ºC for time periods of 1, 6 and 12 days. The temperature was maintained at 36.5ºC in order to mimic the temperature of the human body so as to facilitate reactions occurring at that temperature. In order to ensure that all ions present in PBS were available at all times to stimulate surface reactions with the bioactive glass samples; the PBS was replaced with fresh PBS every 3 days.

CHAPTER 3

Crystallization kinetics*

3.1 Introduction

Various studies were conducted to study the effects of thermal treatments in changing the structure and development of new phases after the glass transition temperature of 550°C in bioactive glass 45S5 leading to crystallization [23, 27, 31, 34, 57]. Bretcanu *et al.* found that the bioglass 45S5 crystallizes in the range between 600°C and 750°C [31] while an earlier study by Lefebvre *et al.* [27] showed structural changes and alterations occurring in bioactive glass 45S5 just after its glass transition temperature of 550°C. In an effort to study the crystallization kinetics of bioactive glass 45S5, a crystallization temperature range of 640°C – 720°C was chosen.

3.1.1 Amorphous bioactive glass 45S5

A macrograph of an as received amorphous bioactive glass 45S5 disc is shown in Figure 3.1A which indicates a completely transparent sample. Moreover, an optical micrograph of an etched amorphous sample (Figure 3.1B) produces a rough surface due to etching of impurities or discontinuities on the surface.

3.2 Crystallization at 640°C

Crystallization of the bioactive glass 45S5 disc samples were initially conducted by placing the sample in the furnace at room temperature and ramping up the temperature at 20°C/min to 640°C. The samples were kept at that temperature for different durations of time as per Table 2.1.
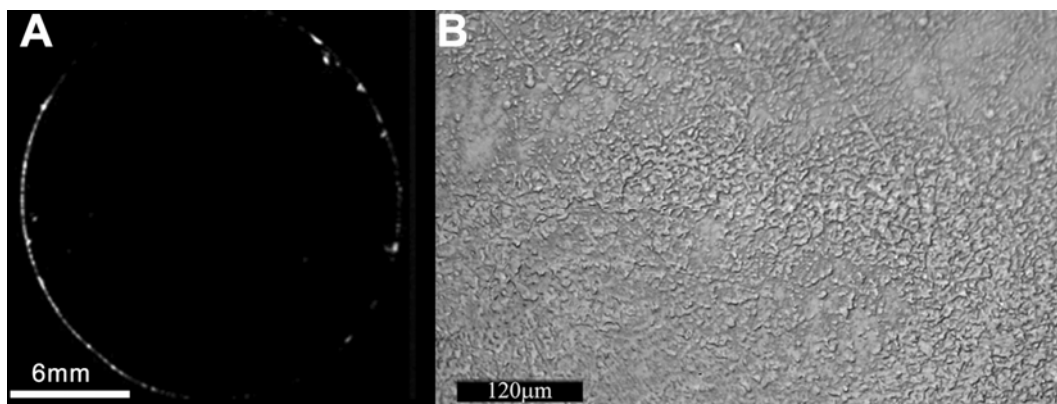
Fig. 3.1: As received amorphous bioactive glass 45S5 (A) Macrograph of a disc (B) Optical micrograph after being etched with 0.05% HF for 5s.

3.2.1 Macrographs

Figure 3.2 – 3.4 show the macrographs of bioactive glass samples crystallized at three temperatures for various durations of time. A change in optical transparency was observed as a function of crystallinity; amorphous samples were transparent, and crystallized samples were translucent.

The macrographs indicate 'devitrification' or crystallization occurring in the samples as the degree of transparency gradually decreases with increasing crystallization time. The change in optical properties can be attributed to light scattering due to the formation of crystals with different index of refraction 'i' (for bioactive glass 45S5 $i = 1.55$ while for combeite crystals $i = 1.598$). Moreover, along with the gradual increase in translucency, some isolated "flowery patterns" spread throughout the samples were also observed which contributed to an exaggerated optical translucency due to light scattering in partially and fully crystallized samples.

3.2.2 Optical micrographs

Figure 3.5 shows optical micrographs depicting the transition of bioactive glass 45S5 disc samples from the amorphous to crystalline state as they are crystallized at a temperature of 640°C over a time span of 60 to 450 minutes. As

the crystallization time increased crystals nucleated and grew in random locations, as is evident from the optical micrographs. The crystallites continued to grow in size individually until they started impinging on one another thus forming regions of crystalline phase with small islands of amorphous phase entrapped. For samples with higher amounts of crystallinity, the crystallites are not spherical (as seen in samples with lower amounts of crystallinity) because during growth whenever one spherical crystallite coalesces with any other crystallite their growth in the abuttal region is restricted thus producing polyhedral crystallites instead of being spherical. After a crystallization time of 450 min, a fully crystallized bioactive glass 45S5 sample (Figure 3.5F) with polyhedral crystallite grains was obtained.

3.3 Variation in crystallization temperature

In an effort to know the effect of temperature on the crystallization of bioactive glass 45S5, similar crystallization experiments were conducted on bioactive glass 45S5 samples at 680°C and 720°C. The samples were placed in the furnace at room temperature and the temperature was ramped at 20°C/min to reach crystallization temperatures of 680°C and 720°C respectively; thereby the samples were kept at these temperatures for various durations of time to obtain data of gradual transformation of an amorphous sample in to a fully crystallized one at these two additional temperatures.

3.3.1 Crystallization at 680°C

Macrographs and optical micrographs of bioactive glass 45S5 samples crystallized at 680°C for different crystallization times are shown in Figure 3.3 and Figure 3.6 respectively. Transition from amorphous to crystalline phases was observed (similar to crystallization carried out at 640°C) in Figure 3.3 which indicated 'devitrification' occurring in these samples. Moreover, as evident from the optical micrographs in Figure 3.6, growth of crystals continued with increasing crystallization times until they impinged on one another.

It was observed that increasing the temperature by 40°C (from 640°C to 680°C) resulted in the bioactive glass samples taking exponentially smaller durations of time to crystallize. However, no visible change in the crystallite size in a fully crystallized sample obtained at either temperature was noticed.

3.3.2 Crystallization at 720°C

Macrographs and optical micrographs of bioactive glass 45S5 samples crystallized at 720°C at different crystallization times are shown in Figure 3.4 and Figure 3.7 respectively. Changes in optical properties - transparent (amorphous) to translucent (crystalline) similar to that seen during crystallization at 640°C and 680°C were noticed in Figure 3.4 which indicated 'devitrification' occurring in these samples and the growth of crystals with increasing crystallization times until they impinge on one another were evident from the optical micrographs in Figure 3.7. It was observed that increasing the temperature by 80°C (from 640°C to 720°C) resulted in the bioactive glass samples taking exponentially less duration of time to crystallize. Therefore, it can be said that an increase in crystallization temperature increases the rate of crystallization (i.e. for the temperatures of interest the phase transformation rate was exponentially dependant on temperature).

However, the crystallite size in a fully crystallized sample at 720°C (crystallization time 20 minutes) was visibly the same as that obtained in fully crystallized samples at 640°C (crystallization time 450 minutes) and 680°C (crystallization time 60 minutes). This is shown in Figures 3.8 which indicates the size of the crystallites obtained to be in the range ~ 20-30μm.

Growth of crystallites during ramping up to 720°C

The thermal treatment given in this technique required that the sample sits inside the furnace as it gets heated up to the crystallization temperature from room temperature at a ramping rate of 20°C/min. This means that the sample spends considerable amount of time in the crystallization range of 600 to 720°C (since

720°C is the crystallization temperature in this case) during ramping up the furnace temperature.

It must be noted that the crystallization time was taken into account only when the furnace temperature reached the crystallization temperature (720°C in this case) i.e. the dwell time of the samples at the desired crystallization temperature (refer schematic Figure 3.13). Hence, presence of crystallites was observed even at 0 minute crystallization time for 720°C due to nucleation and growth of crystals *during ramping up* the furnace temperature. Moreover, higher rate of crystallization at a temperature of 720°C also added to the nucleation and growth stage occurring during ramping up the furnace temperature. Thus, higher residence time in the crystallization range during ramping up the furnace temperature and higher rate of crystallization contributed to the formation of crystallites by the time the furnace reached 720°C. A time lag before commencing the growth of crystallites would have caused the crystallized fraction to not increase until some time had elapsed at the crystallization temperature.

Micrographs at 0 minute corresponding to temperatures of 640°C and 680°C were not shown because no crystallites were found at 0 minutes in these temperatures as the samples did not spend much time during ramping up of furnace temperature to these temperatures and also due to lower rate of crystallization at these lower temperatures. The samples obtained at 0 minute for 640°C and 680°C were similar to that obtained for an as received etched amorphous sample (recall Figure 3.1).

Crystallization Temperature 640°C
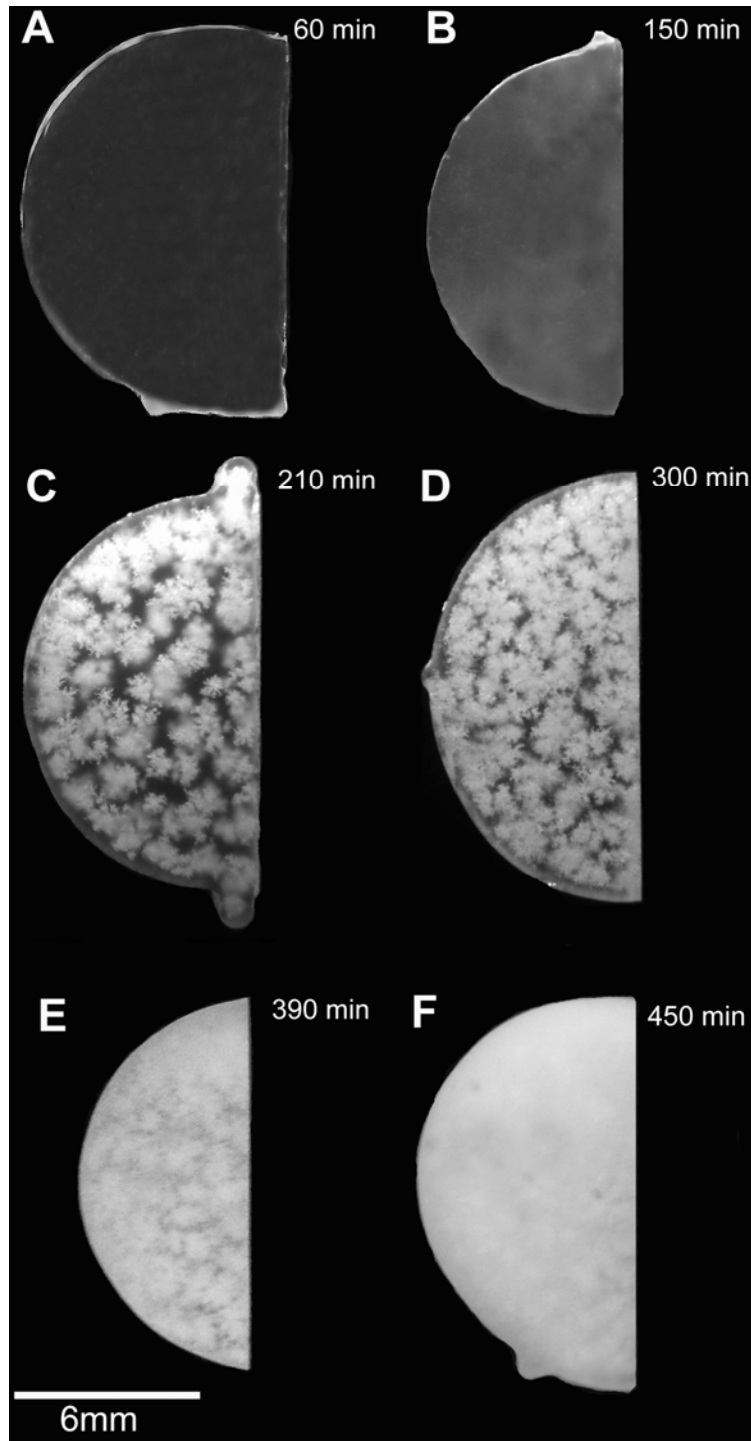
Fig. 3.2: Macrographs of bioactive glass 45S5 samples crystallized at 640°C for dwell times of (A) 60 min (B) 150 min (C) 210 min (D) 300 min (E) 390 min (F) 450 min.

Crystallization Temperature 680°C
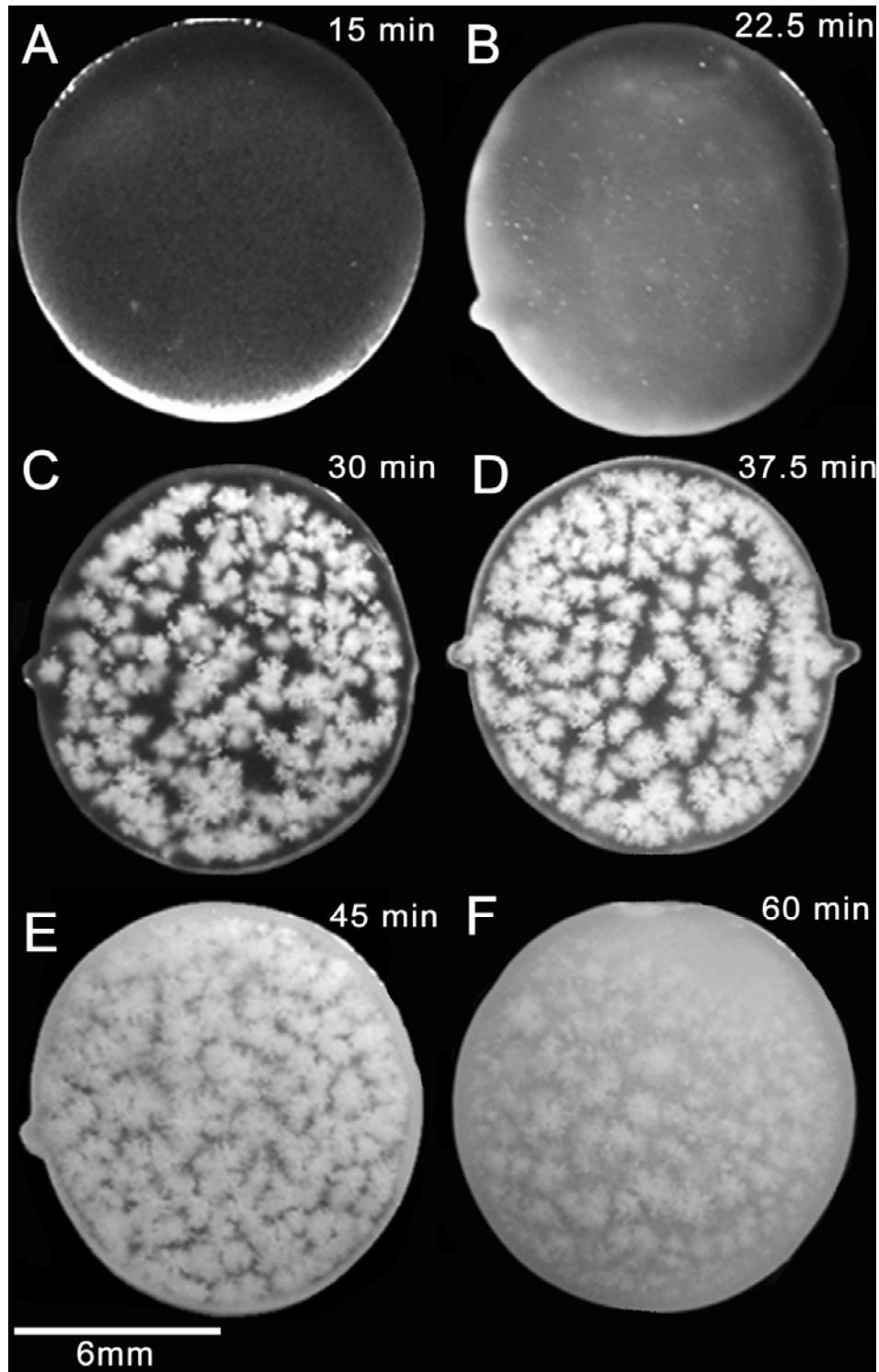
Fig. 3.3: Macrographs of bioactive glass 45S5 samples crystallized at 680°C for dwell times of (A) 15 min (B) 22.5 min (C) 30 min (D) 37.5 min (E) 45 min (F) 60 min.

Crystallization Temperature 720°C
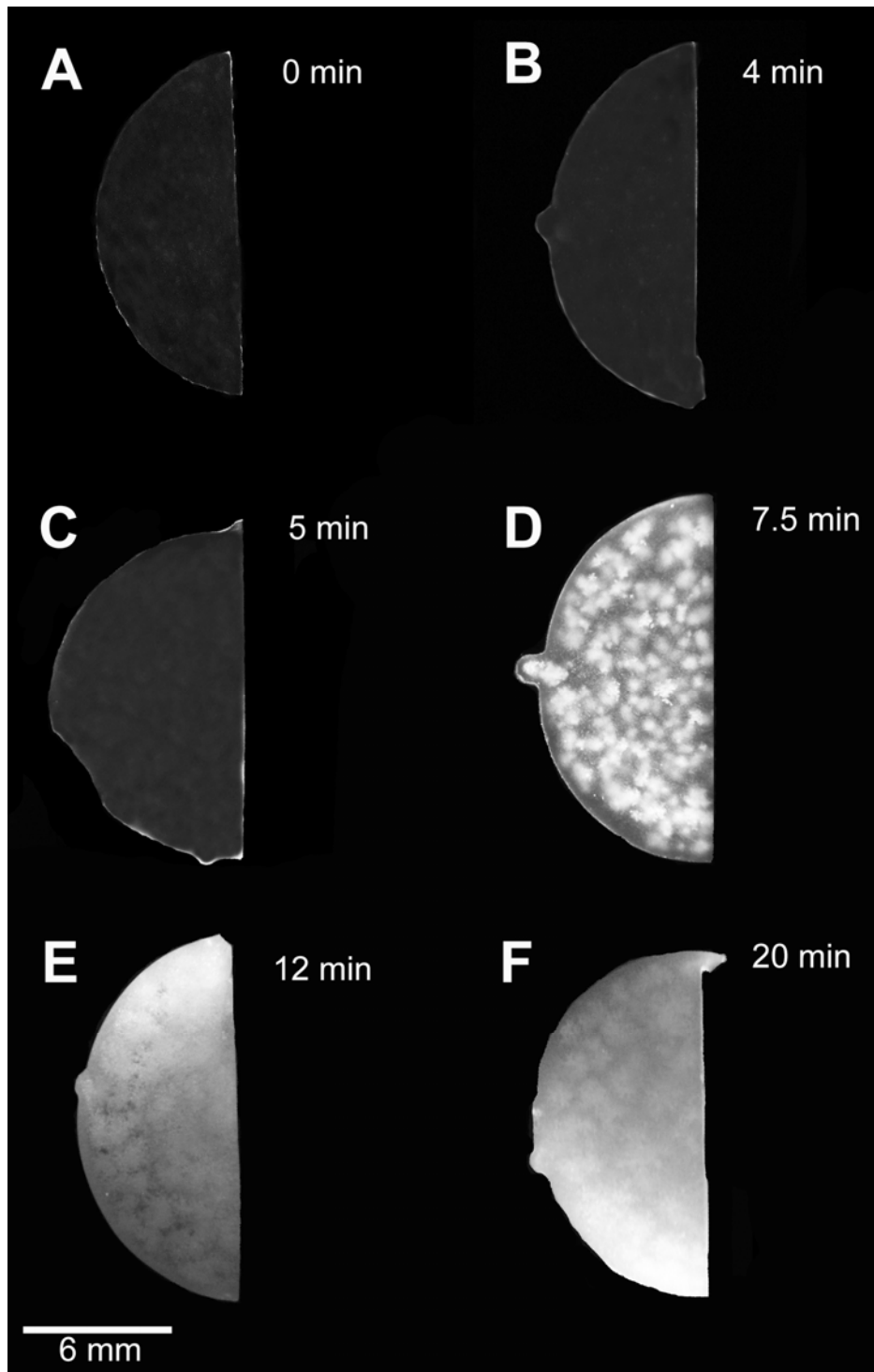
Fig. 3.4: Macrographs of bioactive glass 45S5 samples crystallized at 720°C for dwell times of (A) 0 min (B) 4 min (C) 5 min (D) 7.5 min (E) 12 min (F) 20 min.

Crystallization Temperature 640°C
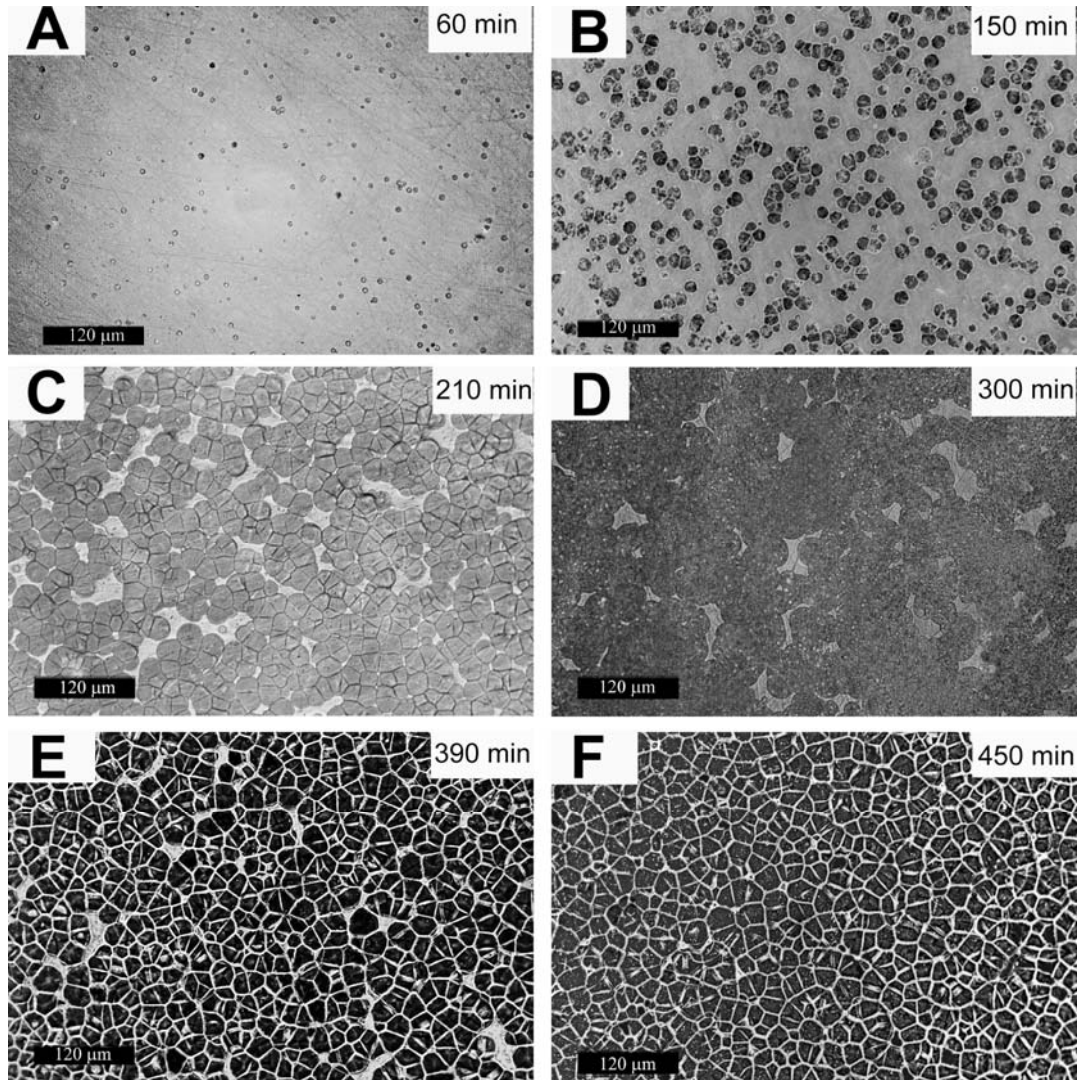
Fig. 3.5: Optical micrographs of bioactive glass 45S5 samples crystallized at 640°C and etched with 0.05% HF for 5s for dwell times of (A) 60 min (B) 150 min (C) 210 min (D) 300 min (E) 390 min (F) 450 min.

Crystallization Temperature 680°C
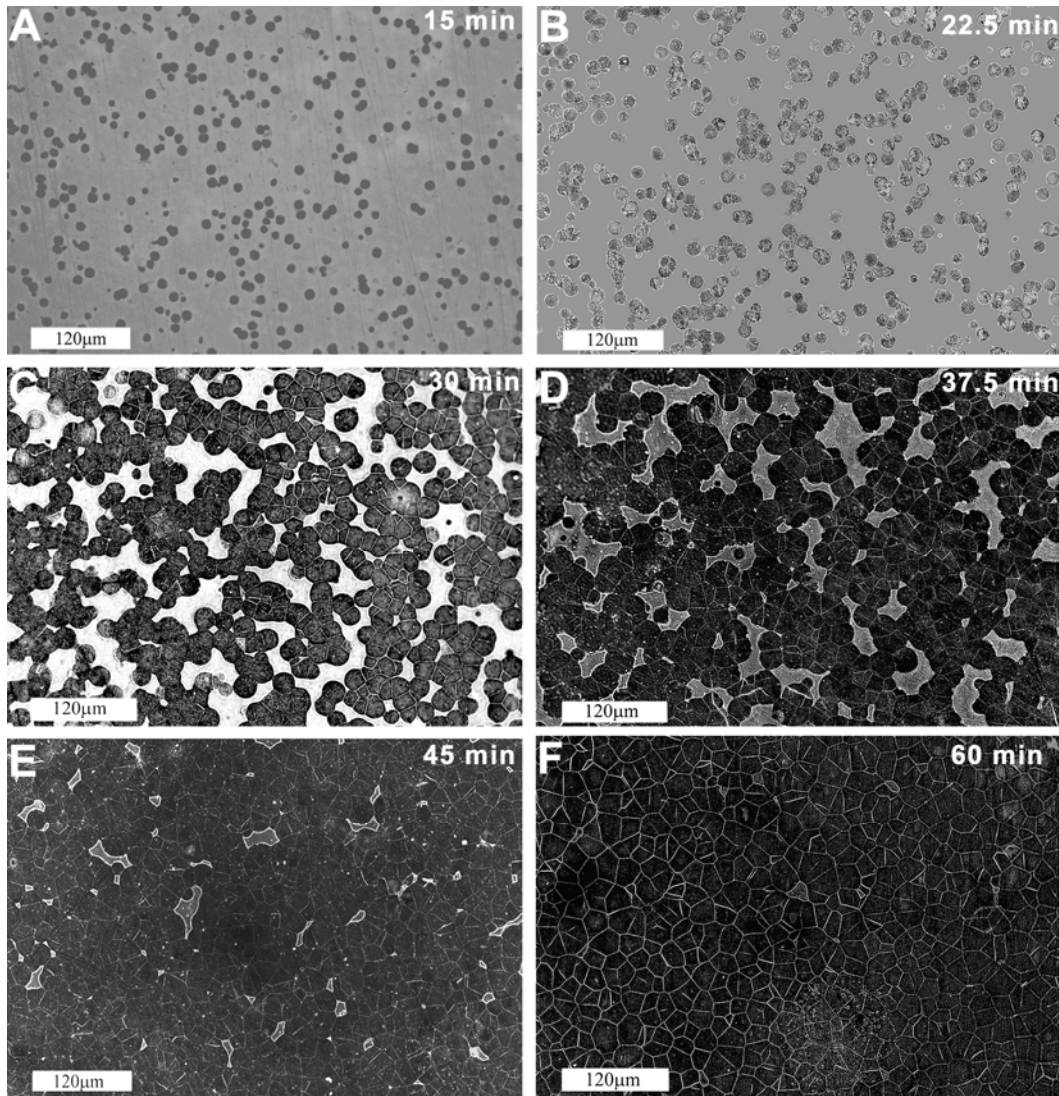
Fig. 3.6: Optical micrographs of bioactive glass 45S5 samples crystallized at 680°C and etched with 0.05% HF for 4s for dwell times of (A) 15 min (B) 22.5 min (C) 30 min (D) 37.5 min (E) 45 min (F) 60 min.

Crystallization Temperature 720°C
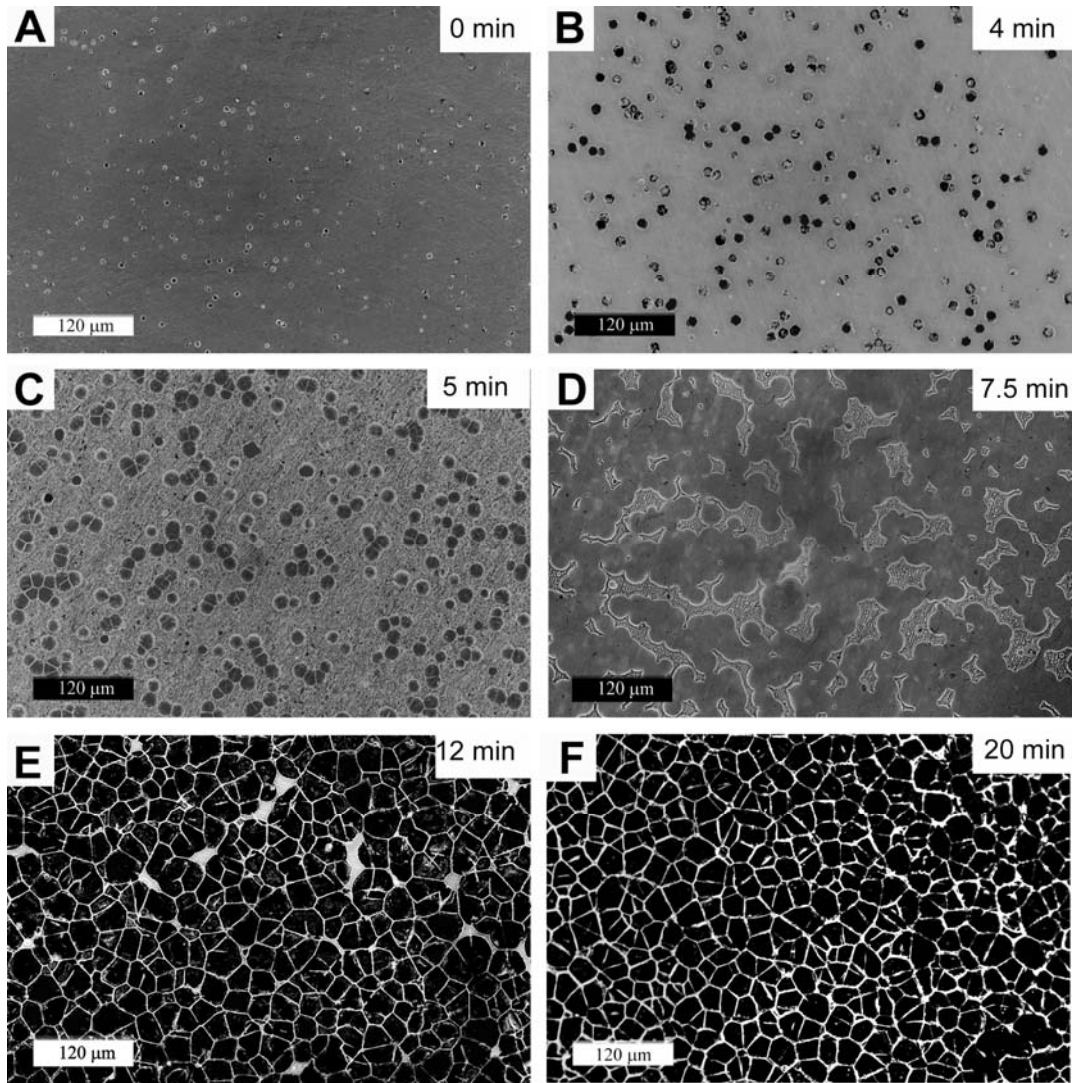
Fig. 3.7: Optical micrographs of bioactive glass 45S5 samples crystallized at 720°C and etched with 0.05% HF for 5s for dwell times of (A) 0 min (B) 4 min (C) 5 min (D) 7.5 min (E) 12 min (F) 20 min.
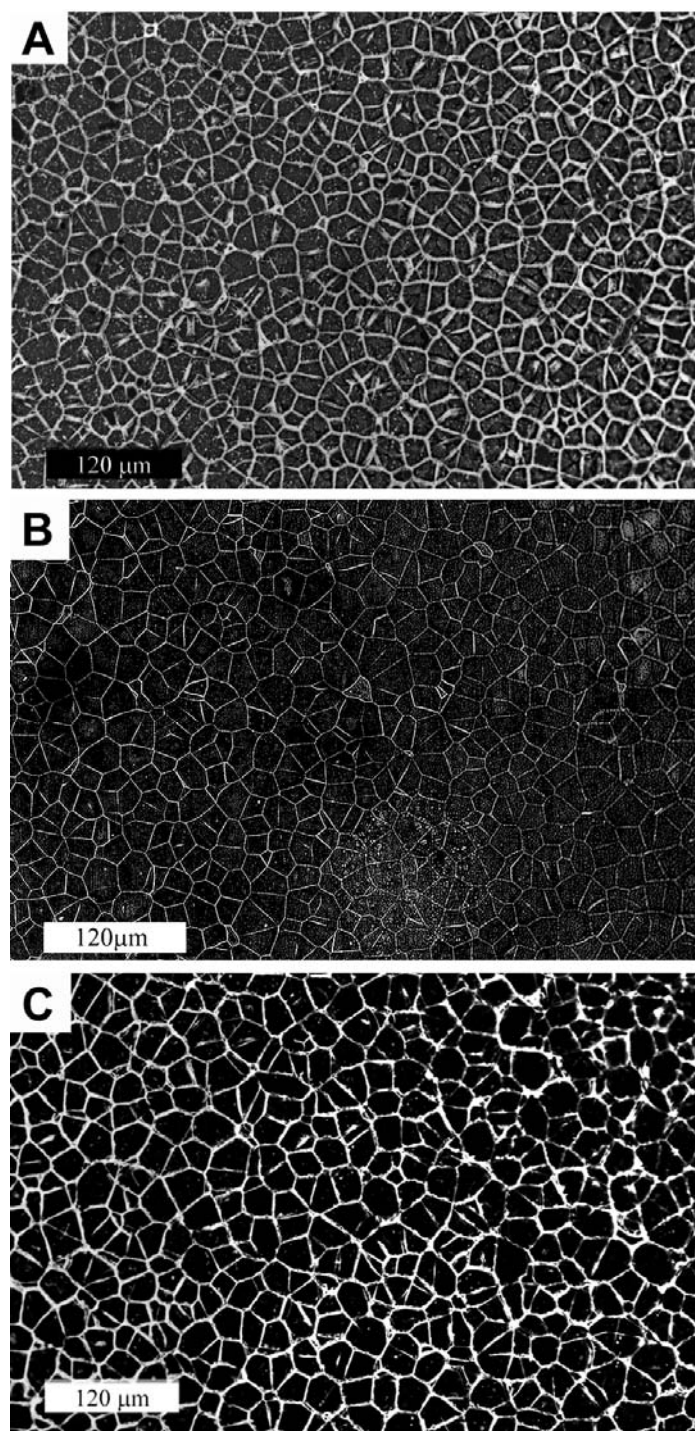
Fig. 3.8: Comparison of optical micrographs obtained from fully crystallized samples (A) crystallized at 640°C for 450 min (B) crystallized at 680°C for 60 min (C) crystallized at 720°C for 20 min.

3.4 Characterization of crystalline phase by x - ray diffraction

The gradual development of crystalline phase as a result of thermal treatment at a crystallization temperature of 680°C was confirmed using XRD. The XRD plots in Figure 3.9 indicate the evolution of a fully crystalline bioactive glass 45S5 after being crystallized for 60 min from an amorphous as received sample. XRD data revealed that the only crystalline phase formed in bioactive glass 45S5 was Combeite ($Na_2Ca_2Si_3O_9$; ICDD PDF Card #075-1687).

The XRD plot for the amorphous as received sample shows some feeble peaks at approximately $2\theta \sim 30°$, which might indicate the presence of some crystalline phase. However, the XRD plots at 15 minutes and 22.5 minutes indicate that there are no peaks at $2\theta \sim 30°$ and only at even higher crystallization times a new peak developed at $2\theta \sim 29.5°$ due to combeite. If that feeble peak in the as received sample was due to pre existing nuclei, then it should also be present and have become more prominent in the 15 min and 22.5 min XRD plots. Moreover, the peak at $2\theta \sim 34°$ shows the highest intensity for the crystalline phase formed but it is totally absent in the amorphous sample. If there were any pre existing nuclei in the material then this peak would have certainly showed up in the as received sample XRD plot. Therefore, the feeble crystallization might be due to some impurity or dirt on the sample which might provide a nucleation site for crystallization but is not due to pre existing nuclei of combeite. Hence the crystallization kinetics calculation carried out later was considered to be unaffected by this impurity.

As revealed by XRD, the crystalline phase formed in bioactive glass 45S5 when crystallized at 680ºC was combeite, which contains no phosphorus. However, bioactive glass 45S5 contains 6 wt% P_2O_5. This meant that a fully crystallized sample would not be fully crystalline in the true sense, as it might have a phosphorus rich phase present. Hence, a crystallized sample was referred as fully crystallized when crystallites were found all over on its surface. The area

fractions of crystallites found on the sample surface were considered for determining the amounts of crystallinity in this case. However, it might be a possibility that the amorphous phosphorus rich phase was distributed in the grain boundaries and the amorphous regions in a partially crystallized sample while it might be present at grain boundaries in a fully crystalline 45S5 sample.
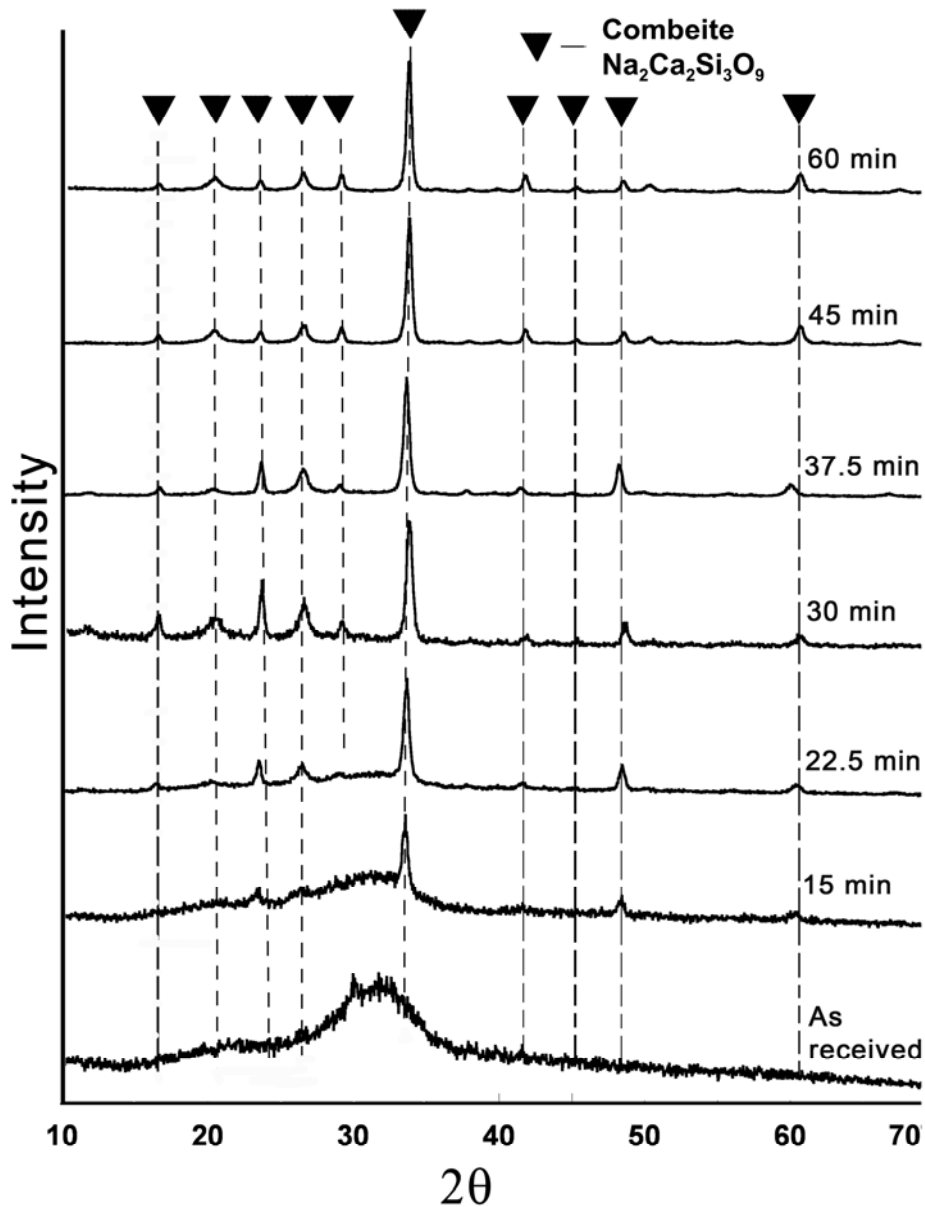
Fig. 3.9: Thin film XRD patterns of bulk bioactive glass 45S5 crystallized at 680°C for different crystallization time intervals. Combeite ($Na_2Ca_2Si_3O_9$) was the only crystalline phase formed. Only high intensity peaks have been labeled.

Fully crystallized bulk samples obtained at 640°C (crystallization time 450 min) and at 720°C (crystallization time 20 minutes) were crushed into powder and XRD was performed on these powder samples in order to confirm that the crystalline phase formed was combeite. The powder XRD patterns for fully crystallized samples obtained at 640°C and at 720°C are shown in Figure 3.10 which also showed that the main crystalline phase formed was Combeite ($Na_2Ca_2Si_3O_9$; ICDD PDF Card #075-1687).
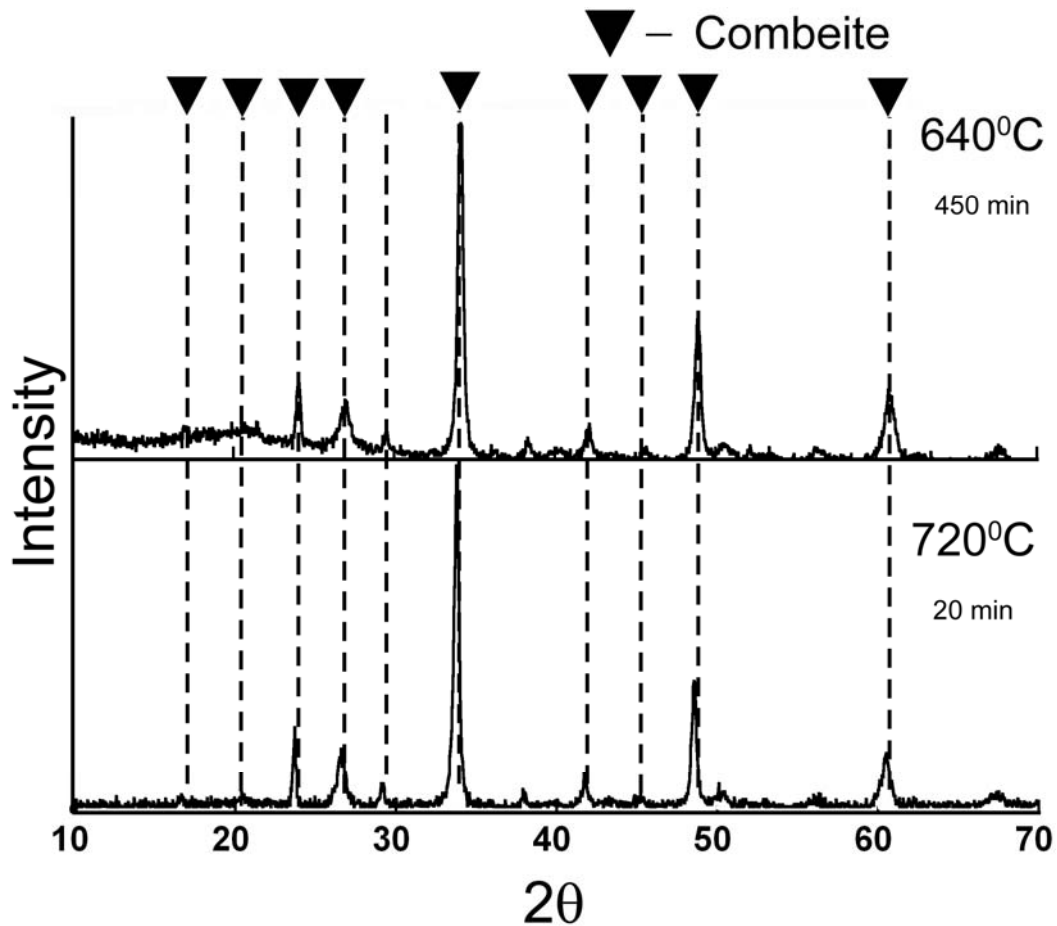
Fig. 3.10: XRD patterns of fully crystalline powdered bioactive glass 45S5 samples (bulk samples crushed to powder) crystallized at 640°C for 450 min. and 720°C for 20 min. respectively. Combeite ($Na_2Ca_2Si_3O_9$) was the only crystalline phase formed. Only high intensity peaks have been labeled.

3.5 Kinetics of crystallization and effect of temperature

Different techniques have been to determine the crystalline kinetics of various bioactive glasses such as using differential thermal analysis / differential scanning calorimetry (DTA/DSC) [27, 34, 59] or calculation of crystalline area fraction from optical micrographs [23, 58] by point counting stereology methods. In this study, volume fractions of crystalline phase formed at 640°C, 680°C and 720°C in etched bioactive glass 45S5 at different crystallization times were required to be determined in order to formulate the Avrami crystallization kinetics. Thereby, quantitative microstructural evaluations from optical micrographs were needed.

3.5.1 Image analysis

The first step towards this evaluation was to calculate the area fraction of crystalline phases formed at each crystallization times. This was done by using ImageJ software. ImageJ converts coloured optical micrographs into binary images first, so as to separate the amorphous from crystalline areas. Thereafter, it calculates the area fraction of the crystalline phase present in the optical micrograph. Figure 3.11 shows an example of conversion of an optical micrograph obtained from a sample crystallized at 680°C for 30 minutes, into a binary image by ImageJ software. If ImageJ could not properly form a binary image from the coloured optical micrograph, Adobe® Photoshop® was used to colour crystalline phase in order to differentiate it from the amorphous regions. Thereby, binary image was formed from this formatted micrograph using ImageJ.
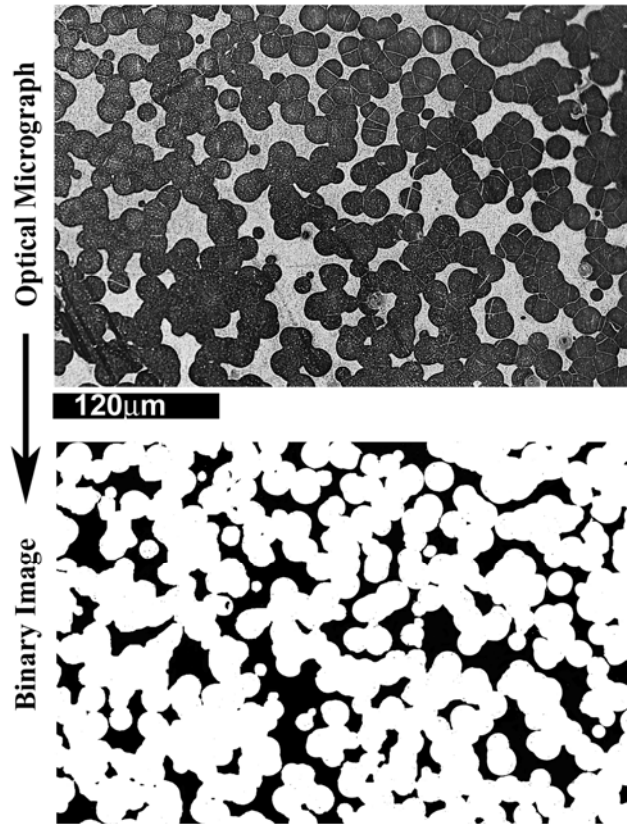
Fig. 3.11: Conversion of optical micrograph (partially crystallized at 680ºC for 30 min) to 8-bit binary image before using ImageJ for crystalline area fraction calculation

3.5.2 Crystalline volume fraction determination

In this study, the area fraction of crystalline phase obtained from optical micrographs using ImageJ software was assumed to be equivalent to the volume fraction present in the sample. Three different micrographs from different locations on each sample surface were evaluated by ImageJ to determine the area fraction of the crystalline phase.

The area fractions of crystalline phases formed at different times at 640°C, 680°C and 720°C are provided in Tables 3.1, 3.2 and 3.3 respectively.

Crystallization time (min)	Crystalline Area Fraction				Min.	Max.
	I	II	III	Average		
0.0	0.000	0.000	0.000	0.000	0.000	0.000
60.0	0.021	0.016	0.020	0.019	0.002	0.003
150.0	0.372	0.421	0.447	0.413	0.034	0.041
210.0	0.777	0.810	0.808	0.798	0.012	0.021
300.0	0.934	0.944	0.950	0.943	0.007	0.009
390.0	0.981	0.979	0.985	0.982	0.003	0.003
450.0	1.000	1.000	1.000	1.000	0.000	0.000

Table 3.1: Crystalline area fractions calculated from three different optical micrographs for different crystallization times at 640ºC.

Crystallization time (min)	Crystalline Area Fraction				Min.	Max.
	I	II	III	Average		
0.0	0.000	0.000	0.000	0.000	0.000	0.000
15.0	0.123	0.158	0.089	0.123	0.001	0.034
22.5	0.400	0.343	0.295	0.346	0.054	0.003
30.0	0.710	0.665	0.686	0.687	0.023	0.022
37.5	0.829	0.793	0.862	0.828	0.001	0.035
45.0	0.974	0.970	0.969	0.971	0.003	0.001
60.0	1.000	1.000	1.000	1.000	0.000	0.000

Table 3.2: Crystalline area fractions calculated from three different optical micrographs for different crystallization times at 680ºC.

Crystallization time (min)	Crystalline Area Fraction				Min.	Max.
	I	II	III	Average		
0.0	0.029	0.027	0.022	0.026	0.003	0.004
4.0	0.115	0.097	0.111	0.108	0.007	0.011
5.0	0.221	0.268	0.236	0.242	0.026	0.021
7.5	0.774	0.811	0.858	0.814	0.044	0.040
12.0	0.976	0.972	0.977	0.975	0.002	0.003
20.0	1.000	1.000	1.000	1.000	0.000	0.000

Table 3.3: Crystalline area fractions calculated from three different optical micrographs for different crystallization times at 720ºC.

3.5.3 Avrami kinetics of crystallization

As discussed earlier, Michael Avrami developed the theory of phase change kinetics in the early 1940s [64-66] known as the Avrami Equation, which describes the phenomenon of a phase transforming into another as function of time at constant temperature. Diffusional phase transformation kinetics including crystallization kinetics is most often studied using the Avrami equation given as:

$$f = 1 - \exp\left(-kt^n\right) \qquad (3.1)$$

where f is the crystalline volume fraction transformed isothermally after time t, k is the rate constant and n is the Avrami exponent.

In order to determine the rate constant 'k' and Avrami exponent 'n' in Equation 3.1, the crystalline fraction transformed 'f' *versus* the crystallization time 't' at each crystallization temperature was plotted and curve-fit generated is shown in Figure 3.12 so as to provide the Avrami crystallization kinetics equation

at each temperature. The values of '*k*' and '*n*' at each crystallization temperature obtained from the plots are provided in Table 3.4.
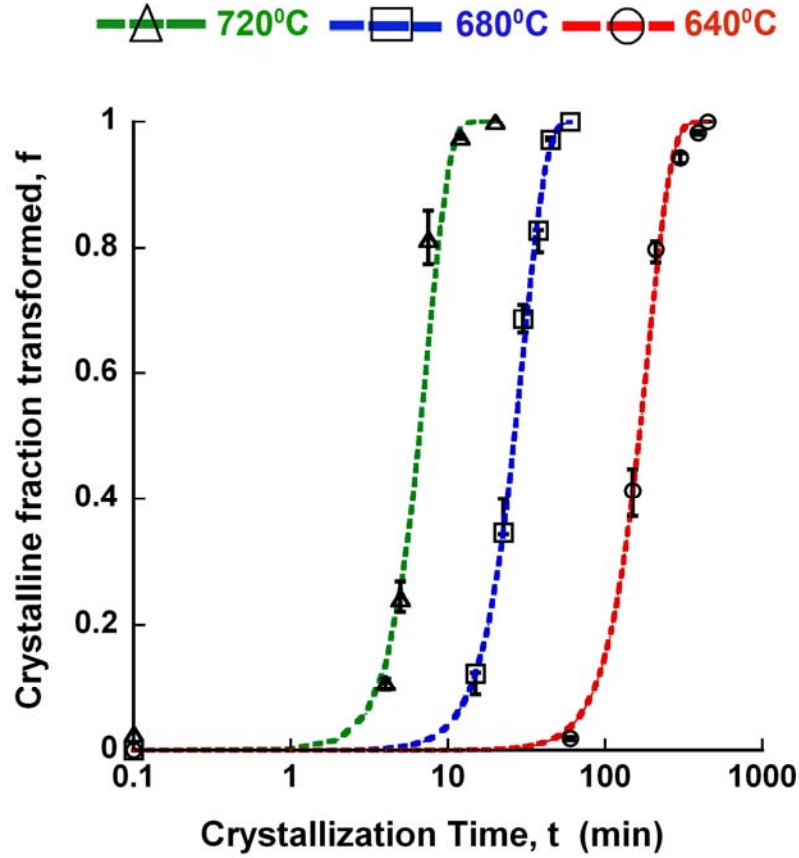
Fig 3.12: Crystallization fraction transformed *vs.* crystallization time (log scale) at 640°C, 680°C and 720°C.

Crystallization temperature (°C)	Rate constant (*k*)	Avrami exponent (*n*)
640	3.0×10^{-7}	2.9
680	5.1×10^{-5}	2.9
720	2.0×10^{-3}	3.1

Table 3.4: Rate constant and Avrami exponent for various crystallization temperatures.

The value of Avrami exponent 'n' ~ 3 at all the three crystallization temperatures indicate bulk crystallization comprising three dimensional growth of crystals which were uniformly nucleated. This result is supported by the optical micrographs of Figures 3.5, 3.6 and 3.7; wherein the number of nuclei clearly does not appear to change, but the size of the nuclei increases with increasing crystallization time. Moreover, the collective plot of crystallized fraction *versus* crystallization time at three different temperatures (Figures 3.12) indicates that the time taken for growth of the crystallites decreases from 640°C to 720°C. This signifies that the nucleation time for crystallites also decrease as the crystallization temperatures increases. The crystallization time scale in the X-axis of Figure 3.11 was taken in a logarithmic scale in order to avoid congestion between the three curves which would be then be difficult to present and analyze.

3.5.4 Effect of crystallization temperature

Formulation of Avrami kinetics at three different temperatures in the crystallization range of bioactive glass 45S5 at a lower heating rate of 20°C/min revealed that increase in the crystallization temperature increases the rate of crystallization and decreases the crystallization time required to obtain a fully crystallized sample over the temperature range 640°C - 720°C.

Moreover, the variation in the values of 'k' and 'n' are given in Table 3.4. The values of 'n' ~ 3 at all the crystallization temperature indicate three dimensional growth of crystals irrespective of crystallization temperature.

But, it was observed that the value of rate constant 'k' increases with increasing crystallization temperature from 640°C to 720°C. This signifies increase in the rate of crystallization with increasing crystallization temperature (640°C to 720°C) which is well supported by the fact that lower crystallization times were required to get a fully crystallized sample with increasing crystallization temperature.

However, the same might not be true at temperatures higher than 720°C because earlier studies on construction of time-temperature-transformation (TTT) diagrams of different glasses have indicated that for each type of glass there exists a temperature in its crystallization range which corresponds to the nose on the TTT curve denoting fastest crystallization rate at this temperature and above which, the rate of crystallization starts to decrease again. In this case, the rate of crystallization was found to be increasing with increasing temperature up to 720°C. So there should be a temperature above 720°C which should correspond to the nose of the TTT curve in bioactive glass 45S5 and above which the crystallization rate would start to decrease. Hence, a future study on the crystallization kinetics at temperatures higher than 720°C may be conducted to formulate the entire TTT curve of bioactive glass 45S5. Moreover, formulation of a TTT curve in this case would not be accurate for higher crystallization temperatures as nucleation and growth of crystals would take place during ramping up at 20°C/min to the crystallization temperature as was evident from the optical micrograph obtained at 720°C for 0 minute (recall Figure 3.7 A). Thus experiments would need to be performed upon cooling from the melt; similar to austenitizing and heat treating of plain carbon steels.

3.5.5 Confirmation of bulk crystallization

The macrograph shown in Figure 3.13a depicts the cross section of a polished and etched partially crystallized sample (crystallized at 680°C for 30 min after a heating rate of 20°C/min) and the corresponding optical micrograph in Figure 3.12b at higher magnification obtained from the central region. The cross section indicates equivalent size of crystallites and similar degree of crystallinity throughout the sample volume when compared with the surface of a partially crystallized disc obtained by similar heat treatment (Figure 3.6 C and 3.10). This similarity provides further evidence of $n\sim3$, thus suggesting uniform bulk nucleation and three dimensional growth of crystals occurring in bulk bioactive glass 45S5.
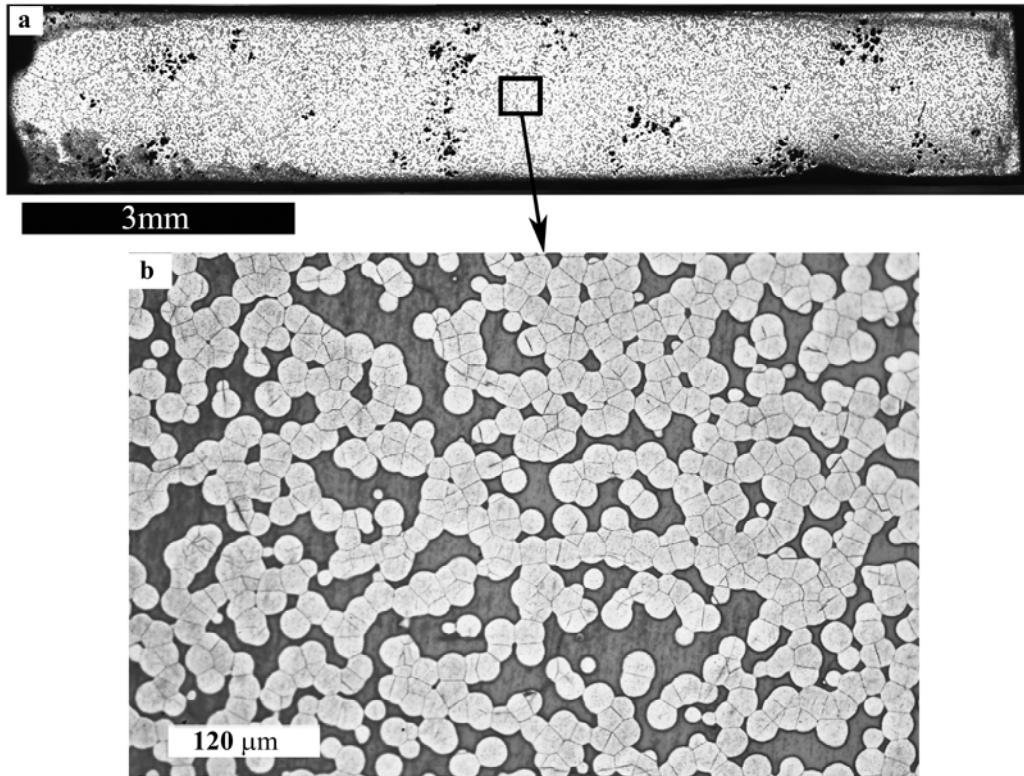
Fig 3.13: (a) Macrograph (b) Optical Micrograph showing the cross section of a partially crystallized bioactive glass 45S5 disc (crystallized at 680°C for 30 min) obtained after etching with 0.05%HF for 4s. The brighter areas show the crystallites formed while darker regions correspond to the amorphous phase. The boxed region in (a) indicates the area along the cross section from which the optical micrograph (b) was taken.

3.6 Effect of heating rate on crystallization kinetics

It may be possible that the nucleation had started during the ramp up (20°C/min heating rate) of the furnace to crystallization temperatures 640°C and 680°C, but it was assumed that such time does not affect the phase transformation because the time to reach the crystallization temperature from the room temperature was ~30 minutes. However, presence of crystallites for 0 minute at 720°C (dwell time of the sample at crystallization temperature of 720°C = 0 minutes) when the furnace temperature was ramped up at 20°C/min indicated that the rate at which a sample is heated to its crystallization temperature must affect the crystallization kinetics of bioactive glass 45S5. It was evident that the

nucleation and even growth of crystals had started during the ramp rate to such a high crystallization temperature (recall Figure 3.7A).

Since, the crystallization kinetics for a heating rate of 20°C/min at three different temperatures were already known, crystallization heat treatment cycles at the same three crystallization temperatures were carried out, but at a different heating rate. In order to study the effect of heating rate on crystallization kinetics, the samples were only inserted in the furnace after the desired crystallization temperature was reached; this provided the fastest heating rate possible using this technique as the samples were heated to the crystallization temperatures almost immediately (< 3 minutes). Hence, in this case, the residence time of samples in the crystallization range as they heat up to the desired crystallization temperature was much less than those samples used previously (inserted in the furnace at room temperature and heated to the crystallization temperature at 20°C/min). A comparative schematic diagram in Figure 3.14 shows the temperature profiles of the furnace at the two heating rates: Heating rate 1 - samples inserted after furnace reaches the crystallization temperature and Heating rate 2 - samples inserted at room temperature and the temperature was ramped up at 20°C/min to the crystallization temperature.

It can be seen from the Figure 3.14,

Slope of AB = BC/AC = Heating rate 1

Slope of AD = DE/AE = Heating rate 2

Since, Slope of AB > Slope of AD

So, Heating rate 1 > Heating rate 2

Higher heating rate > Lower heating rate

For the sake of convenience, the **heating rate 1 will be referred to as higher heating rate** and **heating rate 2 will be referred to as Lower heating rate** in this study hereafter. In both the cases, crystallization time was only taken into account after the furnace reaches the desired crystallization temperature (as denoted in Figure 3.14).
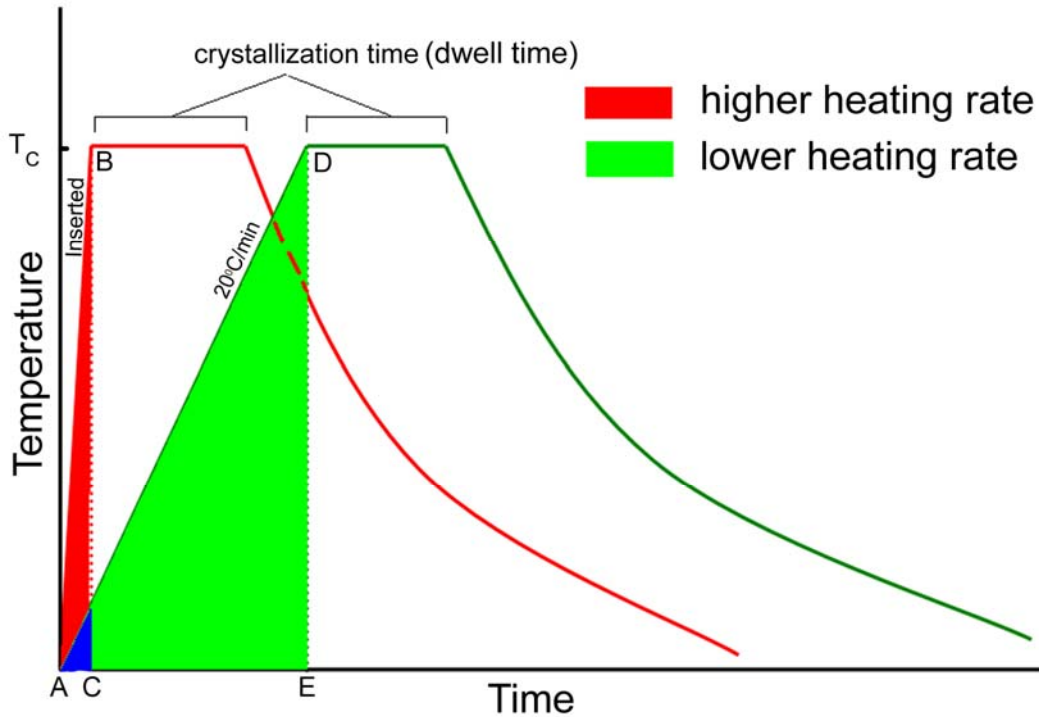
Fig 3.14: Schematic temperature profile showing heating rate of 20C/min (lower heating rate) and when sample was inserted in furnace at crystallization temperature (higher heating rate)

3.6.1 Crystallization at higher heating rate

Crystallization was carried out at a higher heating rate by inserting the bioactive glass samples in the furnace at 640°C, 680°C and 720°C for various crystallization times until a fully crystallized sample was obtained for each crystallization temperature. Macrographs and optical micrographs at higher heating corresponding to crystallization temperatures 640°C, 680°C and 720°C are shown in Figures 3.15 - 3.20. Even at a higher heating rate, transition from amorphous to crystalline glass ceramic was observed at all three temperatures similar to that observed when the samples were heated at 20°C/min to the crystallization temperature.

However, the macrographs and micrographs at all three temperatures revealed that amorphous bioactive glass 45S5 samples took longer durations of

65

time to fully crystallize when the heating rate was high as compared with the samples crystallized at a lower heating rate. This was due to the fact that the bioactive glass samples, with a higher heating rate, did not get much residence time in the crystallization range as the heating rate was very high, which led to lower overall crystallization rate. The time periods for all the crystallization calculations (dwell time at desired temperature) were noted only when the furnace temperature reached the desired crystallization temperature. Hence, for the same crystallization time and cooling time, at a lower heating rate (samples inserted at room temperature and ramped up at 20°C/min to crystallization temperature) the samples spent a longer duration of time in the crystallization range (600°C to 640°C or 680°C) during ramp up to 640°C and 680°C thereby allowing them to undergo nucleation during that time; whereas with much higher heating rate (inserted after furnace temperature reached crystallization temperature) the samples were heated to the crystallization temperature almost at once thereby experiencing shorter residence time in the crystallization range (from 600°C to 640°C or 680°C) during ramp up.

Moreover, at a higher heating rate, it was observed that no crystallization had occurred during ramping up of the sample temperature, as the samples got heated to the crystallization temperatures very quickly. Therefore, it was observed that higher heating rate decreased the rate of crystallization. The opposite was true for a lower heating rate; i.e. more crystallization occurred during ramp up due to two reasons; firstly, longer residence time of the samples in the furnace during ramping up to higher temperatures like 720°C; secondly, higher rate of crystallization at higher temperatures like 720°C.

Another important observation made concerning the heating rate was the increase in crystallite size at higher heating rates as compared to that obtained for a fully crystallized sample at lower heating rate. Comparative micrographs of fully crystallized samples obtained at 680°C with lower and higher heating rates are shown in Figure 3.21. A linear intercept method deduced by Fullman was used to measure the average grain size (refer section 2.4.3) of fully crystallized

samples from the optical micrographs obtained at all three crystallization temperature and both the heating rates as shown in Figure 3.22. The grain size data obtained was plotted as shown in Figure 3.23 which denotes the variation in the crystallite size range observed for fully crystallized sample obtained at lower and higher heating rates for all the three crystallization temperatures. It was found that the crystallite size obtained at higher heating rates were ~ 10-15μm larger in size as compared to that obtained in the case of lower heating rates. The crystallite sizes of a fully crystallized sample in the temperature range of 640°C - 720°C at higher heating rate were in the range 39-54 μm while that obtained at lower heating rates were in the range 28-31 μm. An increase in the crystallite size at higher rate was due to the short residence time of samples in the temperature range where nucleation would have been rapid, thus fewer nuclei would form. Fewer nuclei formed with higher heating rate had higher areas for them to grow before their growth was restricted due to impingement with other crystallites, thus producing larger crystallite size. This can be explained by Figure 3.24 which shows dependence of nucleation and growth rates at the two different heating rates on the amount of undercooling. Since at higher heating rate crystallization in the samples occurs at higher temperatures as compared to those at lower heating rates, hence, the amount of undercooling at higher heating rate is less which results in lower nucleation and higher growth rates, thus forming larger grains.

Moreover, an increase in crystallite size of fully crystallized samples was also observed at each heating rate with increasing temperatures. This was due to the fact that the at higher crystallization temperatures the amount of undercooling is less which leads to higher grain sizes. However, as seen in Figure 3.23, the effect of temperature change on the crystallite sizes was comparatively less than the effect of change in the heating rate.

Crystallization Temperature 640°C
(Higher heating rate)
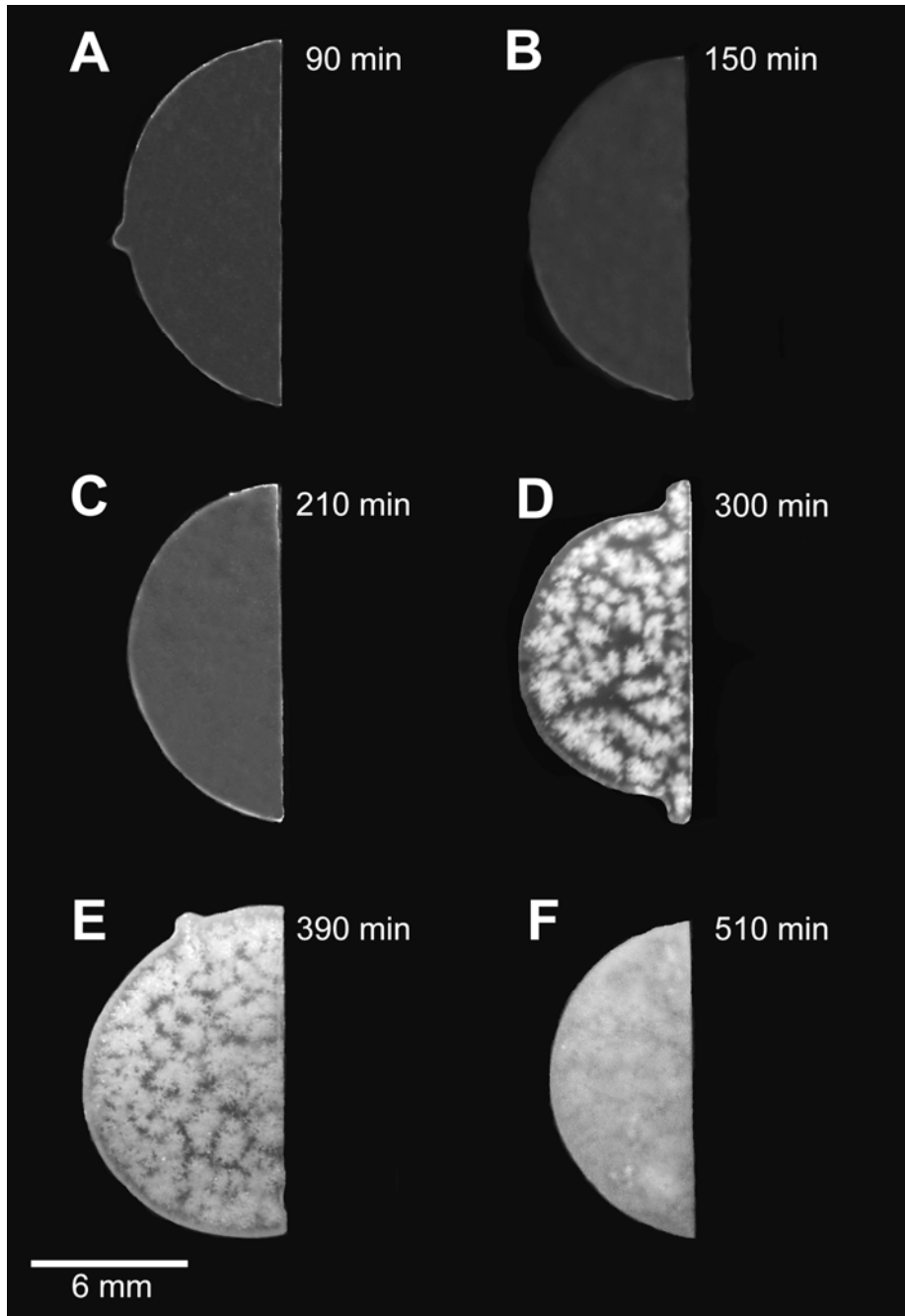
Fig 3.15: Macrographs of bioactive glass 45S5 samples crystallized at 640°C after a high heating rate (samples inserted in the furnace at 640°C) for dwell times of (A) 90 min (B) 150 min (C) 210 min (D) 300 min (E) 390 min (F) 510 min.

Crystallization Temperature 680°C
(Higher heating rate)
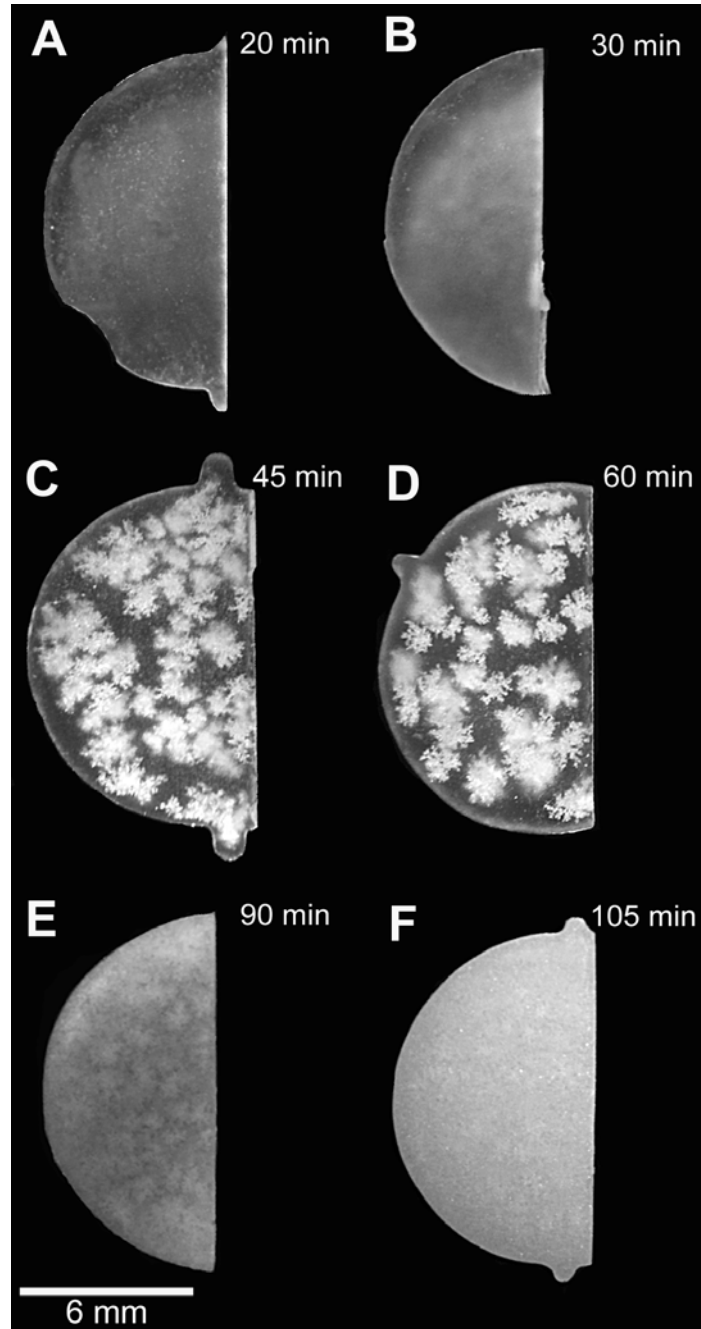
Fig 3.16: Macrographs of bioactive glass 45S5 samples crystallized at 680°C after a high heating rate (samples inserted in the furnace at 680°C) for dwell times of (A) 20 min (B) 30 min (C) 45 min (D) 60 min (E) 90 min (microcracking) (F) 105 min (microcracking).

Crystallization Temperature 720°C
(Higher heating rate)
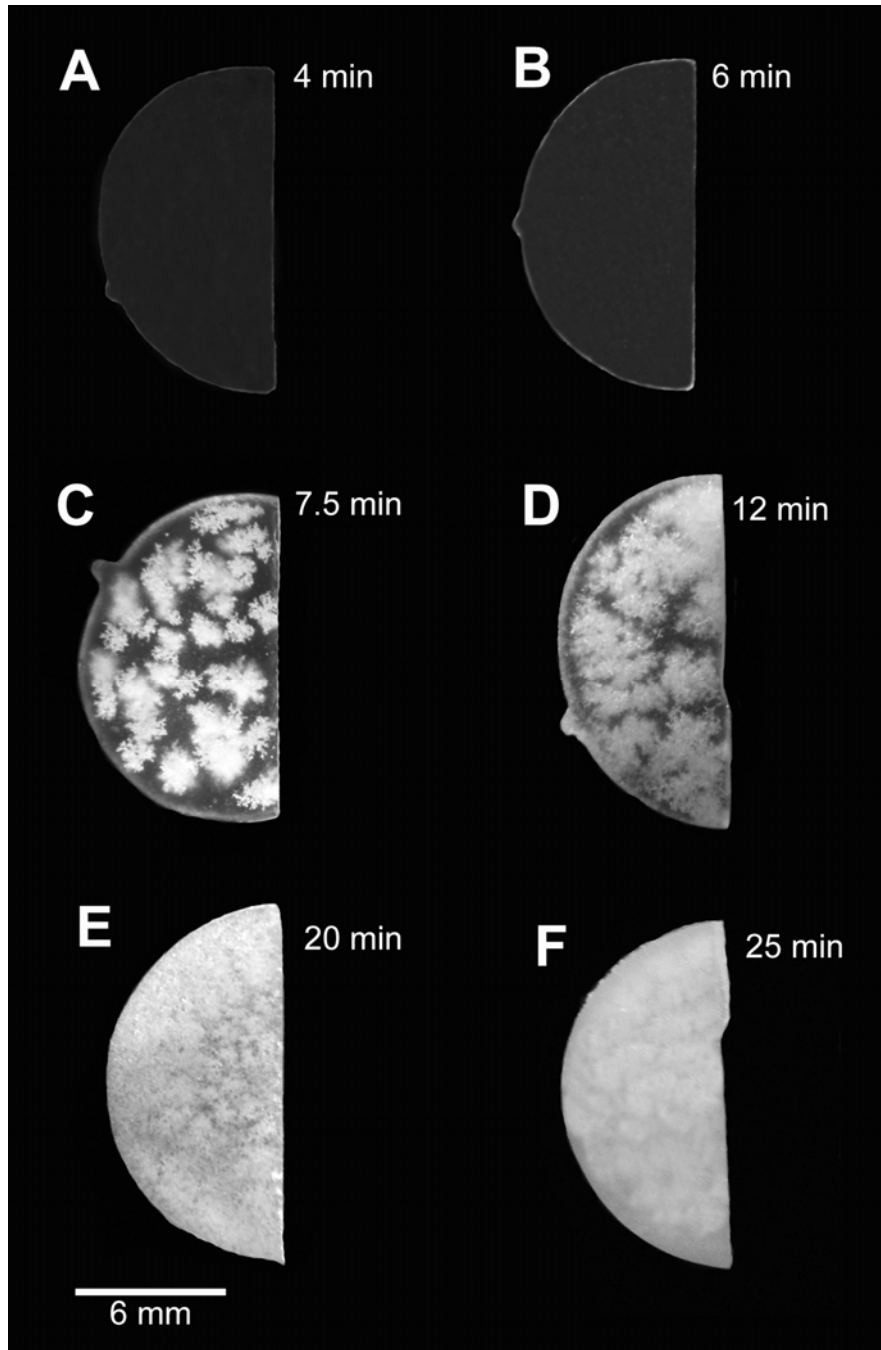
Fig 3.17: Macrographs of bioactive glass 45S5 samples crystallized at 720°C after a high heating rate (samples inserted in the furnace at 720°C) for dwell times of (A) 4 min (B) 6 min (C) 7.5 min (D) 12 min (E) 20 min (microcracking) (F) 25 min (microcracking).

Crystallization Temperature 640°C
(Higher heating rate)
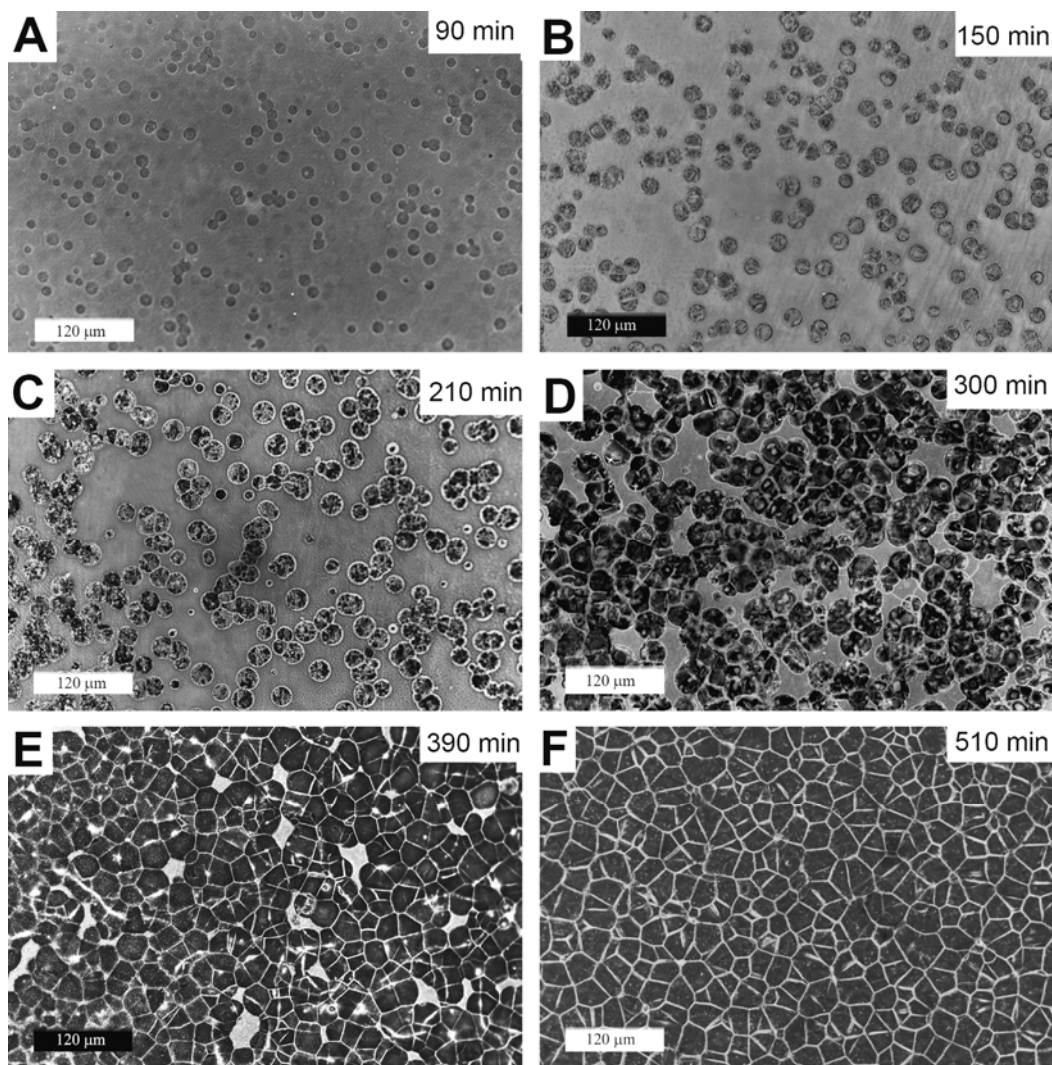
Fig 3.18: Optical micrographs of bioactive glass 45S5 samples crystallized at 640°C and etched with 0.05% HF for 5s after a high heating rate (samples inserted in the furnace at 640°C) for dwell times of (A) 90 min (B) 150 min (C) 210 min (D) 300 min (E) 390 min (F) 510 min.

Crystallization Temperature 680°C
(Higher heating rate)
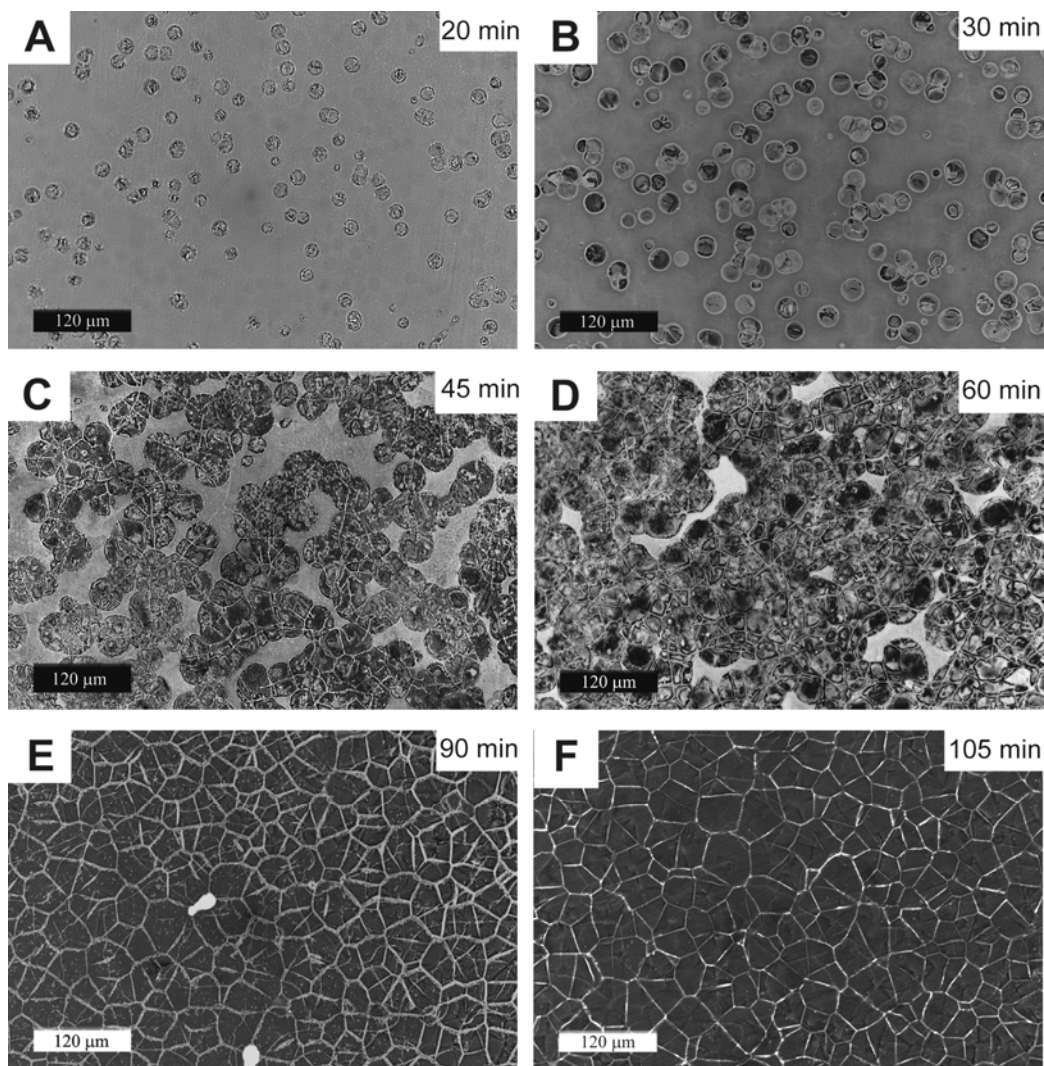
Fig 3.19: Optical micrographs of bioactive glass 45S5 samples crystallized at 680°C and etched with 0.05% HF for 5s after a high heating rate (samples inserted in the furnace at 680°C) for dwell times of (A) 20 min (B) 30 min (C) 45 min (D) 60 min (E) 90 min (F) 105 min.

Crystallization Temperature 720°C
(Higher heating rate)
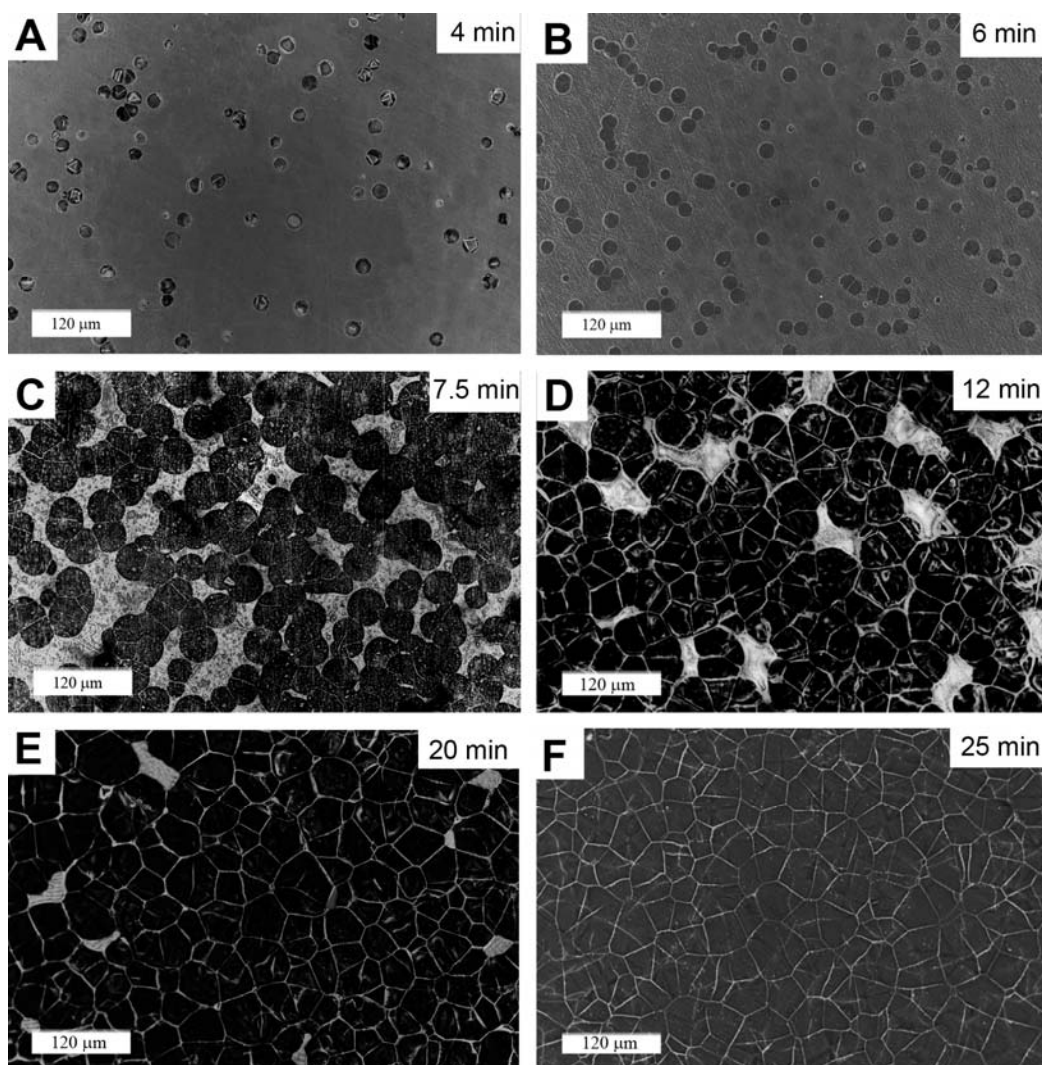
Fig 3.20: Optical micrographs of bioactive glass 45S5 samples crystallized at 720°C and etched with 0.05% HF for 5s after a high heating rate (samples inserted in the furnace at 720° C) for dwell times of (A) 4 min (B) 6 min (C) 7.5 min (D) 12 min (E) 20 min (F) 25 min.
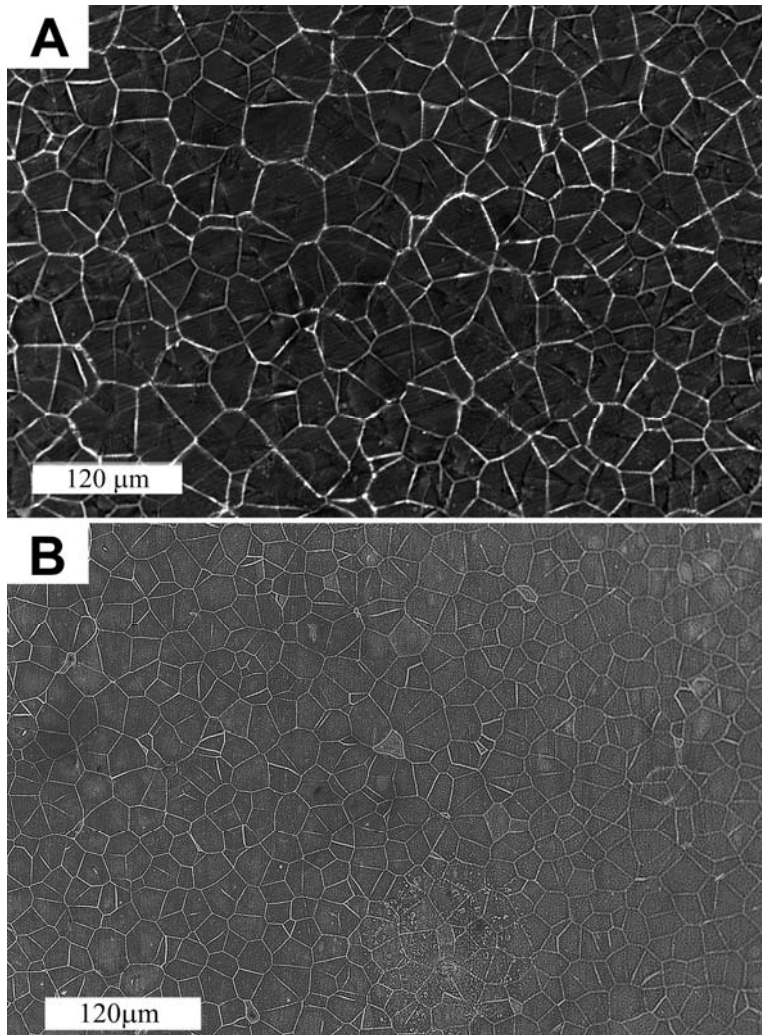
Fig. 3.21: Comparison of optical micrographs obtained from fully crystallized samples at the same crystallization temperature (A) crystallized at 680°C for 105 minutes at higher heating rate (B) crystallized at 680°C for 60 minutes at lower heating rate.

Note: The crystallization times required to obtain a certain volume fraction of crystalline phase were different at different temperatures for both the heating rates. Hence, the crystallite sizes would be different for equivalent crystallization times at different temperatures for both the heating rates.
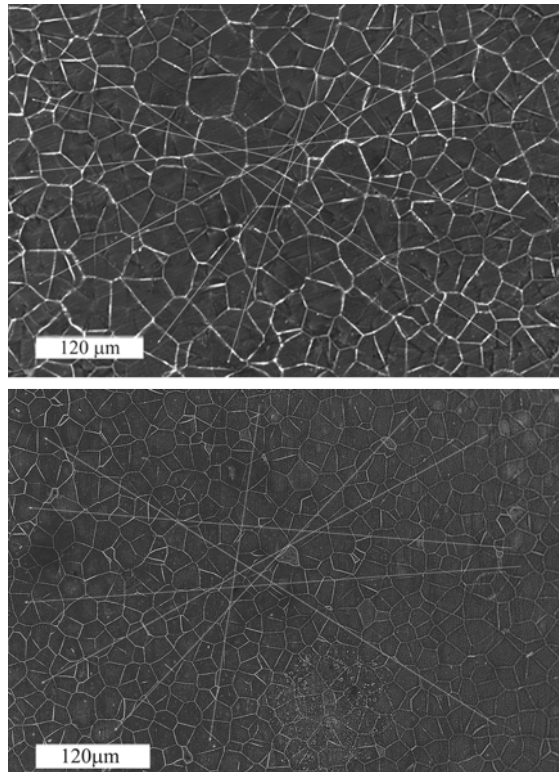
Fig. 3.22: Line intercept method for grain size measurements in fully crystallized samples at 680°C; (top) higher heating rate, (bottom) lower heating rate.
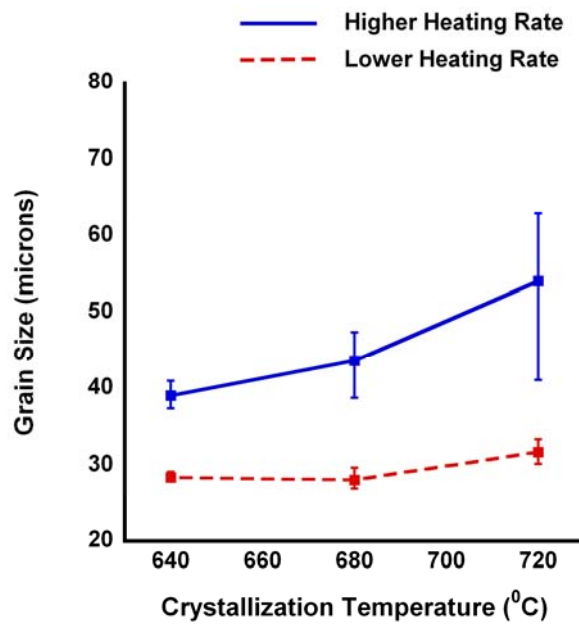
Fig 3.23: Crystallite size range comparison obtained in a fully crystallized sample at three different temperatures at lower and higher heating rates. Error bars indicate minimum and maximum values. N > 100 grain boundaries per data point.
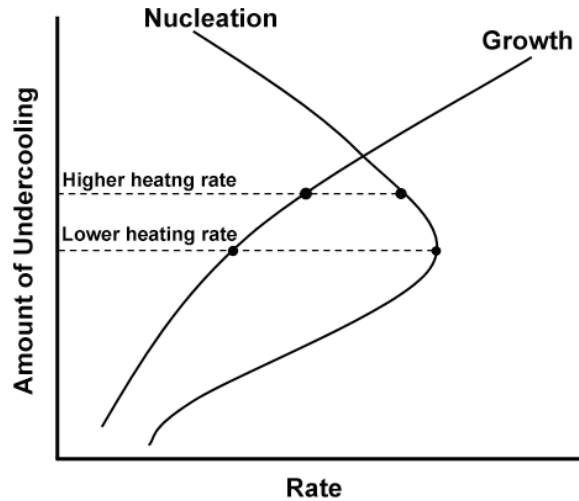
Fig 3.24: Plot showing the dependence of nucleation and growth of crystallites at two different heating rates on the amount of undercooling.

3.6.2 Avrami kinetics at higher heating rate

The crystallization kinetics at higher heating rate for three different crystallization temperatures was formulated using the Avrami Equation (Recall Equation 3.1) with ImageJ for area fraction calculation. Tables 3.5-3.7 provide the area fraction values obtained for 640ºC, 680ºC and 720ºC respectively. Crystalline fraction transformed '*f*' *versus* crystallization time '*t*' at 640ºC, 680ºC and 720ºC with higher heating rate were plotted (with curve-fits) collectively along with their corresponding lower heating rate data in Figure 3.25 in order to study the effect of heating rate on the rate constant '*k*' and Avrami exponent '*n*'. Since higher crystallization temperatures (720°C) required much lower crystallization times when compared with 640°C a comparative plot between these temperatures would be too condensed, so the crystallization time axis was plotted on a logarithmic scale. Comparative display of the values of '*k*' and '*n*' with respect to the change in heating rates is shown in Table 3.8. It was observed from the plot and Table 3.8 that the value of rate constant '*k*' deceases at higher heating rates for the same crystallization temperature indicating a decrease in the rate of crystallization at higher heating rate as compared to lower heating rate which was also evident from the fact that the samples took longer time to crystallize at higher heating rate. Moreover, the values of '*k*' increased with

increasing crystallization temperature at both lower and higher heating rates indicating an increase in rate of crystallization with increasing temperatures. However, this might not be true for temperatures higher than 720°C for reasons previously explained in section 3.5.4. The value of 'n' ~ 3 in all conditions signified that crystallization occurs in bulk bioactive glass 45S5 by three dimension growth of crystallites (bulk crystallization) irrespective of the variations in crystallization temperature, crystallization time or the heating rate to crystallization temperature.

A more commonly used version of the Avrami equation is in a logarithmic format (recall Equation 1.2), a plot of **ln (ln (1/ (1-f)))** *versus* **ln t** is shown in Figure 3.26 where '*f*' was crystalline fraction transformed and '*t*' was the crystallization time. This plot yielded straight lines at each temperature and heating rate, the slopes of which provided the value of '*n*' and the intercept that provided the values for '*ln k*' from which the value of '*k*' was calculated. This plot was a more comprehensive and easily understandable exhibit showing trends and variations in crystallization kinetics with respect to changes in crystallization temperature, crystallization time and the heating rate to crystallization temperature.

Crystallization time (min)	Crystalline Area Fraction				Min.	Max.
	I	II	III	Average		
0.0	0.000	0.000	0.000	0.000	0.000	0.000
90.0	0.124	0.113	0.120	0.120	0.005	0.006
150.0	0.252	0.287	0.284	0.274	0.013	0.022
210.0	0.421	0.413	0.430	0.421	0.009	0.008
300.0	0.852	0.855	0.862	0.856	0.006	0.004
390.0	0.949	0.960	0.959	0.956	0.004	0.007
510.0	1.000	1.000	1.000	1.000	0.000	0.000

Table 3.5: Crystalline area fractions calculated from three different optical micrographs for different crystallization times at 640ºC with higher heating rate.

Crystallization time (min)	Crystalline Area Fraction				Min.	Max.
	I	II	III	Average		
0.0	0.000	0.000	0.000	0.000	0.000	0.000
20.0	0.117	0.124	0.133	0.125	0.0083	0.008
30.0	0.435	0.38	0.317	0.377	0.05767	0.060
45.0	0.787	0.750	0.740	0.759	0.028	0.019
60.0	0.949	0.957	0.948	0.951	0.006	0.002
90.0	1.000	0.997	0.995	0.997	0.003	0.002
105.0	1.000	1.000	1.000	1.000	0.000	0.000

Table 3.6: Crystalline area fractions calculated from three different optical micrographs for different crystallization times at 680ºC with higher heating rate.

Crystallization time (min)	Crystalline Area Fraction				Min.	Max.
	I	II	III	Average		
0.0	0.000	0.000	0.000	0.000	0.000	0.000
4.0	0.077	0.077	0.068	0.074	0.003	0.006
6.0	0.105	0.129	0.126	0.120	0.009	0.015
7.5	0.759	0.746	0.737	0.747	0.012	0.01
12.0	0.911	0.920	0.892	0.908	0.012	0.016
20.0	0.972	0.977	0.978	0.976	0.002	0.004
25.0	1.000	1.000	1.000	1.000	0.000	0.000

Table 3.7: Crystalline area fractions calculated from three different optical micrographs for different crystallization times at 720ºC with higher heating rate.

Crystallization Temperature (°C)	Lower heating rate		Higher heating rate	
	Rate constant (k)	Avrami exponent (n)	Rate constant (k)	Avrami exponent (n)
640	3.0×10^{-7}	2.9	1.3×10^{-7}	2.9
680	5.1×10^{-5}	2.9	2.0×10^{-5}	2.9
720	2.0×10^{-3}	3.1	7.8×10^{-4}	3.2

Table 3.8: Values of 'k' and 'n' with respect to the change in heating rates at three different crystallization temperatures.
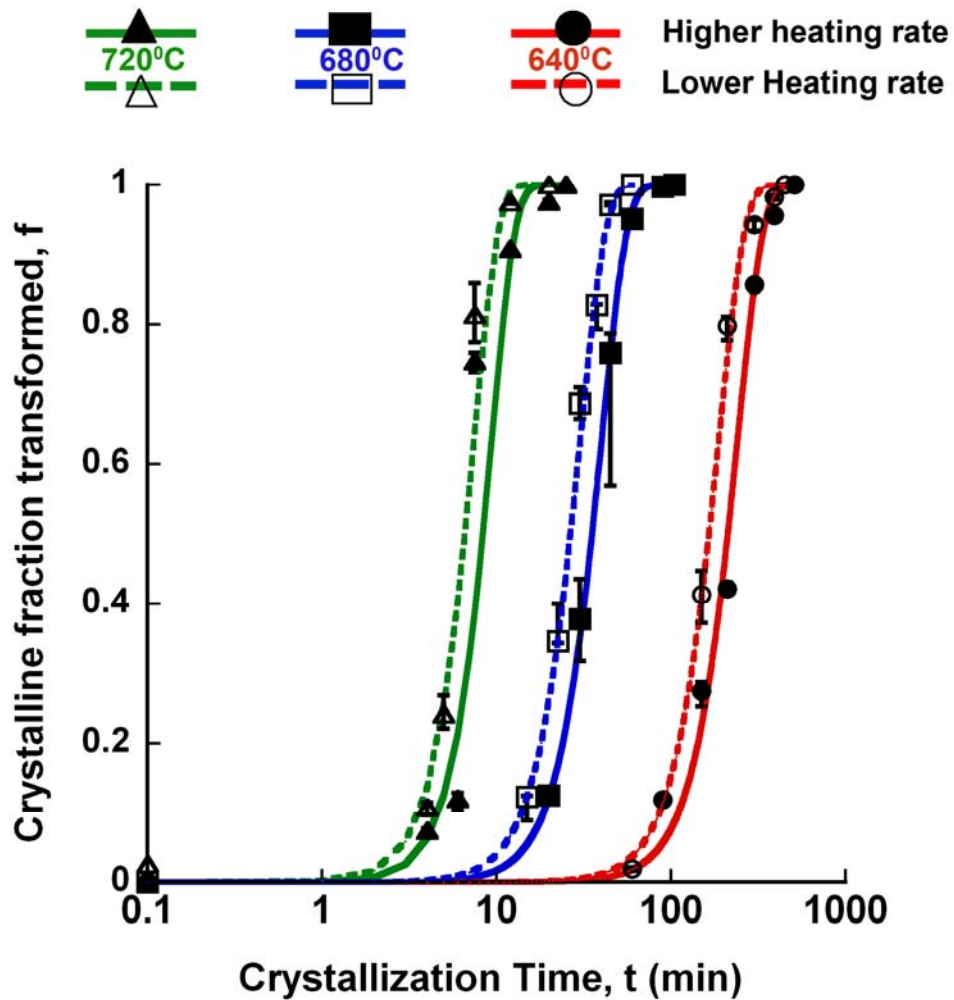
Fig 3.25: Crystalline fraction transformed *vs*. crystallization time (log scale) at two different heating rates each corresponding to three different crystallization temperatures.
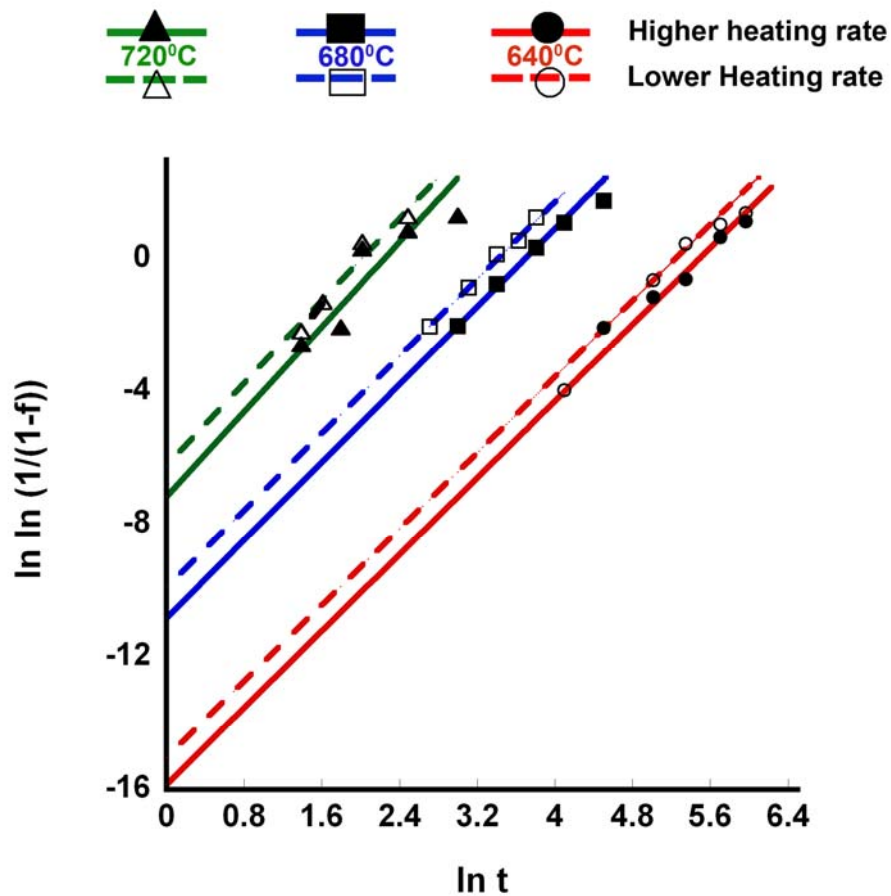
Fig 3.26: Avrami plot of [**ln (ln (1/ (1-f)))**] *versus* [**ln t**] at two different heating rates each corresponding to three different crystallization temperatures.

3.6.3 Construction of TTT curve

A TTT curve was constructed in Figure 3.27 (as per Figure 1.11) for bulk bioactive glass 45S5 using crystallization data of the three crystallization temperatures at higher heating rate. A TTT curve with lower heating rate would prove to be inaccurate since at crystallization temperature of 720°C crystal growth occurred during heating. TTT curves corresponding to 1%, 50% and 100% crystalline bioactive glass were constructed which correlated with the Avrami plots for isothermal transformations at all three crystallization temperatures. The correlation is shown for crystallization temperature of 720°C. Moreover, transformation points of 25% and 75% for all three temperatures were also shown for convenience. The TTT curve for 0% was not constructed as it was assumed
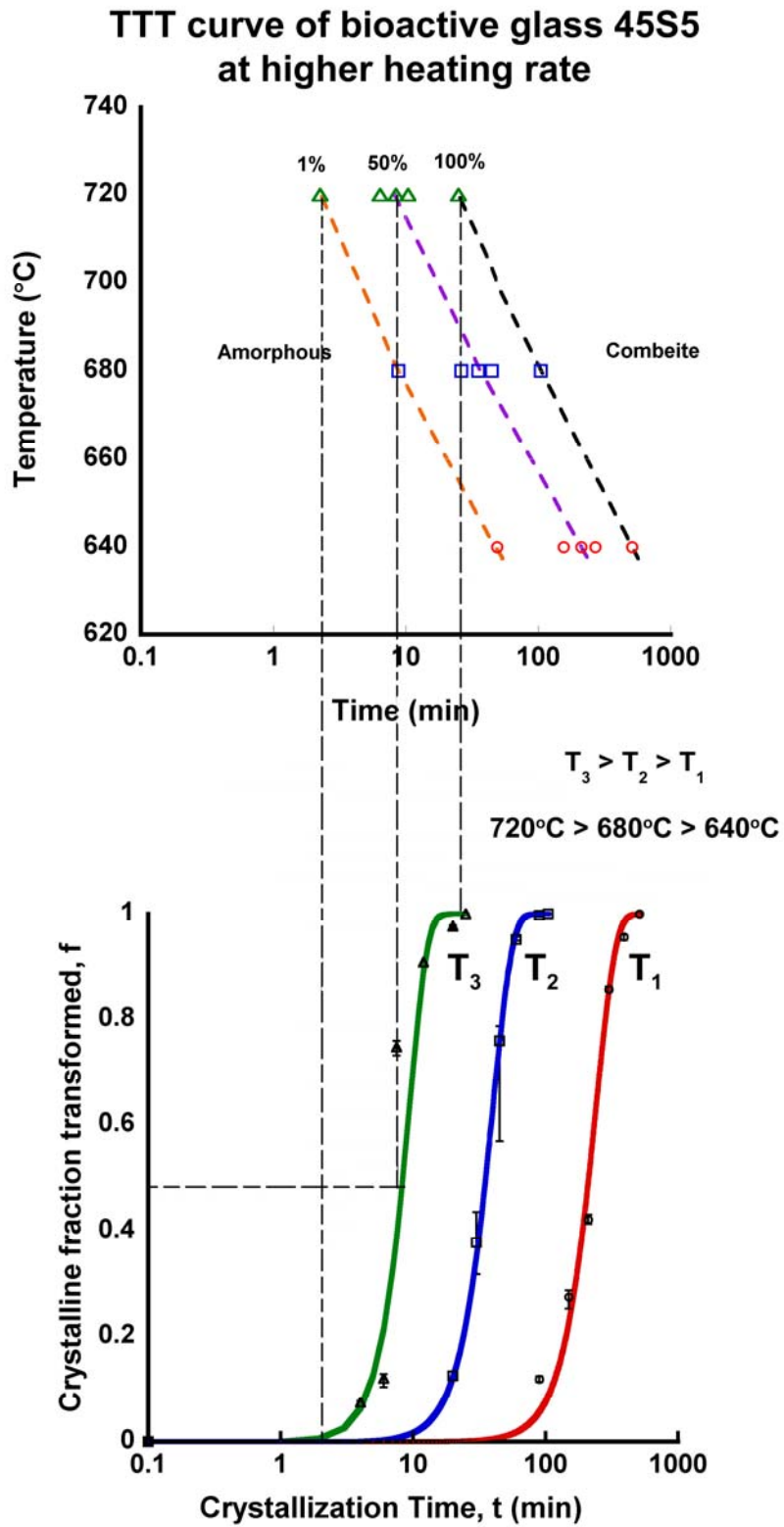
Fig. 3.27: TTT curve for bioactive glass 45S5 at higher heating rate.

that samples had no crystallinity at 0 min and with our method it would be very difficult to measure percentage crystalline in a sample with less than 1% crystallinity. It was evident that the crystallization temperature range chosen (640°C to 720°C) was below the nose of the TTT curve as the crystallization time required was still decreasing at 720°C. More experiments may be done in the future to determine the location of the nose of the TTT curve, so that the entire phase transformation kinetics can be obtained for this system.

3.6.4 Cracks at higher heating rate

It was mentioned before that after crystallization, sample surfaces were roughened thereby making it necessary to polish them again so that they could be characterized. During polishing of partially and fully crystallized samples for three different temperatures with higher heating rate, it was observed that small cracks developed from one of the edges (specifically the edge which comes in contact first against the motion of the polishing wheel). Depending on high or low degree of polishing required on the samples, these cracks would either stop or spread from the initiation area to the other parts of the sample. This was evident from the fact that the crack initiation/propagation areas in the sample start to become totally opaque once the cracks start propagating instead of showing the usual translucency that partially and fully crystalline samples exhibit (refer Figure 3.16 E and F, Figure 3.17 E and F). These microscopic cracks then propagated to the rest of the sample making it opaque. Such a transition has been shown in Figure 3.28 for partially crystalline sample obtained at 720°C with higher heating rate after crystallizing for 7.5 minutes.

The microscopic cracks were thought to be initiated at a particular edge in the sample due to the thermal shock it receives when it gets heated up to high crystallization temperatures within ~ 2-3 minutes (higher heating rate). Thereby, during polishing as a result of friction force between the sample and the polishing cloth, these cracks start to propagate. It was observed that if polishing was stopped in between, the crack propagation would stop producing a sample similar

to Figure 3.28(B). However, the cracks were so microscopic that the samples did not break or shatter in to pieces as a result of subsequent polishing or handling. It was important that macrographs were taken before polishing the samples as generation of cracks during polishing would give the wrong impression of higher crystallinity in the sample due to excessive light scattering by these cracks making the sample almost opaque.

| (A) | (B) | (C) |
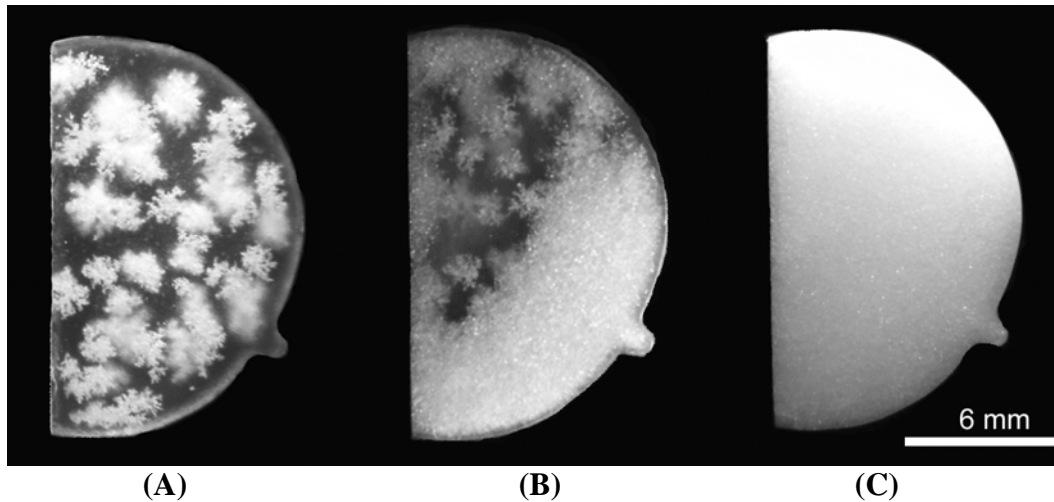
Fig 3.28: Time lapse macrographs showing transition of a translucent bioactive glass 45S5 sample partially crystallized at 720°C with higher heating rate for 7.5 min into opaque due to light scattering by internal microscopic crack propagation during polishing.

Figure 3.29 shows the optical micrographs of a fully crystallized sample obtained with higher heating rate at 720°C after crystallizing for 25 minutes. Both the micrographs Figure 3.29 (A) and (B) were taken at exactly the same location on the sample. However, both the micrographs were taken slightly out of focus in order to highlight the grain boundaries in (A) and the microscopic cracks developed in (B). As was evident from the micrographs, one had to be careful while characterizing samples crystallized with higher heating rates as the cracks tend to superimpose on the crystallites interfering with the observed microstructure; one might get the wrong impression of cracks being a grain boundary while it was just an artifact.
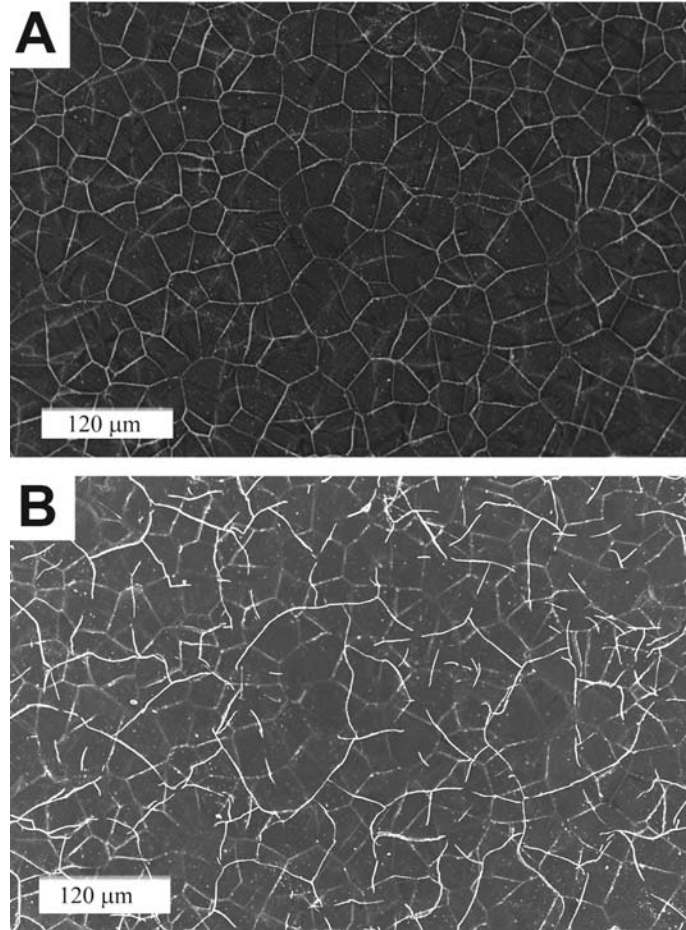
Fig 3.29: Optical micrographs of bioactive glass 45S5 sample fully crystallized at 720°C with higher heating rate for 25 min taken slightly out of focus in order to (A) highlight the grain boundaries (B) highlight the microscopic cracks.

3.7 Formation of voids during crystallization

After crystallization heat treatments it was observed that apart, from changes in the optical properties due to devitrification (transparent to translucent), optical properties were also changed at random locations in the samples due to the formation of "flowery patterns" inside the glass ceramic which contributed to lower transparency in these locations by greater light scattering. Figure 3.30 shows an example of these flowery patterns formed in a bioactive glass 45S5 sample partially crystallized at 680°C with lower heating rate for 30 minutes under reflected (3.30A) and transmitted lighting conditions (3.30B). These "flowery patterns" were not observed for samples with ~ 40% crystallinity.

However at greater amounts of crystallinity these flowery patterns become more and more prominent.

During and after polishing it was found that the sample surface contained pit like structures which were difficult to grind/polish off and seemed to be deep as is evident from the optical micrographs in Figure 3.31 which were taken slightly over focused in order to highlight the pits and some bright parts on the subsurface around the pits.
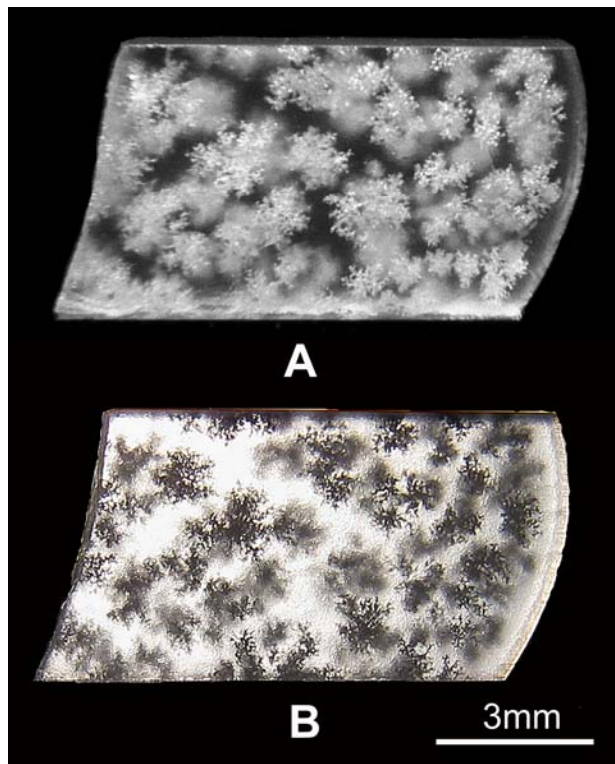
Fig. 3.30: Macrographs of partially crystallized sample (crystallized at 680°C for 30 min; lower heating rate) under (A) reflected light (B) transmitted light.

3.7.1 SEM analysis

Secondary electron micrographs of these pit like structures in unetched partially crystallized sample (Figure 3.32A) indicated that these might be interlinked voids formed in the sample since the morphology of these pit like structures showed elongated pits and even deeper holes present at the bottom of the pit as if it was interlinked with another pit through this hole. This became

more prominent in the SEM image of the pit like structures in an etched sample (Figure 3.32B) as it showed the pits forming at the edges of grains indicating that these depressions on the sample surface could be inter linked voids. Such voids may have formed due to shrinkage in the sample during crystallization. Due to bulk nature of the sample which hinders easy deformation, and nucleation/growth of a cluster of grains at isolated random locations, these voids were formed as a result of crystals forming and causing shrinkage along its peripheral areas, thus forming interlinked voids along the grain boundaries.
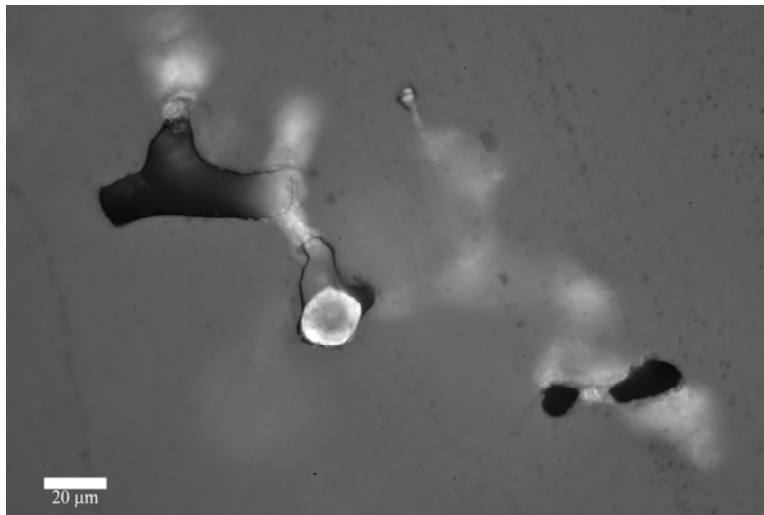
Fig. 3.31: Optical micrograph of a partially crystallized sample (crystallized at 680°C for 30 min; lower heating rate) taken slightly over focused showing voids on surface and in the subsurface.

3.7.2 Dye penetrant test analysis

In order to correlate the interlinked voids on the sample surface found after polishing with the "flowery patterns" that were seen in the macrographs, dye penetrant test was conducted. The macrograph in Figure 3.33(A) shows the voids present on the surface a partially crystallized sample after polishing. The corresponding macrograph of the same sample after the dye penetrant test shown in Figure 3.33(B) reveals that the dye had seeped through the voids on the surface to their respective ends, highlighting the "flowery patterns". It was thus evident that the "flowery patterns" formed in crystallized bioactive glass samples were

actually interlinked voids that formed "flowery patterns" at isolated locations due to shrinkage during crystallization or volatilization of grain boundary phase by creating pressure pockets. Though the flowery patterns were formed by interlinked voids found at isolated locations but they were not interlinked with other voids. Hence, only those flowery patterns, whose interlinked voids were opened to the surface, were only detected by the dye.
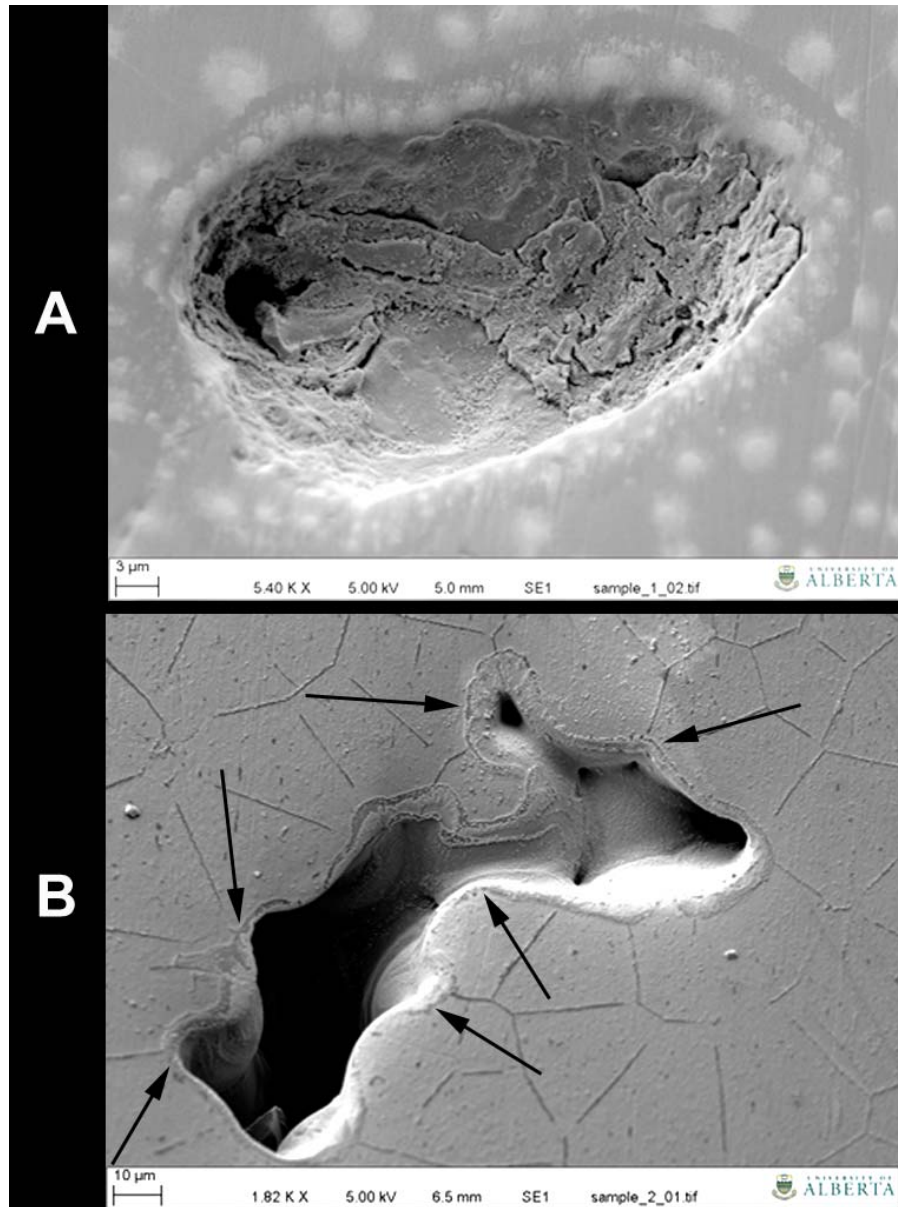
Fig. 3.32: Secondary electron micrograph of partially crystallized sample (crystallized at 680°C for 30 min; lower heating rate) showing interlinked voids (A) unetched sample (B) sample etched with 0.05% HF for 4s (arrowheads indicate formation of voids at the grain boundaries).
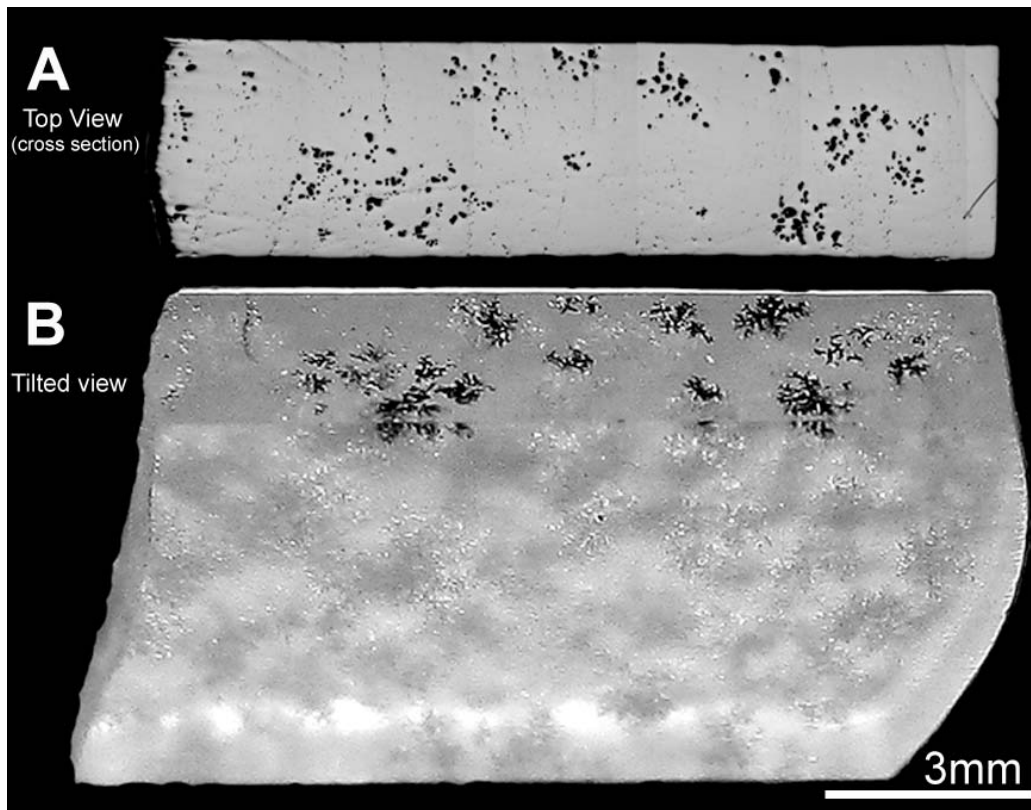
Fig. 3.33: Macrographs of an unetched partially crystallized sample (crystallized at 680°C for 30 min; lower heating rate) showing (A) voids on the surface after polishing (B) Dye penetrating through the voids on the surface highlighting the flowery patterns.

3.8 Chapter summary

Knowledge of the crystallization kinetics is paramount for producing a bioactive glass ceramic with the desired degree of crystallinity. With this objective, Avrami kinetics of crystallization was formulated for bulk bioactive glass 45S5 in the crystallization temperature range of 640°C - 720°C. The observations and conclusions in this temperature range which can be drawn from this study are provided below:

- Thermal treatment at a desired temperature for various times revealed an increase in the degree of crystallinity with increasing crystallization time following Avrami kinetics.

- Change in the optical properties from transparent (amorphous) to translucent occurred with increasing crystallinity.

- Increasing the crystallization temperature increased the crystallization rate by decreasing the time required to obtain a fully crystallized sample.

- XRD data revealed that the crystalline phase formed in bioactive glass 45S5 was Combeite ($Na_2Ca_2Si_3O_9$; ICDD PDF Card #075-1687).

- For the same crystallization temperature, higher heating rate decreased the crystallization rate.

- For the same heating rate, the Avrami rate constant "k" increased with increasing crystallization temperature indicating an increase in the crystallization rate. However, for the same crystallization temperature, "k" decreased at higher heating rates.

- Avrami exponent 'n' was ~ 3 irrespective of crystallization temperatures and heating rates indicating three dimensional growth of crystals (bulk crystallization) with uniform nucleation occurring in bulk bioactive glass 45S5.

- Nucleation and growth during ramping at lower heating rate was detected from micrographs showing crystals for 0 minute dwells at the crystallization temperature (720°C), implying that the phase transformation occurred during ramp up.

- For the same heating rate, the time required to obtain a fully crystallized sample increased with decreasing temperature and the crystallite size of these fully crystallized samples increased with increasing temperatures. Grain size increase from ~ 28 - 31μm at lower heating rate to ~ 39 - 54μm at higher heating rate was observed for a full crystallized sample showing greater effect of heating rate change on the grain size than the effect of temperature change.

Thus, it was observed that the crystallization kinetics was affected by time, temperature and heating rate and these parameters can be varied to obtain a variation in the microstructure. An attempt at construction the TTT curve for bulk

bioactive glass 45S5 was made with the available crystallization data. However, the TTT curve indicated that the chosen crystallization temperature range (640°C -720°C) was below the nose of the TTT curve.

It was also found that the "flowery patterns" formed during crystallization which provided an added translucency and formed pits during polishing in the samples were actually interlinked voids formed beside clusters of grains (along grain boundaries) likely to have formed due to shrinkage during crystallization or volatilization of grain boundary phase.

CHAPTER 4

Crack propagation and fracture*

4.1 Introduction

One of the motivations to study the crystallization kinetics of bioactive glass 45S5 was to formulate ways to improve its fracture toughness and other mechanical properties. As discussed previously, the idea was to manufacture a glass ceramic dispersion of optimum crystalline phase in an amorphous matrix which would increase the fracture toughness as cracks propagating through the amorphous matrix would be hindered or deflected by the crystals.

Pursuing this line of thought, glass ceramic versions of bioactive glass 45S5 were developed by crystallization to different amounts of crystalline phase dispersed in the amorphous matrix. In this chapter, testing and characterizing the mechanical properties of the glass ceramic and comparison with its amorphous counter part will be discussed.

4.2 Crack propagation study by microindentation

Nychka and co-workers [28, 36] had previously established the hardness, Palmqvist crack (cracks emanating from the corners of the indents) features and fracture toughness of amorphous bioactive glass 45S5 using Vickers indentation technique which use the Palmqvist crack lengths in determination of fracture toughness of a material using the Equation 4.1.

$$P = \left(K_{IC} / \delta \right)\left(E / H \right)^{-1/2} c^{3/2} \qquad (4.1)$$

where

K_{IC} – fracture toughness (MPam$^{1/2}$),

P – indentation load (N),

E – Young's modulus of the material (GPa),

H – Hardness of the material (GPpa),

δ – an empirical constant of 0.016 ± 0.004 for the Vickers indentation, and

c – half length of Palmqvist crack (m); $2c$- total length of crack).

4.2.1 Amorphous bioactive glass 45S5

A similar technique was used to study the Palmqvist crack propagation in amophous bioactive glass 45S5 samples. It was observed that the Palmqvist cracks emanating from the indent tips propagated in a straight line without any hindrance. Moreover, it was also noticed that Palmqvist crack lengths for a particular indentation load were relatively consistent with each other ($2c$ = 110.1±3 μm). Such an example of straight Palmqvist cracks is shown in the optical micrographs of Figure 4.1 which shows Vickers indents made with an indentation load of 300gf (2.940N). The indent sizes and crack lengths decreased with decreasing indentation load. This indicated uniformity in the material which justifies the amorphous structure and crack lengths depending on the indentation load as per the Equation 4.1. A schematic of the crack paths is shown beside each optical micrograph in Figure 4.1 for easy tracking of crack paths.

Moreover, subsurface lateral cracks were also seen for indentations at higher loads of 200gf (1.9614 N) and above imaged through a bright reflection around the indent (as seen in Figure 4.1) signifying the lateral crack path below the surface.
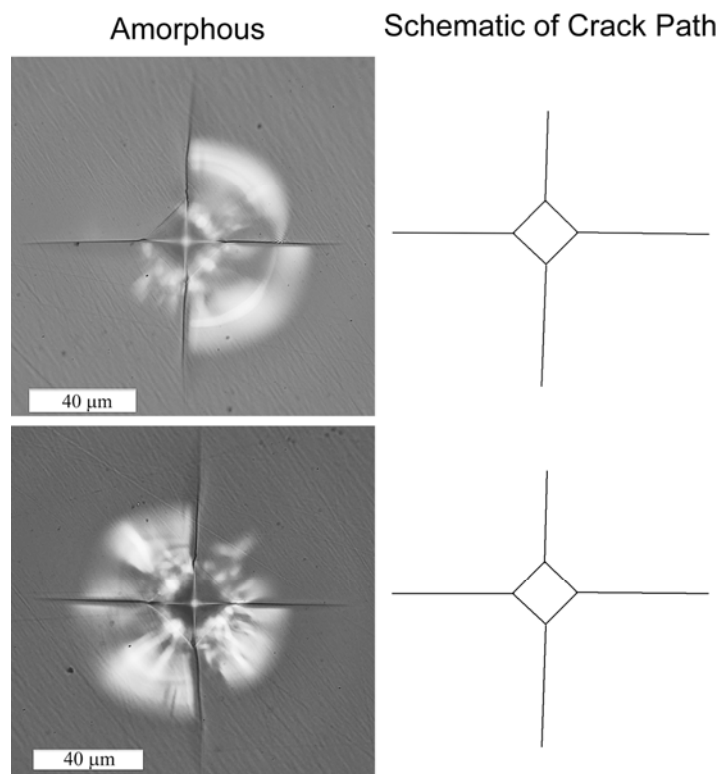
Fig 4.1: Optical micrographs and corresponding schematic figures showing Palmqvist crack propagation paths observed in amorphous bioactive glass 45S5 carried out by Vickers indentation technique. Indentation load was 300gf (2.940N).

4.2.2 Partially crystallized bioactive glass 45S5

Vickers indentation technique was also implemented on partially crystallized bioactive glass 45S5 samples (crystallized at 680ºC for 30 minutes, lower heating rate) with the objective of conducting comparative crack propagation study in amorphous and crystalline phases. These samples had ~ 68% crystalline phase containing almost equal amounts of crystalline and amorphous regions allowing better resolution for analysis of crack propagation behaviour in both the phases.

Figure 4.2 shows utilization of Vickers indentation technique in partially crystallized bioactive glass 45S5 samples. It was observed that the Palmqvist cracks developed in partially crystallized bioactive glass did not traverse in a straight line as seen in amorphous bioactive glass. On the contrary, the cracks in

partially crystallized bioactive glass followed no particular pattern; they originated at different points all along the periphery of the indents and deflect at many points throughout the crack path. Deflections approximately as high as 30° were observed in some cases. It can be inferred from this observation that the cracks might traverse through the path of least obstruction or through points where it consumed the least amount of surface energy required to form crack surfaces – indicating that the cracks propagated along the preferred crystallographic orientation in the crystallites. Since different grains have different crystallographic orientation with respect to each other, the preferred plane for crack propagation might not have been that in which the initial crack was propagating. The cracks had to twist themselves from the original plane of propagation to the preferred crystallographic plane whenever they encountered a different orientation along the path. Straight crack propagation in crystalline regions can be attributed to similar (or equivalent energy) crystallographic orientation among adjacent grains.

This result signifies that crack propagation might be hindered if the crystals are oriented at different angles to the direction of the crack path since more energy is required for deflection towards the preferred crystallographic orientation. If crystals could be produced at angles much different than the direction of crack propagation, then it might increase the fracture toughness by crack deflection as the crack traverses from one preferred crystallographic plane to another.

However, the crack deflection at crystallites might also occur due to thermal mismatch strain generated in the samples after the phase transformation during crystallization. Although the partially crystallized samples were annealed after crystallization heat treatment the presence of residual strain due to volume change during crystallization or different coefficient of thermal expansions between the phases cannot be ignored. Residual thermal stresses may also have contributed to observed crack deflections due to strain fields across the crystallite-amorphous phase boundary. However, a lack of property data concerning the

crystalline and amorphous phases prevents further model development to calculate such thermal residual stresses.

Etching and light interference from the optical microscope provides different colors in the micrograph which is not possible to discard and they provide poor imaging conditions for the crack paths. Hence, for the convenience of the readers we have included the schematic of the crack paths along with the optical micrographs.
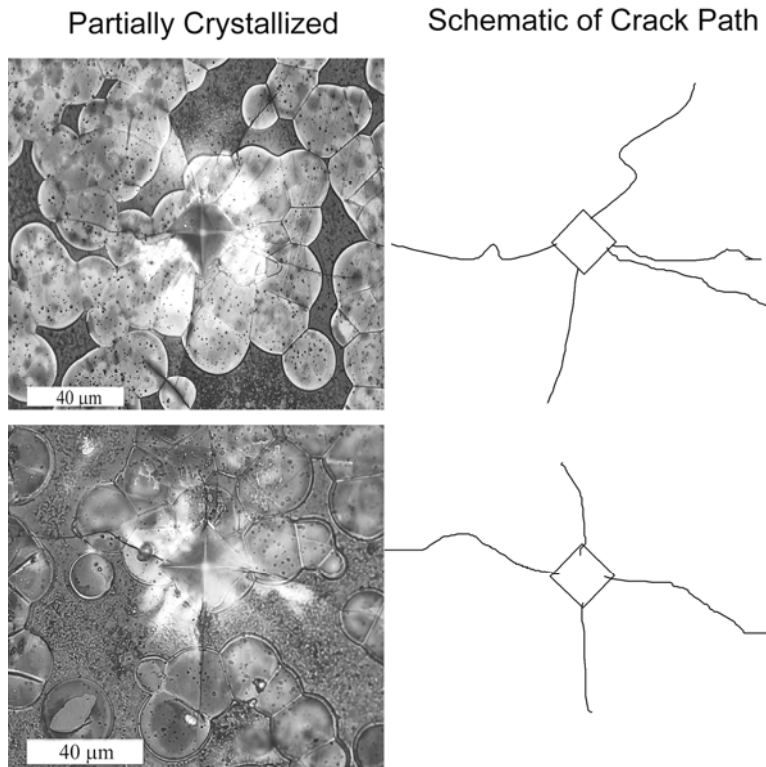
Fig. 4.2: Optical micrographs and corresponding schematic figures showing Palmqvist crack propagation paths observed in crystallized (crystallized at 680ºC for 30 min) bioactive glass 45S5 carried out by Vickers indentation technique. Indentation load was 300gf (2.940N).

4.2.3 Crack path as a function of crystallinity

In an attempt to study crack propagation in bioactive glass 45S5 as a function of crystallinity; crack propagation in three samples crystallized at 680°C at low heating rate for three different time intervals 22.5 minutes (~35%

crystallinity), 30 min (~68% crystallinity) and 60 minutes (100% crystallinity) were studied using Vickers indentation technique. Figure 4.3 shows the crack paths formed in three samples with different amounts of crystallinity. It was observed that the sample with lowest crystallinity (~ 35%) crack paths were relatively straight with some amount of deflection at the crystallites and cracks generating around the periphery of the indent rather than its corners (Figure 4.3 A). At even higher crystallinity (~ 68%) it was observed that the crack paths were even more random with higher degrees of deflection at the crystals indicating that crack propagation might have occurred along the preferred crystallographic orientation (Figure 4.3B). Figure 4.3C shows the crack paths in a fully crystalline sample (crystallized at 680°C for 60 minutes) which was not etched in order to eliminate light interference from the optical microscope caused by etching. Since the sample was fully crystalline so it was evident that the indented area was crystalline as well. It was observed that the crack propagation was transgranular and random with deflections at various locations along its length. One of the cracks bifurcated along its length and formed another crack almost perpendicular to its direction of propagation.

It was previously discussed that in section 1.6 that an optimum crystal dispersion, crystal size and location can only hinder crack path by twisting around crystals (due to thermal mismatch strain fields or preferred crystallographic orientation). However, in this experiment crack paths twisting around crystals were not observed which may be due to the fact that the optimum crystal volume fraction was not chosen for testing, or the thermal mismatch strain is not great enough. Hence, an in depth analysis may be carried out in future by studying crack propagation as a function of crystallinity and quantitative analysis may be done on the crack paths so as to find out the possibility of an optimum crystalline volume fraction which would hinder crack path by twist along crystals, thereby increasing fracture toughness. Nevertheless, the following section demonstrates an increase in fracture resistance during thermal shock testing of glass ceramic materials.
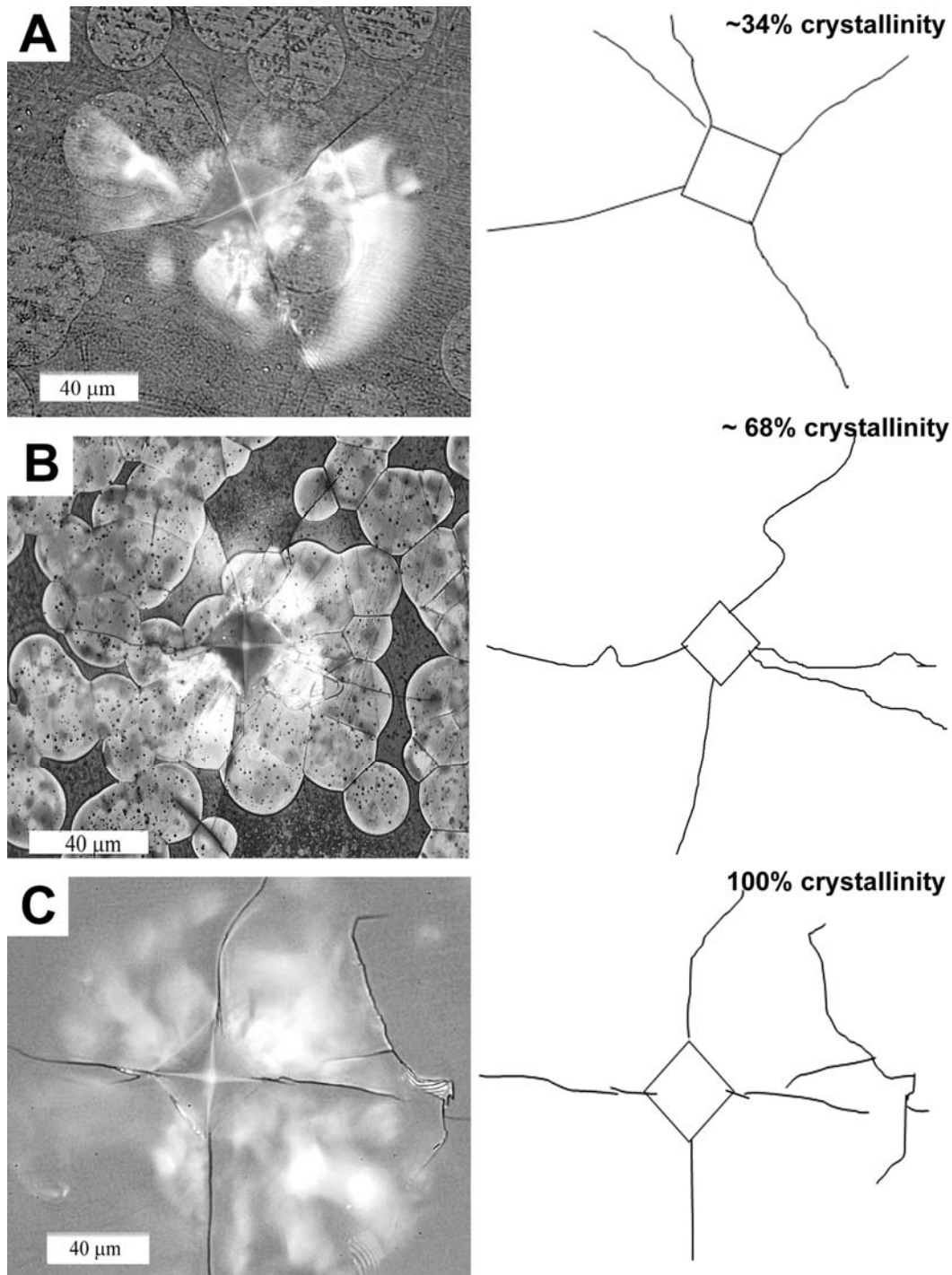
Fig. 4.3: Optical micrographs and corresponding schematic figures showing Palmqvist crack propagation paths observed in samples crystallized at 680C for (A) 22.5 min (~35% crystallinity) (B) 30 min (~68% crystallinity) (C) 60 min (100% crystallinity) carried out by Vickers indentation technique. Indentation load was 300gf (2.940N). The fully crystallized sample (C) was not etched in order to eliminate light interference (caused by etching) from the optical microscope.

4.3 Crack propagation and fracture by quenching

Another attempt was made to conduct a comparative study on the mode of fracture occurring in amorphous and partially crystallized bioglass ceramics. In this case, the amorphous bioactive glass was heated to a crystallization temperature of 680°C and then quenched in water at room temperature while another amorphous sample was heated to 680°C and kept at this temperature for 30 minutes to partially crystallize before being quenched in water. Fracture details of both the amorphous and partially crystallized samples are provided in the succeeding sections.

4.3.1 Fracture in amorphous bioactive glass 45S5

It was observed that upon quenching from a temperature as high as 680°C, the amorphous glass disc (recall figure 3.1A) shattered and exploded into many pieces. Macrograph of the shards of this amorphous sample is shown in Figure 4.4.

Fig. 4.4: Macrograph of shattered pieces of amorphous bioactive glass 45S5 after it was quenched from 680°C.

It was evident that the amorphous sample was not able to withstand the high thermal shock it received when quenched from 680°C. The fracture surfaces from the macrographs were not clear. Therefore, SEM was conducted to have a closer look at the fracture surfaces. Figure 4.5 shows the secondary electron micrographs depicting the fracture surfaces of a quenched amorphous sample. The micrographs revealed a brittle fracture (mirror) occurring in the interior of the sample without much evidence of any toughening, except along the periphery of the sample where it showed cleavage fracture (hackle) along different planes.
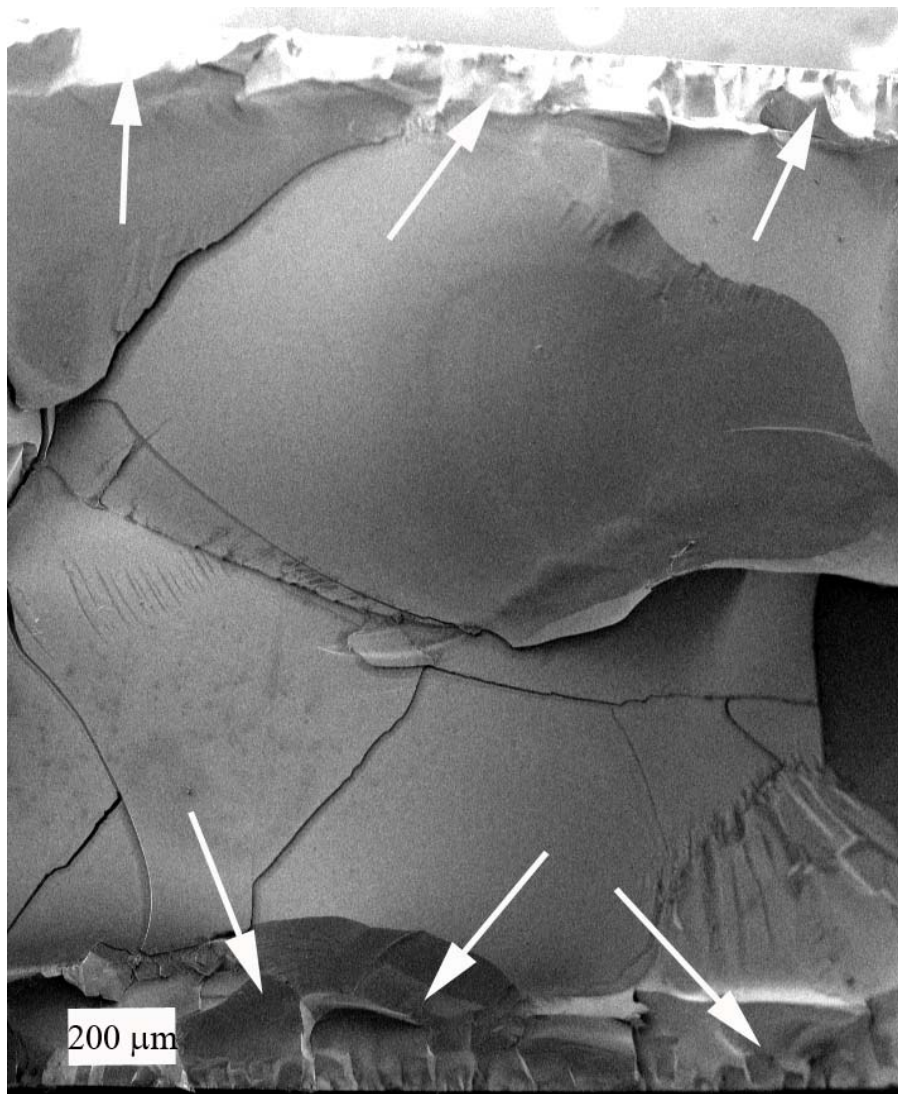
Fig. 4.5: Secondary electron micrograph of cross section fracture surface in amorphous bioactive glass 45S5 after it was quenched from 680°C. The arrow heads show hackle type fracture at the periphery.

4.3.2 Fracture in partially crystallized bioactive glass 45S5

On quenching a partially crystallized (crystallized at 680ºC for 30 minutes, lower heating rate) bioglass 45S5 sample from 680°C to room temperature, it was found that the sample did not shatter into pieces like the amorphous sample; on the contrary it developed a lot of macroscopic cracks in it making it more translucent due to light scattering by the cracks. The macrograph of a quenched partially crystallized sample is shown in Figure 4.6 which indicates the macroscopic cracks formed in it as a result of thermal shock. Such cracking indicates a rise in the thermal shock resistance, which might have been due to the presence of crystals in the sample which deflected/hindered the crack propagation thereby increasing its resistance to brittle fracture. This can also be correlated to the Palmqvist crack deflection produced in crystals as seen in the optical micrographs of a partially crystallized sample (recall Figure 4.2)

Fig. 4.6: Macrograph of a partially crystallized (crystallized at 680ºC for 30 min, lower heating rate) bioactive glass 45S5 sample after it was quenched from 680°C.

In order to confirm the fact that crystallization of the bioactive glass sample had increased its resistance to cracking and thermal shock resistance, the

cracked sample in Figure 4.6 was broken manually so that the fracture surfaces of this sample could be studied. A macrograph of the manually broken sample shown in Figure 4.7 reveals that the sample broke along the already cracked planes (cracked planes seen in Figure 4.6). Although macroscopic cracks were present all over the sample the sample broke along the already cracked planes which were parallel to the applied manual force without shattering the whole sample.

Fig. 4.7: Macrograph of the partially crystallized and quenched bioactive glass sample after it was **manually broken**.

Secondary electron micrograph of the fractured surface of a partially crystallized sample quenched from 680°C is shown in Figure 4.8. An important observation made was that although the sample fractured along the cracked planes, each cracked plane was blanketed with numerous small cleavage planes (mist). The numerous small cleavage planes seemed to change direction after every 30-40 microns. Cleavage cracks encounter a grain boundary (twist mismatch) oriented at a different angle than the current cleavage plane and they change direction to accommodate the twist mismatch and propagate along a different plane. The twist paths formed as a result of a cleavage crack crossing a grain boundary between crystallites was evident from the high magnification secondary electron micrograph of the fracture surface in Figure 4.9. The twist paths signify that crack propagation consumed more energy as it twisted along the cleavage planes thereby increasing the resistance to cracking. Thus, the twist mismatch at different crystallographic oriented planes posed a lot of hindrance for cracks to propagate in a partially crystallized sample. This can be correlated to the

increase in fracture toughness in a partially crystallized sample as compared to an amorphous one, as it absorbs more energy during crack propagation.
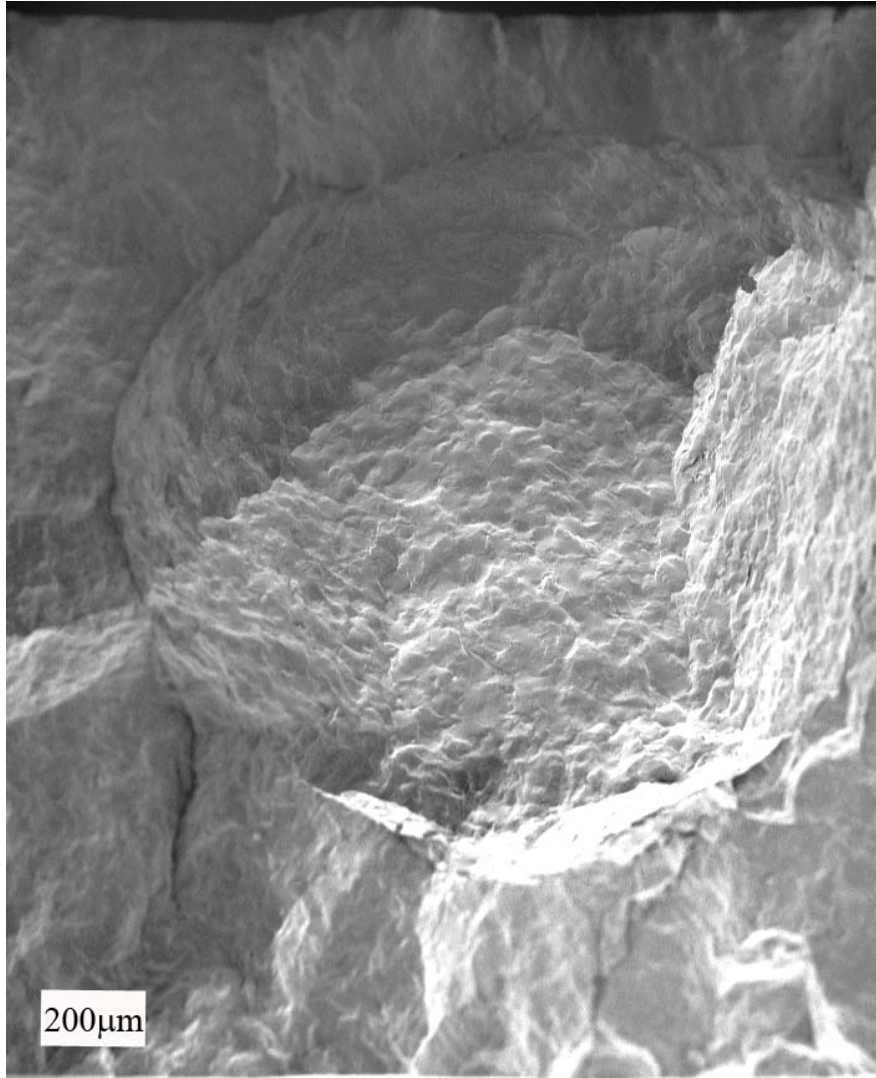
Fig. 4.8: Secondary electron micrograph of fracture surface in partially crystallized (crystallized at 680ºC for 30 min, lower heating rate) bioactive glass 45S5 after it was quenched from 680°C.
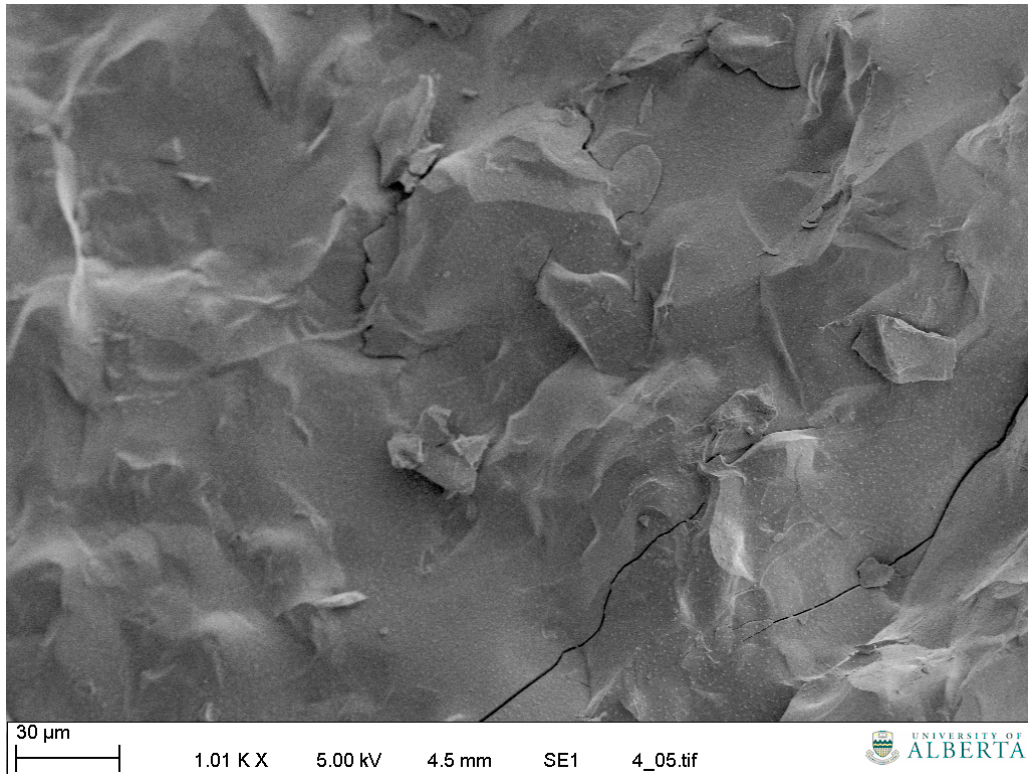
Fig. 4.9: Secondary electron micrograph of fracture surface in partially crystallized bioactive glass 45S5 at higher magnification showing twist paths.

4.4 Possible effects of "flowery patterns" and microcracks

It has been previously shown that the "flowery patterns" formed during crystallization of bioactive glass 45S5 were actually interlinked voids likely to have formed due to shrinkage during crystallization. Presences of these voids can possibly affect the fracture behaviour in partially crystallized sample but either by acting as crack arrestors (crack propagation stops at these voids) or as stress concentrators for crack initiation. Stress concentration at these voids might aid in microcracking on quenching the partially crystallized sample from 680°C to room temperature. In both the cases, an increase in the toughness is expected if crack propagation is restricted in the first case while numerous microcracks formed would induce toughening in the second case.

4.5 Chapter summary

In accordance with one of the research objectives, an attempt at characterizing crack paths and understanding the fracture behaviour in partially crystallized 45S5 glass ceramic was made. Conclusions drawn in this study were:

- Vickers indentation technique revealed crack propagation in crystallized regions to exhibit no regular pattern – initiating all along the periphery of indents and deflecting at crystallites. The crack deflection could be due to crack propagation along preferred crystallographic orientation or thermal mismatch strain present between the crystallites and the amorphous matrix.

- Study of crack path as a function of crystallinity revealed that at lower crystallinity the crack paths were relatively straight as more amorphous phase was present. However, crack deflections became much higher and random with increasing crystallinity.

- The amorphous bioactive glass sample shattered and exploded during quenching while only cracks developed in the partially crystallized sample after quenching from 680°C.

- Fracture surfaces in a partially crystallized sample revealed cleavage fracture with the cracks deflecting at grain boundaries as they propagated from one crystallographic plane to another. This suggested higher fracture resistance in partially crystalline sample as more energy was consumed for crack propagation when compared with an amorphous sample with an almost flat fracture surface showing no hindrance in crack propagation.

Although crack deflections and high fracture resistance was observed in partially crystallized samples when compared with its amorphous counterpart, an optimum volume fraction and dispersion of crystalline phase which would cause crack path to turn around crystals thereby increasing fracture toughness still needs to be determined. Hence, a comprehensive quantitative study on the crack path and fracture surfaces on partially crystalline samples with various amounts of crystallinity may be carried out in future.

CHAPTER 5

Surface mineralization*

5.1 Introduction

It is paramount that increasing the mechanical properties in bioactive glass 45S5 should not deteriorate its bioactivity to any degree. Hence an attempt was made to study the *in vitro* mineralization of a partially crystalline sample in a phosphate buffer solution (PBS). Earlier studies by Nychka *et al.* [28, 29, 36] demonstrated the *in vitro* bioactivity and dissolution rate of amorphous and fully crystalline bioactive glasses. Herein, development of the mineralized layer formed on partially crystallized bioactive glass 45S5 after immersion in PBS as a function of time was studied. A partially crystalline sample (crystallized at 680°C for 30 minutes; ~ 68% crystalline) was chosen for the immersion test as it provided better resolution for analysis of the mineralized layer in **both** amorphous and crystalline regions.

5.2 Characterization of mineralized layer

5.2.1 SEM characterization

For any bioactive glass specimen taken out of an immersion solution, the mineralized layer formed on the surface will dry and experience a volume decrease. Due to constraint by the substrate the layer will develop a tensile stress and the layer may crack or peel in order to relieve the stress.

After immersion in PBS, when the amorphous and partially crystallized bioactive glass (680°C for 30 minutes) samples were removed and dried they experienced "mud cracking", and exhibited some layer peeling. Low magnification secondary electron micrographs for samples revealed different types of mud cracks formed within the mineralized layers on crystalline and amorphous regions on the samples (Figure 5.1).
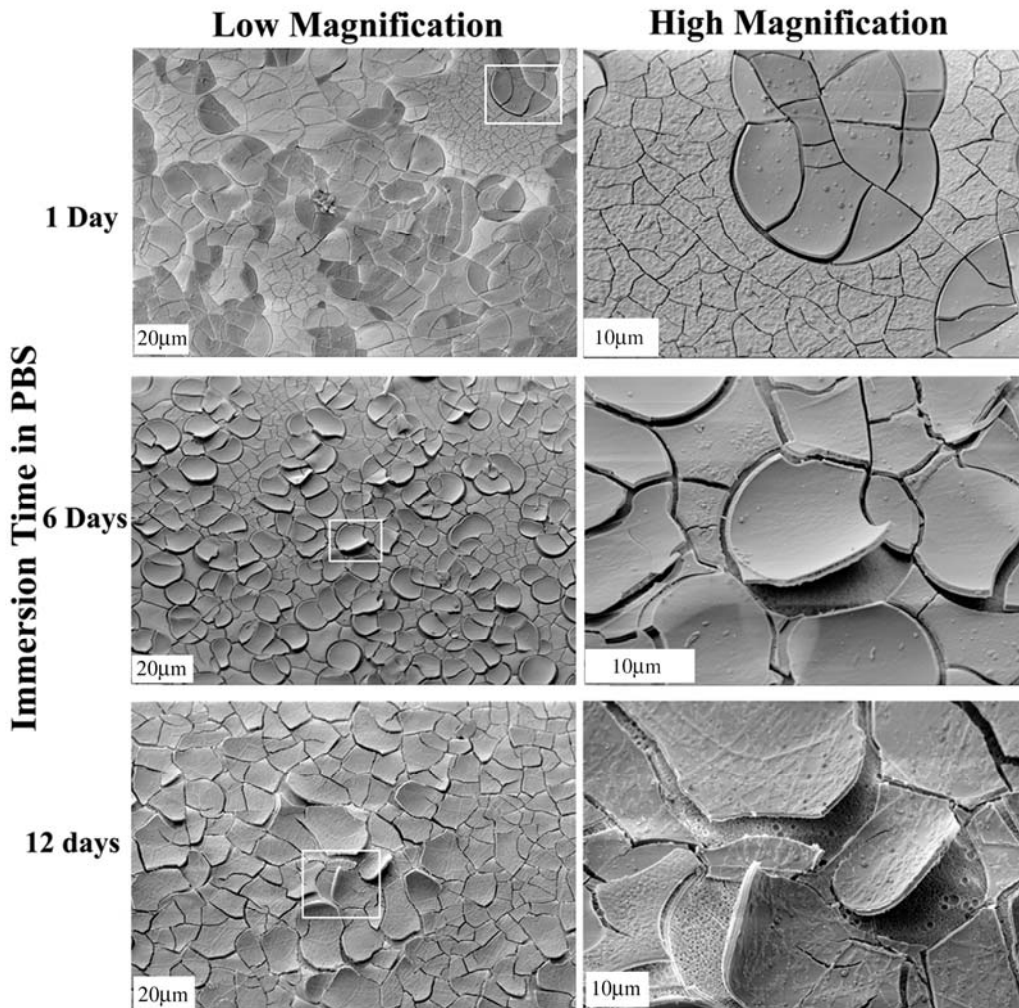
Fig 5.1: Secondary electron micrographs showing mineralization on partially crystallized bioactive glass 45S5 (crystallized at 680ºC for 30 min) after immersion in PBS for different time intervals.

Atop crystalline regions (identified by crystal shape), the cracks in the layer were large, infrequent, and non uniform and the layer appeared to have started to peel off from the substrate originating at the grain boundaries. On the

contrary, the layer atop amorphous bioactive glass zones formed many small uniform cracks and did not exhibit peeling.

Figure 5.1 also reveals the dissolution of the sample surface after prolonged immersion after 12 days in PBS. Notice that the underlying surface has been pitted due to dissolution in the high magnification micrograph of the 12 day immersed sample.

5.2.2 FTIR characterization

FTIR analysis of partially crystallized samples (680°C for 30 minutes) before and after immersion in PBS is shown in Figure 5.2. The reflectance spectra for the partially crystallized condition before immersion concur with that obtained by Peitl *et al.* [23]. The peaks between ~ 460 cm^{-1} and 610 cm^{-1}, denoted by black filled arrows indicate the vibrational modes of crystalline combeite phase ($Na_2Ca_2Si_3O_9$). The peak at 1089 cm^{-1} indicates Si-O-Si stretching vibration while the band around $\sim$925cm^{-1} (at absorption peak $\sim$962cm^{-1}) corresponds to Si-O-2NBO (non bridging oxygen) vibrational modes related with Ca^{2+} and Na^{2+} ions in the glass network. However, after immersion for 1 and 6 days, the NBO peak shifted and showed an absorption peak at 950cm^{-1} indicating the presence of Si-OH bonds. This suggests the formation of silanol (Si-OH) groups on the sample surface due to release of Ca^{2+} and Na^{2+} into solution and hydrolysis of the silica network in solution after immersion in PBS, which is given by the following reactions [35]:

$$Si\text{-}O\text{-}Na^+ + H^+ + OH^- \rightarrow Si\text{-}OH + Na^+_{(solution)} + OH^- \qquad (5.1)$$

$$Si\text{-}O\text{-}Si + H_2O \rightarrow Si\text{-}OH + OH\text{-}Si \qquad (5.2)$$

Another significant change in the FTIR spectra was observed after immersion: small peaks appeared in the region $\sim$ 1480cm^{-1} to 1635cm^{-1} (denoted by the white filled arrows). These small peaks might be due to the presence of carbonate CO_3^{2-} ions formed due to the reaction of atmospheric CO_2 with Ca^{2+} ions available on the sample surface [32, 74, 75]. However, the FTIR spectra were

difficult to interpret with respect to the mineralized phases due to the fact that the layer was very thin (recall Figure 5.1) and it tended to crack and/or peel from the surface upon drying. It is obvious that the bulk bioceramic sample substrate was sampled (combeite is detected) and it can be seen that the higher intensity spectra from the bulk sample have likely swamped the weaker signal from mineralized phases. Nonetheless, evidence of surface reactions is demonstrated. A quantitative microscopic technique to probe mineralized regions atop crystalline and amorphous phases may be utilized in future for better analysis.
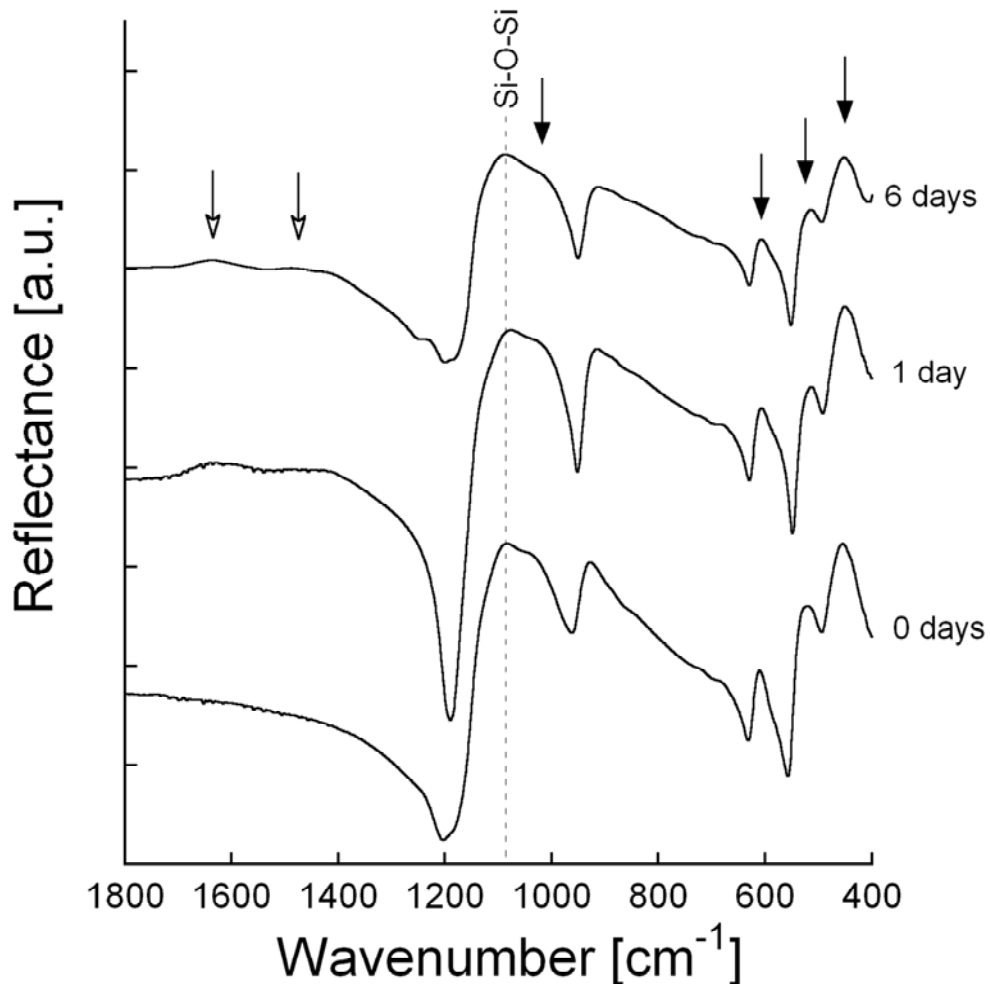
Fig. 5.2: FTIR spectra obtained for partially crystallized bioactive glass 45S5 (crystallized at 680°C for 30 min) after 0 days, 1 day and 6 days immersion in PBS.

5.3 Strain relaxation model

We propose that the possibility exists such that difference in chemical compositions and structure of amorphous and crystalline regions might:

- stimulate different reactions with immersion solutions (e.g., PBS), thereby producing a mineralized layer of dissimilar characteristics over the amorphous and crystalline regions, or that

- the same mineral layer interacts differently with the structure of the underlying material (e.g., epitaxy or lower interfacial fracture toughness on the crystallites).

Furthermore, in order to explain the varied crack sizes and peeling behaviour of the mineralized layer, a strain relaxation mechanism has been schematically illustrated in Figure 5.3. Without micro FTIR or micro Raman to determine chemical composition of the local minerals atop the glass ceramic we assume that the mineralized layer has similar physical and chemical attributes over both the amorphous and crystalline phases. The biaxial tensile stress (σ_m) in the mineralized layer developed as it contracted upon drying. In order to facilitate release of strain energy, the mineralized layer formed over crystalline regions formed large cracks and peeled itself off from the surface. As a result, it can be concluded that the bonding capability of the mineralized layer to the crystalline bioactive glass is frail, resulting in weaker adhesion and subsequently peeling off to release strain energy. However, in amorphous regions, the mineralized layer was well attached and exhibited a large number of small uniform cracks all along its surface in order to release the strain energy. This shows a higher adhesion capability of amorphous phase to the mineralized layer formed on the surface as compared to the crystalline phase of bioactive glass 45S5, at least for immersion times up to 6 days [76].
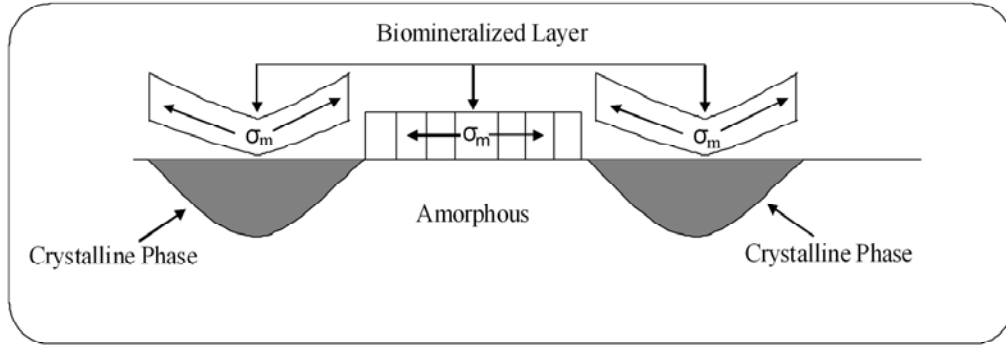
Fig. 5.3: Schematic figure showing strain release mechanism occurring in mineralized layer upon drying after the samples were taken out of PBS. The strain relaxation mechanism is different in the layer atop the crystalline and amorphous regions.

Earlier, Tolpygo *et al.* studied the stresses developed on alumina oxide films during thermal cycles [77]. A similar correlation was attempted to obtain mathematical expressions for tensile strain developed on the mineralized layer upon drying.

Figure 5.4 shows the schematic of strain generation (A) and relaxation (B) phenomenon in the mineralized layer and bioactive glass ceramic sample upon drying.

It is considered that a uniform mineralized layer of thickness h_m formed atop the bioactive glass sample (substrate) of thickness h_S. Initially, drying strains were generated in the mineralized layer and bioactive glass ceramic upon drying. However, after constraint a tensile stress (σ_m) was generated in the mineralized layer while a compressive stress (σ_s) was generated on the substrate (glass ceramic). Two cases can be considered here: Case 1 where mineralized layer atop amorphous regions was considered and Case 2, where mineralized layer atop crystalline regions was considered.

Case 1: The mineralized layer atop amorphous region formed numerous small cracks in it upon drying. So, the strain compatibility upon drying (after constraint) can be written as:

$$- \varepsilon_m - \varepsilon_c + \varepsilon^e{}_m = -\varepsilon_S - \varepsilon^e{}_s \tag{5.3}$$

where $\varepsilon^e{}_m$ and $\varepsilon^e{}_S$ are the biaxial elastic strains (after constraint); ε_m and ε_S are the drying strains in the mineralized layer and substrate (glass ceramic) respectively. ε_c is the cracking strain due to the formation of cracks in the mineralized layer, i.e., strain relaxation.

A

Under immersion

Mineralized layer

Bioactive glass ceramic

Upon drying

After constraint

σ_m

σ_s

B

Case 1: Amorphous
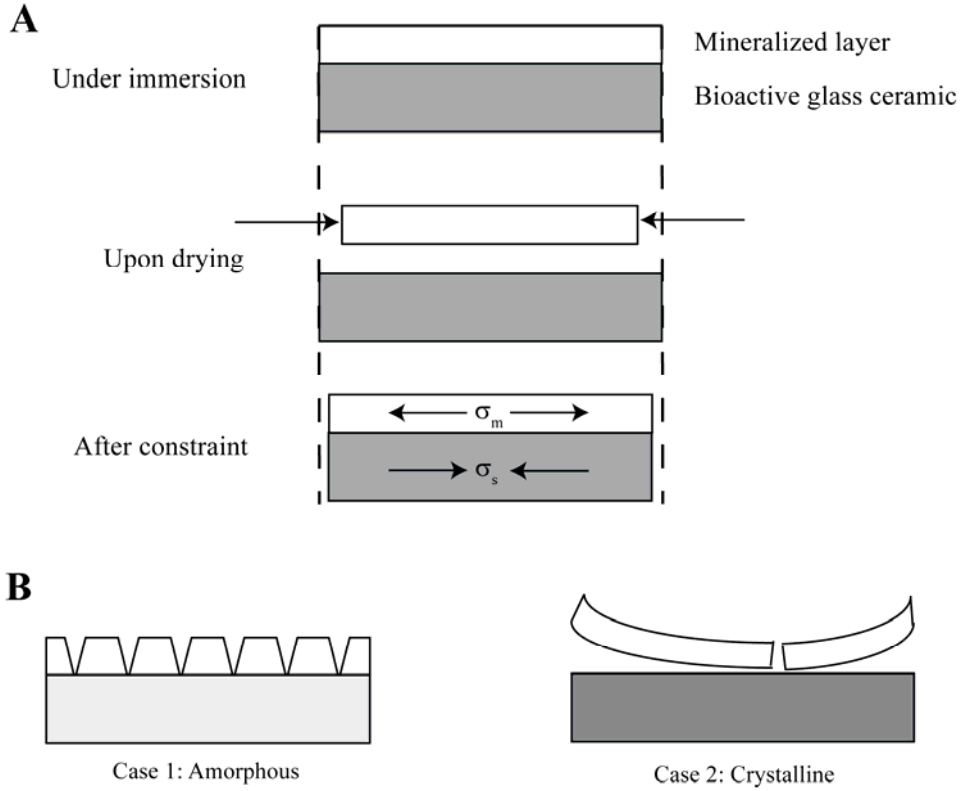
Case 2: Crystalline

Fig. 5.4: Schematic of (A) stress generation and (B) stress relaxation models in the mineralized layer atop amorphous and crystalline regions upon drying.

Upon drying, the mineralized layer contracts much more than the bulk bioactive glass sample which produces a constraint on the mineralized layer making it stretch, thus producing a tensile stress.

Force balance dictates:

$$\sigma_m h_m = \sigma_S h_S \qquad (5.4)$$

where σ_m and σ_S are biaxial stresses formed on the mineralized layer and bioactive glass sample respectively. Applying Hooke's law to Equation 5.4.

$$\frac{E_m h_m}{1 - v_m} . \varepsilon^e{}_m = \frac{E_S h_S}{1 - v_S} . \varepsilon^e{}_S \qquad (5.5)$$

$$\varepsilon^e{}_S = \frac{E_m h_m (1 - v_S)}{E_S h_S (1 - v_m)} . \varepsilon^e{}_m$$

$$\varepsilon^e{}_S = \varepsilon^e{}_m . B \qquad (5.6)$$

where $B = \dfrac{E_m h_m (1 - v_S)}{E_S h_S (1 - v_m)}$; v_m and v_S are the Poisson's ratio, and E_m and E_S are the Young's modulus for the mineralized layer and bioactive glass sample respectively.

Substituting in value of $\varepsilon^e{}_S$ in Equation 5.3,

$$\varepsilon^e{}_m = \frac{(\varepsilon_m - \varepsilon_S) + \varepsilon_c}{1 + B} \qquad (5.7)$$

Case 2: The mineralized layer atop the crystalline region formed larger bifurcating cracks which caused it to peel from the substrate upon drying. This was due to two types of strain – the strain that caused large bifurcating cracks (ε_{bc}) and the strain due to curvature that caused the mineralized layer to peel off from the substrate (ε_κ). So, the strain compatibility upon drying (after constraint) can be written as:

$$-\varepsilon_m - \varepsilon_\kappa - \varepsilon_{bc} + \varepsilon^e{}_m = -\varepsilon_S - \varepsilon^e{}_S \qquad (5.8)$$

Substituting Equation 5.6 in Equation 5.8,

$$\varepsilon^e{}_m = \frac{(\varepsilon_m - \varepsilon_S) + \varepsilon_{bc} + \varepsilon_\kappa}{1 + B} \qquad (5.9)$$

It was previously observed that the mineralized layer contracts much more on drying i.e., $\varepsilon_m \gg \varepsilon_S$ (since, $\varepsilon_S \rightarrow 0$; no strain develops in the bulk ceramic

substrate upon drying); hence the value of ε^e_m in Equations 5.7 and 5.9 is always positive indicating that the mineralized layer is in tension. Thus, material properties must be known for both the mineralized layer and glass ceramic in order to determine the tensile strains and stresses developed in the mineralized layer.

In Case 1, the strain energy is released only by formation of numerous small cracks in the mineralized layer while in Case 2, the strain energy is released by formation of large bifurcating cracks and peeling of the layer from the substrate. Assuming the biaxial stress (σ_m) generated is equivalent for mineralized layer atop both crystalline and amorphous regions, it can be concluded that lesser amount of energy was required to peel the mineralized layer atop crystalline regions. Therefore, fracture stress at the crystal-mineral interface is less than that at the amorphous-mineral interface. In other words, the energy release rate at the amorphous-mineral surface interface ($G_{amorphous-mineral}$) is higher than the energy release rate at the crystal-mineral interface ($G_{crystal-mineral}$)

$$\text{i.e., } G_{amorphous-mineral} > G_{crystal-mineral}$$

However, the cracking pattern observed in these *in vitro* tests might not be similar to what actually occurs *in vivo*. Nonetheless, this observation may prove useful for *in vivo* conditions, as any mineralized layer formed during bone-implant interfacial reactions would have to withstand some form of stress during service and having the ability to adhere with the implant material under such stress could be paramount. A future *in vivo* study confirming and comparing the stiffness of the crystalline and amorphous phases with that of the mineralized layer formed would provide a great impetus on understanding the adhesion behaviour of bioactive glass-ceramic to the mineralized layer, and across any implant-tissue interface.

For longer times of immersion (>6 days) the demarcation between amorphous and crystalline regions (underneath the mineral layer) is less distinguished, and peeling of the mineral layer following drying does not correlate

as well with underlying structure. That being said, there are regions with a large degree of peeling and such regions seem to correlate with fewer cracks per unit area; a bimodal distribution of crack density seems to be evident.

5.4 Chapter summary

In vitro immersion tests of partially crystallized bioactive glass 45S5 in PBS indicated formation of a Si-OH network and confirmed lower adhesion capability of crystalline phase to the mineralized layer formed on the surface in the presence of a biaxial tensile stress as compared to the amorphous region. Lower adhesion behaviour of mineralized layer atop crystalline regions might be attributed to different chemical and physical characteristics of mineralized layer formed on both crystalline and amorphous phases.

Chapter 6

Conclusions and future work

6.1 Conclusions

Owing to the poor mechanical properties of bioactive glass 45S5, it is essential to produce a bioactive glass 45S5 with enhanced mechanical properties without any compromise in its bioactivity. This reason provided the main motivation behind conducting this research: production of a 45S5 bioactive glass ceramic with an optimum volume fraction of crystals dispersed and size in the amorphous matrix possessing the ability to turn crack paths around crystals thereby improving the fracture toughness. However, knowledge of crystallization kinetics and mineralization behaviour of the crystalline phase is paramount for production and application feasibility respectively. Hence, this research was conducted to study the Avrami crystallization kinetics, crack propagation, fracture mode and mineralization in partially crystalline bioactive glass 45S5, so that the crystalline fraction could be controlled.

Thermal treatment of bulk bioactive glass 45S5 samples revealed the rate of crystallization; microstructure and degrees of crystallinity can be varied by varying the processing parameters such as crystallization temperature, time of crystallization and heating rate. Avrami kinetics of crystallization formulated for the temperature range of 640ºC to 720ºC revealed that although the crystallization rate and degree of crystallinity varied with the processing parameters, the mode of crystallization always followed three dimensional growth of crystals (bulk nucleation) with uniform nucleation i.e., Avrami exponent 'n'~ 3 irrespective of changes in crystallization temperature and heating rate. While a TTT curve constructed for the range 640ºC to 720ºC provided a good fit with the Avrami transformation-time plots, this temperature range was still below the nose of the TTT curve.

Crack propagation study by Vickers indentation technique showed a transition from straight crack path in amorphous to random crack path deflections (as high as 30°) in the crystalline regions indicating hindrance provided by crystals as the cracks propagate along preferred crystallographic planes. This increase in fracture resistance was further supported by higher fracture resistance shown by partially crystallized samples as compared to its amorphous counterpart on quenching. Higher hindrance to crack propagation shown by partially crystalline glass ceramic suggested that there might be an optimum volume fraction, size, and dispersion of crystals which would turn crack path around crystals altogether providing the highest fracture toughness (be it from a crystal forming from the glass, such as combeite, or a different crystal type forming from a new glass composition).

In order to determine the mineralization behaviour of the glass ceramic, i*n vitro* immersion tests in PBS was conducted which indicated higher adhesion capability of the mineralized layer with the amorphous phase when compared with the crystalline phase upon drying. This might be attributed to different chemical and physical characteristics of mineralized layer formed on both crystalline and amorphous phases. However, fragility of the mineralized layer hindered proper analyses of the mineralized layer.

6.2 Future work

This research could be extended in the following manner in order to fulfill long term goals of producing a bioactive glass 45S5 with enhanced mechanical properties without compromising bioactivity:

- Fracture toughness testing of samples, such as single-edge notched beam (SENB) containing different volume fraction of crystalline phases with varied grain sizes may be carried out to assess the optimum microstructure which would provide the highest toughness. R-curve behaviour would be favoured over straight modulus of rupture testing.

116

- Construction of a TTT curve (quenching from melt and holding at desired temperature) along the whole crystallization temperature range which would provide better crystallization kinetics and processing window. Modelling of the TTT curve lines would also improve understanding of the nucleation and growth phenomena.

- Construction of a continuous cooling transformation curve (CCT; cooling at various rates from melt) which would provide better processing information for engineering manufacture of glass ceramics.

- Transmission electron microscopy (TEM) to better understand the mode of crystallization, lattice parameters and crystalline phases formed.

- Bioactivity of the crystalline phase as compared to the amorphous phase in a fluid such as SBF which is more indicative of the human body fluid. More detailed analysis of the mineralized layer formed on the surface to have a better idea about the mineralization behaviour.

Bibliography:

[1] V. J. Shirtliff, L. L. Hench, Journal of Materials Science 38 (2003) 4697-4707.

[2] L. L. Hench, Journal of Materials Science-Materials in Medicine 17 (2006) 967-978.

[3] L. L. Hench, Journal of the American Ceramic Society 81 (1998) 1705-1728.

[4] L.L. Hench, E. C. Ethridge, Biomaterials: An Interfacial Approach, Academic Press, New York, 1982.

[5] S. M. Best, A. E. Porter, E. S. Thian, J. Huang, Journal of the European Ceramic Society 28 (2008) 1319-1327.

[6] L. L. Hench, Biomaterials 19 (1998) 1419-1423.

[7] D. Shi, Biomaterials and Tissue Engineering, Springer, 2004, p. 27-30.

[8] R. Li, A. E. Clark, L. L. Hench, Journal of Applied Biomaterials 2 (1991) 231-239.

[9] J. W. Nicholson, Chemistry of Medical and Dental Materials, RSC Publishing, 2002, p. 83.

[10] J. Wilson, S. B. Low, Journal of Applied Biomaterials 3 (1992) 123-129.

[11] L. L. Hench, and, J. K. West, Life Chem. Rep. 13 (1996) 187-241.

[12] H. Oonishi, L. L. Hench, J. Wilson, F. Sugihara, E. Tsuji, S. Kushitani, H. Iwaki, Journal of Biomedical Materials Research 44 (1999) 31-43.

[13] H. Oonishi, S. Kushitani, E. Yasukawa, H. Iwaki, L. L. Hench, J. Wilson, E. I. Tsuji, T. Sugihara, Clinical Orthopaedics and Related Research (1997) 316-325.

[14] L. L. Hench, R. J. Splinter, T. K. Greenlee, W. C. Allen, Journal of Biomedical Materials Research 2 (1971) 117-141.

[15] T. K. Greenlee, C. A. Beckham, J. C. Malmorg, A. R. Crebo, Journal of Biomedical Materials Research 6 (1972) 235-&.

[16] L. L. Hench, H. A. Paschall, Journal of Biomedical Materials Research 7 (1973) 25-42.

[17] M. Hamadouche, L. Sedel, Journal of Bone and Joint Surgery-British Volume 82B (2000) 1095-1099.

[18] L. L. Hench, Glass Technology 44 (February 2003) 1-10.

[19] G. Jell, M. M. Stevens, Journal of Materials Science-Materials in Medicine 17 (2006) 997-1002.

[20] W. P. Cao, L. L. Hench, Ceramics International 22 (1996) 493-507.

[21] L. L. Hench, American Ceramic Society Bulletin 84 (2005) 18-21.

[22] L. L. Hench, Mrs Bulletin 24 (1999) 13-19.

[23] O. Peitl, G. P. LaTorre, L. L. Hench, Journal of Biomedical Materials Research 30 (1996) 509-514.

[24] L. L. Hench, D. L. Wheeler, D. C. Greenspan, Journal of Sol-Gel Science and Technology 13 (1998) 245-250.

[25] L. L. Hench, Journal of Biomedical Materials Research 41 (1998) 511-518.

[26] Q. Z. Z. Chen, I. D. Thompson, A. R. Boccaccini, Biomaterials 27 (2006) 2414-2425.

[27] L. Lefebvre, J. Chevalier, L. Gremillard, R. Zenati, G. Thollet, D. Bernache-Assolant, A. Govin, Acta Materialia 55 (2007) 3305-3313.

[28] J. A. Nychka, D. Li, B. Alexander, Journal of the Mechanical Behavior of Biomedical Materials 1 (2008) 243-251.

[29] J. A. Nychka, S. L. R. Mazur, S. Kashyap, D. Li, F. Q. Yang, Jom 61 (2009) 45-51.

[30] X. F. Chen, Y. C. Meng, Y. L. Li, N. R. Zhao, Applied Surface Science 255 (2008) 562-564.

[31] O. Bretcanu, X. Chatzistavrou, K. Paraskevopoulos, R. Conradt, I. Thompson, A. R. Boccaccini, Journal of the European Ceramic Society 29 (2009) 3299-3306.

[32] M. Cerruti, D. Greenspan, K. Powers, Biomaterials 26 (2005) 1665-1674.

[33] M. G. Cerruti, D. Greenspan, K. Powers, Biomaterials 26 (2005) 4903-4911.

[34] D. C. Clupper, L. L. Hench, Journal of Non-Crystalline Solids 318 (2003) 43-48.

[35] M. R. T. Filgueiras, G. Latorre, L. L. Hench, Journal of Biomedical Materials Research 27 (1993) 1485-1493.

[36] D. Li, F. Q. Yang, J. Nychka, Engineering Fracture Mechanics 75 (2008) 4898-4908.

[37] T. Kokubo, H. Takadama, Biomaterials 27 (2006) 2907-2915.

[38] G. E. Vargas, R. V. Mesones, O. Bretcanu, J. M. P. Lopez, A. R. Boccaccini, A. Gorustovich, Acta Biomaterialia 5 (2009) 374-380.

[39] B. Ilharreborde, E. Morel, F. Fitoussi, A. Presedo, P. Souchet, G. F. Penneçot, K. Mazda, J Pediatr Orthop. 28 (2008) 347-351.

[40] M. Vogel, C. Voigt, U. M. Gross, C. M. Muller-Mai, Biomaterials 22 (2001) 357-362.

[41] M. D. Michel, A. Mikowski, C. M. Lepienski, C. E. Foerster, F. C. Serbena, Journal of Non-Crystalline Solids 348 (2004) 131-138.

[42] W. D. Callister, Materials Science and Engineering: An introduction, John Wiley and Sons Inc., 2007.

[43] P. Sepulveda, J. R. Jones, L. L. Hench, Effect of particle size on Bioglass (R) dissolution, in: S. Giannini, A. Moroni (Eds.), Bioceramics, vol 192-1, Trans Tech Publications Ltd, Zurich-Uetikon, 2000, pp. 629-633.

[44] B. D. Leatherman, J. L. Dornhoffer, Otology & Neurotology 23 (2002) 657-660.

[45] M. Vollenweider, T. J. Brunner, S. Knecht, R. N. Grass, M. Zehnder, T. Imfeld, W. J. Stark, Acta Biomaterialia 3 (2007) 936-943.

[46] D. L. Wheeler, K. E. Stokes, R. G. Hoellrich, D. L. Chamberland, S. W. McLoughlin, Journal of Biomedical Materials Research 41 (1998) 527-533.

[47] A. R. Boccaccini, I. Notingher, V. Maquet, R. Jerome, Journal of Materials Science-Materials in Medicine 14 (2003) 443-450.

[48] C. C. Lin, L. C. Huang, P. Y. Shen, Journal of Non-Crystalline Solids 351 (2005) 3195-3203.

[49] Housefie.L.G., L. L. Hench, American Ceramic Society Bulletin 53 (1974) 384-384.

[50] P. Buscemi, R. Chhatre, D. E. Clark, G. Y. Onoda, L. L. Hench, American Ceramic Society Bulletin 53 (1974) 611-611.

[51] G. A. Fuchs, Biomedizinische Technik 27 (1982) 24-29.

[52] D. C. Greenspan, L. L. Hench, Journal of Biomedical Materials Research 10 (1976) 503-509.

[53] A. S. Vlasov, O. V. Ludanova, Glass and Ceramics 52 (1995) 99-101.

[54] R. H. Doremus, Glass Science, 1994, p. 74.

[55] S. D. Stookey, R. D. Maurer, Pergamon Press, New York, 1962, p. 77.

[56] H. A. ElBatal, M. A. Azooz, E. M. A. Khalil, A. S. Monem, Y. M. Hamdy, Materials Chemistry and Physics 80 (2003) 599-609.

[57] A. El-Ghannam, E. Hamazawy, A. Yehia, Journal of Biomedical Materials Research 55 (2001) 387-395.

[58] O. Peitl, E. D. Zanotto, L. L. Hench, Journal of Non-Crystalline Solids 292 (2001) 115-126.

[59] A. S. Rizkalla, D. W. Jones, D. B. Clarke, G. C. Hall, Journal of Biomedical Materials Research 32 (1996) 119-124.

[60] B. Lawn, Fracture of Brittle Solids, Cambridge University Press, 1993, p. 204.

[61] R. W. Davidge, T. J. Green, Journal of Materials Science 3 (1968) 629-634.

[62] D. C. Clupper, J. J. Mecholsky, G. P. LaTorre, D. C. Greenspan, Journal of Biomedical Materials Research 57 (2001) 532-540.

[63] A. R. Boccaccini, Q. Chen, L. Lefebvre, L. Gremillard, J. Chevalier, Faraday Discussions 136 (2007) 27-44.

[64] M. Avrami, Journal of Chemical Physics 7 (1939) 1103-1112.

[65] M. Avrami, Journal of Chemical Physics 9 (1941) 177-184.

[66] M. Avrami, Ibid 8 (1940) 212-224.

[67] N. Widlak, R. W. Hartel, S. Narine, Crystallization and solidification properties of lipids, AOCS Press, 2001, p. 112.

[68] A. K. Jena, M. C. Chaturvedi, Phase transformation in Materials Prentice Hall, 1992, p. 247.

[69] Y. Liu, Q. Xiang, Y. Tan, X. Sheng, Journal of Non-Crystalline Solids 354 (2008) 938-944.

[70] N. Koga, J. Sestak, Z. Strnad, Thermochimica Acta 203 (1992) 361-372.

[71] G. S. Meiling, D. R. Uhlmann, Physics and Chemistry of Glasses 8 (1967) 62.

[72] A. Elyamani, E. Snitzer, R. Pafchek, G. H. S. Jr., Journal of Materials Research 6 (1991) 401-406.

[73] R. L. Fullman, Transactions of the American Institute of Mining and Metallurgical Engineers 197 (1953) 447-452.

[74] L. Peddi, R. K. Brow, R. F. Brown, Journal of Materials Science-Materials in Medicine 19 (2008) 3145-3152.

[75] M. Cerruti, C. Morterra, Langmuir 20 (2004) 6382-6388.

[76] T. M. Adams, R. A. Layton, Introductory MEMS Fabrication and Applications, Springer, US, 2009, p. 131-153.

[77] V. K. Tolpygo, D. R. Clarke, Acta Materialia 47 (1999) 3589-3605.